



TEZ ŞABLONU ONAY FORMU
THESIS TEMPLATE CONFIRMATION FORM.

- Şablonda verilen yerleşim ve boşluklar değiştirilmemelidir.
- Jüri tarihi** Başlık Sayfası, İmza Sayfası, Abstract ve Öz'de ilgili yerlere yazılmalıdır.
- İmza sayfasında jüri üyelerinin unvanları doğru olarak yazılmalıdır. Tüm imzalar **mavi pilot kaleme** atılmalıdır.
- Disiplinlerarası** programlarda görevlendirilen öğretim üyeleri için jüri üyeleri kısmında tam zamanlı olarak çalışmaları anabilim dalı başkanlığının ismi yazılmalıdır. Örneğin: bir öğretim üyesi Biyoteknoloji programında görev yapıyor ve biyoloji bölümünde tam zamanlı çalışıysa, İmza sayfasına biyoloji bölüm yazılmalıdır. İstisnai olarak, disiplinler arası program başkanı ve tez danışmanı için disiplinlerarası program adı yazılmalıdır.
- Tezin **son sayfasının sayfa** numarası Abstract ve Öz'de ilgili yerlere yazılmalıdır.
- Bütün chapterlar, referanslar, ekler ve CV sağ sayfada başlamalıdır. Bunun için **kesmeler** kullanılmıştır. **Kesmelerin kayması** fazladan boş sayfaların oluşmasına sebep olabilir. Bu gibi durumlarda paragraf (¶) işaretine tıklayarak kesmeleri görür hale getirin ve yerlerini **kontrol edin**.
- Figürler ve tablolar kenar boşluklarına taşmamalıdır.
- Şablonda yorum olarak eklenen uyarılar dikkatle okunmalı ve uygulanmalıdır.
- Tez yazdırılmadan önce PDF olarak kaydedilmelidir. Şablonda yorum olarak eklenen uyarılar PDF dokümanında yer almamalıdır.
- Tez taslaqlarının kontrol işlemleri tamamlandıında, bu durum öğrencilere METU uzantılı öğrenci e-posta adresleri aracılığıyla duyurulacaktır.
- Tez yazım süreci ile ilgili herhangi bir sıkıntı yaşarsanız, **Sıkça Sorulan Sorular (SSS)** sayfamızı ziyaret ederek yaşadığınız sıkıntıyla ilgili bir çözüm bulabilirsiniz.

- Do not change the spacing and placement in the template.
- Write **defense date** to the related places given on Title page, Approval page, Abstract and Öz.
- Write the titles of the examining committee members correctly on Approval Page. **Blue ink** must be used for all signatures.
- For faculty members working in **interdisciplinary programs**, the name of the department that they work full-time should be written on the Approval page. For example, if a faculty member staffs in the biotechnology program and works full-time in the biology department, the department of biology should be written on the approval page. Exceptionally, for the interdisciplinary program chair and your thesis supervisor, the interdisciplinary program name should be written.
- Write **the page number of the last page** in the related places given on Abstract and Öz pages.
- All chapters, references, appendices and CV must be started on the right page. **Section Breaks** were used for this. **Change in the placement** of section breaks can result in extra blank pages. In such cases, make the section breaks visible by clicking paragraph (¶) mark and **check their position**.
- All figures and tables must be given inside the page. Nothing must appear in the margins.
- All the warnings given on the comments section through the thesis template must be read and applied.
- Save your thesis as pdf and Disable all the comments before taking the printout.
- This will be announced to the students via their METU students e-mail addresses when the control of the thesis drafts has been completed.
- If you have any problems with the thesis writing process, you may visit our **Frequently Asked Questions (FAQ)** page and find a solution to your problem.

Yukarıda bulunan tüm maddeleri okudum, anladım ve kabul ediyorum. / I have read, understand and accept all of the items above.

Name : Behrang
Surname : Hosseiniaghdam
E-Mail : b.hosseini@gmail.com
Date : 31.03.2023
Signature : _____

FAULT DETECTION OF A PLANETARY GEAR SYSTEM BASED ON NON-
LINEAR DYNAMIC MODELING AND VIBRATION SIGNALS VIA NON-
STATIONARY TIME SERIES MODELS

A THESIS SUBMITTED TO
THE GRADUATE SCHOOL OF NATURAL AND APPLIED SCIENCES
OF
MIDDLE EAST TECHNICAL UNIVERSITY

BY

BEHRANG HOSSEINIAGHDAM

IN PARTIAL FULFILLMENT OF THE REQUIREMENTS
FOR
THE DEGREE OF DOCTOR OF PHILOSOPHY
IN
MECHANICAL ENGINEERING

MARCH 2023

Approval of the thesis:

Fault Detection of a Planetary Gear System Based on Non-linear Dynamic Modeling and Vibration Signals via Non-stationary Time Series Models

submitted by **BEHRANG HOSSEINIAGHDAM** in partial fulfillment of the requirements for the degree of **Doctor of Philosophy in Mechanical Engineering, Middle East Technical University** by,

Prof. Dr. Halil Kalıpçilar
Dean, Graduate School of Natural and Applied Sciences

Prof. Dr. M. A. Sahir Arıkan
Head of the Department, **Mechanical Engineering**

Prof. Dr. Ender Ciğeroğlu
Supervisor, **Mechanical Engineering, METU**

Examining Committee Members:

Prof. Dr. Yiğit Yazıcıoğlu
Mechanical Eng, METU

Prof. Dr. Ender Ciğeroğlu
Mechanical Eng, METU

Assoc. Prof. Dr. Mehmet Bülent Özer
Mechanical Eng, METU

Assoc. Prof. Dr. Can Ulaş Doğruer
Mechanical Engineering, Hacettepe University

Assoc. Prof. Dr. Kutluk Bilge Arıkan
Mechanical Engineering, TED University

Date: 31.03.2023



I hereby declare that all information in this document has been obtained and presented in accordance with academic rules and ethical conduct. I also declare that, as required by these rules and conduct, I have fully cited and referenced all material and results that are not original to this work.

Name Last name :

Behrang Hosseiniaghdam

Signature :

ABSTRACT

FAULT DETECTION OF A PLANETARY GEAR SYSTEM BASED ON NON-LINEAR DYNAMIC MODELING AND VIBRATION SIGNALS VIA NON-STATIONARY TIME SERIES MODELS

Hosseiniaghdam, Behrang
Doctor of Philosophy, Mechanical Engineering
Supervisor: Prof. Dr. Ender CİĞEROĞLU

March 2023, 157 pages

The current study aims to investigate the fault diagnosis problem in a gear system using non-stationary time series models and non-linear dynamic modeling. Fault diagnosis of gearboxes is an ongoing and significant research topic in the context of condition monitoring. Various gears and gearboxes are used in machinery found in different industries and vehicles. During manufacturing, detecting gearbox faults is also an important task. Faults such as tooth profile error, helix angle error (of helical gears), and assembly errors are of the faults as mentioned earlier. Some other faults occur when the machinery is operating and if they are not prognosed in advance they can finally result in catastrophic failures. Instances of such faults include gear tooth crack, surface pitting, and spalling. For fault detection, first, a non-linear dynamic model, including tooth root crack, is developed. Then the dynamic model with fault is verified by using the results given in the available literature. In the next step, fault detection using experimental data is carried out. The process starts with the analysis of the vibration signals measured from a test setup to identify the fault features in the frequency spectrum via Fast Fourier Transform (FFT). Before FFT analysis, the signals are averaged via Time Synchronous Averaging (TSA) method. Subsequently,

the TSA signals are modeled via a non-stationary time series model called Functional Time Series Time Dependent Autoregressive Moving Average (FS-TARMA) and its another form called FS-TAR. The developed method of fault detection, utilizes the identified models for vibration analysis and the estimation of Power Spectral Densities to evaluate fault effects in the time-frequency domain. Subsequently, a fault detection and localization algorithm is developed by comparing models associated with healthy and faulty gearboxes. Finally, the experimental results, as well as theoretical results, are analyzed by the use of the developed method to demonstrate its applicability and effectiveness.

Keywords: Gear Dynamics, Non-linear vibrations, Vibration signal analysis, Fault detection, Time series models.

ÖZ

DOĞRUSAL OLMAYAN DİNAMİK MODELLEME VE TİTREŞİM SİNYALLERİNE DAYALI BİR PLANET DİŞLİ SİSTEMİNİN DURGUN OLMAYAN ZAMAN SERİSİ MODELLERİ İLE HATA TESPİTİ

Hosseiniaghdam, Behrang
Doktora, Makina Mühendisliği
Tez Yöneticisi: Prof. Dr. Ender Ciğeroğlu

Mart 2023, 157 sayfa

Bu çalışma, durağan olmayan zaman serisi modelleri ve doğrusal olmayan dinamik modelleme kullanarak bir dişli sisteminde arıza teşhis problemini araştırmayı amaçlamaktadır. Dişli kutularının arıza teşhisini, durum izleme bağlamında devam eden ve önemli bir araştırma konusudur. Farklı endüstrilerde ve araçlarda bulunan makinelerde çeşitli dişliler ve dişli kutuları kullanılmaktadır. İmalat sırasında şanzıman arızalarının tespiti de önemli bir konudur. Diş profil hatası, helis açısı hatası (helisel dişlilerin) ve montaj hataları gibi hatalar daha önce bahsedildiği gibi hatalardandır. Diğer bazı arızalar, makine çalışırken meydana gelir ve önceden tespit edilmezlerse, sonunda feci arızalara neden olabilirler. Bu tür hataların örnekleri arasında dişli dişi çatlaması, yüzeyde çukurlaşma ve parçalanma yer alır. Arıza tespiti için öncelikle diş kök çatlığı dahil doğrusal olmayan bir dinamik model geliştirilmiştir. Daha sonra mevcut literatürde verilen sonuçlar kullanılarak hatalı dinamik model doğrulanmıştır. Bir sonraki adımda, deneyel veriler kullanılarak arıza tespiti gerçekleştirilir. Süreç, Hızlı Fourier Dönüşümü (FFT) aracılığıyla frekans spektrumundaki arıza özelliklerini belirlemek için bir test düzeneğinden ölçülen titreşim sinyallerinin analizi ile başlar. FFT analizinden önce, Zaman

Senkron Ortalama (TSA) yöntemi ile sinyallerin ortalaması alınır. FFT analizinden önce, Zaman Senkron Ortalama (TSA) yöntemi ile sinyallerin ortalaması alınır. Daha sonra, TSA sinyalleri, Fonksiyonel Zaman Serisi Zamana Bağlı Otoregresif Hareketli Ortalama (FS-TARMA) adı verilen durağan olmayan bir zaman serisi modeli aracılığıyla modellenir. Ardından, sağlıklı ve arızalı dişli kutuları ile ilgili modeller karşılaştırılarak bir arıza tespit ve lokalizasyon algoritması geliştirilmiştir. Son olarak, deneysel sonuçların yanı sıra teorik sonuçlar, uygulanabilirliğini ve etkinliğini göstermek için geliştirilen yöntemin kullanımıyla analiz edilir.

Anahtar Kelimeler: Dişli Dinamiği, Doğrusal olmayan titreşimler, Titreşim sinyali analizi, Arıza tespiti, Zaman serisi modelleri

Dedication

To my loving family, who have supported me throughout my life. Your endless love, encouragement, and sacrifices have been the motivating force behind my success. My parents, and my siblings, you have been my source of inspiration. I dedicate this thesis to you with all my love and appreciation.

ACKNOWLEDGMENTS

I would like to express my profound gratitude to my supervisor, Prof. Dr. Ender Ciğeroğlu, for his guidance, support, and encouragement throughout my Ph.D. research. He has been an excellent mentor, providing valuable feedback and guidance on my research work.

I would also like to thank the members of my thesis committee, Prof. Dr. Yiğit Yazıcıoğlu, Assoc. Prof. Dr. Mehmet Bülent Özer, Assoc. Prof. Dr. Can Ulaş Doğruer and Assoc. Prof. Dr. Kutluk Bilge Arıkan, for their valuable feedback and support throughout my PhD research. Their insightful comments and suggestions helped me to improve the quality of my research and writing.

I would also like to thank Dr. Imthiyas Manarikkal for providing experimental data measured from a planetary gearbox test rig in Coventry University.

TABLE OF CONTENTS

ABSTRACT	v
ÖZ	vii
ACKNOWLEDGMENTS	x
TABLE OF CONTENTS.....	xi
LIST OF TABLES	xiv
LIST OF FIGURES	xv
1 INTRODUCTION	1
2 LITERATURE REVIEW	3
2.1 Summary of literature	3
2.2 Methodology	10
2.3 Contributions to the field	12
2.4 Objectives and scope.....	13
3 Dynamic modeling of a planetary gearbox	15
3.1 Linear dynamic model	15
3.1.1 Linear dynamic response of the gear system.....	21
3.2 Non-linear dynamic model.....	26
3.2.1 Non-linear dynamic modeling of a spur gear pair with gear faults.....	26
3.2.2 Non-linear dynamic response of a purely rotational planetary gear system with sun gear fault.....	53
3.2.3 Non-linear dynamic modeling of a planetary gear system including translational DOFs of the gears with a planet gear fault.....	78
4 Analysis of experimental data.....	99

4.1	Experimental test rig and acquired data	99
4.1.1	Healthy case.....	99
4.1.2	Mild pitted case.....	99
4.1.3	Severe pitted case.....	100
4.1.4	Chipped tooth case.....	100
4.1.5	Missing tooth case	100
4.2	Analysis of gear vibration signals	102
4.2.1	Spectral analysis of planetary gear data by FFT.....	102
5	Fault detection process based on FS-TAR, FS-TARMA and AR metric.....	105
5.1	Modeling non-stationary signals and novelty detection	105
5.1.1	Estimation of non-stationary time series via FS-TARMA models.....	105
5.1.2	Estimation of nonstationary time series via FS-TAR models.....	109
5.1.3	AR metric for the comparison of time series models and novelty detection	
		112
6	Time-frequency analysis of gear vibration signals by FS-TAR and Wavelet Transform	115
6.1	Time-frequency analysis of gear vibration signals by Wavelet Transform	115
6.2	Time-frequency analysis of gear vibration signals by FS-TAR model.....	116
6.3	Continuous Wavelet Transform of vibration signals.....	117
6.4	FS-TAR model-based PSD.....	118
7	Fault detection based on FS-TAR models via vibration signals: results.....	125
7.1	Modeling and estimation of gear signals via FS-TAR models.....	125
7.1.1	FS-TAR model identification, results	125
7.2	Gear fault detection based on estimated FS-TAR models.....	128

7.3	Conclusion	133
8	Conclusion and future works	135
8.1	Conclusion	135
8.2	Future works	137
	REFERENCES	139
A.	Equations of motion of the non-linear planetary gear system	147
	CURRICULUM VITAE	157

LIST OF TABLES

TABLES

Table 3.1 Parameter values used in the simulations [50]	22
Table 3.2 frequencies with multiplicity m and number of planets N	23
Table 3.3 Gear system data [1].....	44
Table 3.4 Possible configurations at line of action based on fixed element, input element, and the direction of rotation for input.....	58
Table 3.5 Gear parameters for planetary gearbox	63
Table 3.6 The calculated values of mesh phasing.	64
Table 4.1 Properties of the planetary gearbox used for data acquisition.....	100
Table 4.2 Frequencies of different components of the planetary gearbox	103

LIST OF FIGURES

FIGURES

Figure 2.1 Fault detection process based on comparison of time series	12
Figure 3.1 Schematic view of the planetary gearbox with three planets [49].....	18
Figure 3.2 a) planar motion of the sun gear, b) the planet gear and carrier; the dashed and solid lines: positions before and after motion [49].....	19
Figure 3.3 meshing between the sun and a planet [49].....	19
Figure 3.4 meshing between the ring and a planet [49].....	20
Figure 3.5 Gear mesh stiffness between a) planet i and ring and sun, b) ring gear and planet i [49]	20
Figure 3.6 First mode of the planetary gearbox	23
Figure 3.7 Second mode of the planetary gearbox	24
Figure 3.8 The third mode of the planetary gearbox.....	24
Figure 3.9 The fourth mode of the planetary gearbox	25
Figure 3.10 The fifth mode of the planetary gearbox	25
Figure 3.11 The mode thirteen of the planetary gearbox.....	26
Figure 3.12 Dynamic model of a spur gear pair [1].....	28
Figure 3.13 Dynamic model of a spur gear pair [1].....	33
Figure 3.14 Meshing steps and the number of teeth in contact [54].....	34
Figure 3.15 Mesh stiffness for positive modification coefficient	35
Figure 3.16 Mesh stiffness without modification	36
Figure 3.17 Mesh stiffness with negative modification coefficient.....	36
Figure 3.18 Periodic decaying sinusoidal pulse [55]	38
Figure 3.19 Modeling crack in a beam with rectangular cross section.....	39
Figure 3.20 Gear tooth profile dimensions	40
Figure 3.21 Modeling tooth root crack	41
Figure 3.22 Mesh stiffness of gear with cracked tooth calculated by FEM [57]....	42
Figure 3.23 Mesh stiffness of cracked tooth calculated using the approximate method.....	42

Figure 3.24 Tangential acceleration at pitch point, gear	44
Figure 3.25 Tangential acceleration at pitch point, pinion	45
Figure 3.26 Gear bearing acceleration.....	45
Figure 3.27 Pinion bearing acceleration	46
Figure 3.28 Gear bearing acceleration.....	46
Figure 3.29 Pinion bearing acceleration [1]	47
Figure 3.30 Calculated pinion bearing acceleration, intact gears.....	48
Figure 3.31 Pinion bearing acceleration, pitted tooth [1].....	48
Figure 3.32 Calculated pinion bearing acceleration, pitted tooth.....	49
Figure 3.33 Dynamic tooth load, including pinion pitting	50
Figure 3.34 Pinion bearing acceleration, including pinion pitting	50
Figure 3.35 Gear bearing acceleration, including pinion pitting	51
Figure 3.36 Pinion pitch point acceleration, including pinion pitting	51
Figure 3.37 Gear pitch point acceleration, including pinion pitting.....	52
Figure 3.38 FFT of the pinion bearing acceleration with pitted pinion tooth	52
Figure 3.39 Schematic of a planetary gearbox. $u_s, u_c, u_r, u_{1,2,3}$ represent degrees of freedom of the model [59]	58
Figure 3.40 Mesh phases of a planetary gearbox shown on the periodic mesh stiffness $\gamma_{sn}, \gamma_m, \gamma_{rs}, \gamma_{s1} = 0$, and $t = 0$ corresponds to pitch point contact at first plant and sun mesh. The symbol * refers to starting point of contact a pitch point [59] .	59
Figure 3.41 (a) Schematic of contact points progression on periodic mesh stiffness [59]	60
Figure 3.42 Rotation of sun and carrier between two successive fault mesh of sun gear [60].....	65
Figure 3.43 Mesh stiffness of different planet-sun meshes for faulty sun gear	67
Figure 3.44 Mesh stiffness of different sun gear with different planets with mesh phasing included	67
Figure 3.45 Sun gear acceleration, healthy gearbox.....	71
Figure 3.46 Carrier acceleration, healthy gearbox	72

Figure 3.47 Planetary gear acceleration, healthy gearbox	72
Figure 3.48 Acceleration of faulty planet gear, cracked planet	73
Figure 3.49 Acceleration of sun gear, cracked planet.....	74
Figure 3.50 Acceleration of the carrier, cracked planet.....	74
Figure 3.51 FFT of sun gear acceleration, healthy gearbox.....	75
Figure 3.52 FFT of carrier acceleration, healthy gearbox.....	75
Figure 3.53 FFT of a planetary gear acceleration, healthy gearbox	76
Figure 3.54 FFT of sun gear acceleration, cracked sun	76
3.55 FFT of sun gear acceleration, healthy vs cracked planet (a) general view, (b) smaller frequency interval.....	77
According to the Figure 3.56, the position vector of the sun and carrier can be expressed as follows	79
Figure 3.57 Lumped parameter model of a planetary gear system [49]	80
Figure 3.58 Initial and displaced locations of (a) sun gear; (b) carrier and planet [49]	80
Figure 3.59 Gear mesh between sun and planet i [49]	81
Figure 3.60 Angular acceleration of sun gear, purely rotational model	87
Figure 3.61. Angular acceleration of sun gear, non-linear model.....	87
Figure 3.62 Comparison of FFT of sun gear angular acceleration for non-linear case with $k_p = k_c = k_s = 10^{18} \text{ N} / \text{m}$ and purely rotational model.....	88
Figure 3.63 Angular acceleration of a planet, healthy nonlinear system.....	89
Figure 3.64 Translational acceleration of a planet in radial direction η , healthy nonlinear system	90
Figure 3.65 Angular acceleration of the carrier, healthy nonlinear system	91
Figure 3.66 Translational acceleration of the carrier in x direction, healthy nonlinear system	92
Figure 3.67 Angular acceleration of the sun gear, healthy nonlinear system	93
Figure 3.68 Translational acceleration of the sun gear in x direction, healthy nonlinear system	94

Figure 3.69 Angular acceleration of the sun gear, faulty nonlinear system	95
Figure 3.70 Translational acceleration of a planet in radial direction η , healthy nonlinear system	96
Figure 3.71 Translational acceleration of the sun gear in x direction, healthy nonlinear system	97
Figure 3.72 Comparison of the FFT of sun gear angular acceleration, healthy vs faulty.....	98
Figure 4.1 Different fault cases considered in the experimental data collection [64]	101
Figure 4.2 Vibrations measured on top of ring gear, low-pitted planet	103
Figure 4.3 FFT of vibration signals measured on top of ring gear, healthy case ..	104
Figure 4.4 FFT of vibration signals measured on top of ring gear, pitted case.....	104
Figure 6.1 CWT graph of the healthy gearbox vibration, a) 3D view, b) 2D view	119
Figure 6.2 CWT graph of the pitted gearbox vibration, a) 3D view, b) 2D view ..	120
Figure 6.3 PSD estimate of the healthy gear vibration signal based on FS-TAR model	122
Figure 6.4 PSD estimate of the pitted gear vibration signal based on FS-TAR model (dotted lines are used for clarification only).....	123
Figure 7.1 BIC values for different AR and functional basis orders plotted as a 3D surface.....	126
Figure 7.2 (a) Prediction vs time series for a segment of nonstationary gear acceleration, (b) residual series of estimated model, (c) residual variance	127
Figure 7.3 AR(∞) of FS-TAR models associated with healthy and pitted cases: a) for one revolution of carrier, b) for two revolutions of carrier; t_{pr} : planet frequency with respect to ring, t_{car} : period of carrier rotation.....	132
Figure 7.4 Meshing succession of planetary gear faulted tooth (marked with a red dot) with: a) ring gear (first time), b) sun gear and c) ring gear (second time).....	132

CHAPTER 1

INTRODUCTION

Gearboxes are used in most of machinery operating in various industries. Automotive, helicopters, petrochemical factories, wind turbine etc. are among the typical ones. Planetary gearboxes provide a number of advantages over the other gearboxes and therefore they are preferred to the conventional gear systems. In some areas the condition monitoring of the gearbox and fault prognosis is of high importance. Detection of an incipient gear fault in the earlier stages can reduce the maintenance costs, increase reliability and prevent catastrophic failures. This is more critical in vehicles such as helicopters. Different methods that utilize various signals may be employed for fault detection. Vibration signals are among mostly used ones as they can provide valuable information about gearbox health condition. Vibrations can be generated either by the gearbox itself or be generated with a simulated dynamic model. In this study, both dynamic models and experimentally measured signals are employed simultaneously to develop a robust fault detection algorithm.

CHAPTER 2

LITERATURE REVIEW

In this part, first a survey of the published literature in the field of fault diagnosis of planetary gear systems will be carried out. Subsequently, considering the areas of the field that still can be developed and possible contributions, the research plan and methodology is presented.

2.1 Summary of literature

Gearboxes are of major constituent parts of many machineries in different industries. As any other machines, they require regular maintenance and if they are not monitored continuously, it can lead to sudden failures, and an increase in annual operating budget for the industries. Condition based maintenance (CBM) allows for continuous monitoring of the systems and fault prediction so that a planned maintenance based on the estimated fault level is carried out before a sudden failure occurs. Mesh stiffness and load variation in gearboxes, gives rise to vibrations. Many researchers utilize gear vibrations as informative data for the fault symptom diagnosis in gear systems. Although rich in information, they have generally low levels of signal to noise ratio (SNR).

Approaches taken by researchers to gear fault diagnosis can be classified into two major groups: model-based methods which utilize dynamic linear/non-linear models including different faults and data-driven methods which are based on data measured from faulty and healthy gears. The former are developed to gain further insight into how different faults influence the vibration response of a gearbox and consequently develop algorithms for condition monitoring via experimentally acquired data.

To aid fault detection through dynamic modeling, Parey et al [1] investigated the effect of tooth pitting on the vibrations of a spur gear pair. The surface pitting was modelled by a sinusoidal decaying pulse and its severity influence in the response was evaluated by crest factor and kurtosis analysis. Through a verification with experimental results, they showed the effectiveness of the proposed method of fault model. Another approach to include the pitting in the dynamic model is to estimate the amount of the change in mesh stiffness [2-3]. Chen et al [4] introduced a realistic crack effect in dynamic model of a multistage gear system in which they could see the influence of the crack initiation angle on the vibration signals. Another common type of tooth faults is spalling. Since it affects the shape of tooth it changes the stiffness of the tooth and hence the mesh stiffness compared with healthy gears. Therefore, a frequent approach is to consider its effect on mesh stiffness. Luo et [5] al proposed a general approach to model tooth spalls in any shape and investigated its effect on gear vibrations. This work can provide other authors with mesh stiffness of spalled gears in dynamic modelling. Other effects such as gear eccentricity, tooth profile modification and misalignment can be simultaneously included in dynamic models as well. This approach is advantageous in differentiating between different fault features. In an attempt to model the pits and spalling effects, Luo et al [6], proposed a dynamic model that considers the effects of tooth roughness change and geometric deviation due to surface pitting and spalling. They demonstrated that surface roughness changes result in sidebands in high frequencies with significant amplitudes in the resonance frequency. This is because the effect of local faults such as pitting and spalling reveals itself as sideband frequencies and peaks at many frequencies, especially in high frequencies. Gears demonstrate a non-linear dynamic behavior in the working condition; therefore, in the solution phase of the gear vibration equation sets, different approaches can be employed. For the spur gears, non-linearity stems from different sources from which the most important one is varying mesh stiffness that varies as a function of the gear rotation angle. Considering the relative orders of the gear mesh stiffness, bearing stiffness and shaft stiffness, there might be a coupling between the torsional and lateral vibrations. It is

shown in [7] that the gear system may exhibit diverse behavior ranging from periodic, sub-harmonic, and chaotic motion due to lateral-torsional coupling effects. Developing a complete dynamic non-linear gear model allows a realistic evaluation of diagnostic procedures. Most of authors preferred to establish a dynamic model which includes a single gear fault and there are few models which consider multiple faults with their interaction. Modelling is a forward problem at which the effects of faults are included in the mathematical models and the response (outputs) are calculated. The next step after the validation of models is to find algorithms that can unfold the complicated response patterns and detect faults using the available data. This is an inverse problem with its own difficulties. Each type of gear faults has certain effect on the gear vibration response and therefore might require specific methods to be detected. As it is expressed in [8], faults such as wear, pitting, chipping, scuffing, spalling, tooth breakage and white structure flaking are the major initiation causes of gearbox failures. Furthermore, it is stated that more investigations need to be performed on different and mixed fault modes and severities. This is because most of the authors have verified the effectiveness of the employed fault indicator solely for a special fault case. According to [9], spalls and pitting affect the tooth surface quality and mesh stiffness and it is hard to differentiate them through vibrations, although the change in the response is significant. Therefore, with a reliable non-linear dynamic model, development of proper fault detection and classification algorithms are of high importance.

Since dealing with large data is computationally expensive and unprocessed data does not provide highly correlated information, different methods are developed to extract fault sensitive extract features from signals. Gear vibration signals are non-stationary (or cyclostationary) in their nature and the obtained features may simultaneously depend on time and frequency. A method that is popular in feature extraction context and takes into account the frequency as well as time is wavelet transform. Barbieri et al [10] Showed that the use of wavelet transform in time domain could potentially detect a fault. However, in order to detect the fault type, i.e. gear or bearing, their associated characteristic frequency obtained by singular

value decomposition (SVD) must be used. One of the most important features of wavelet transforms is that it enables zooming in time or frequency domain and the investigation of instantaneous frequencies of the signals. However, resolution in the frequency domain might be low. In an attempt, Hu et al [11] introduced a high order synchrosqueezing wavelet transform that provides higher resolution in the estimation of instantaneous frequency and successfully used it in gear fault detection.

In the context of fault diagnosis, once there exist multiple fault types, the first task after the detection of a fault occurrence, is to identify the type of the fault which is called fault isolation. From pattern recognition point of view, this could be seen as a non-linear classification task which can be tackled by various methods. Different approaches have been developed for this purpose. Artificial Neural Networks (ANNs) and Support Vector Machines (or in a general class, Kernel based methods) are popular methods in this category. Sadeghi et al [12] adopted a method based on ANN for fault identification purpose and they showed the effectiveness of the method. ANNs are quite popular in the field of classification as it can aid the unsupervised classification process. Rafiee et al [13] utilized features from wavelet transform as an input to ANN based classifier to identify gear and bearing faults. Other classifiers such as fuzzy classifier has also been reported in fault identification process [14]. Simliar studies has been carried out in [15-17] where the issue of time varying operating conditions is of high concern.

Another complexity that arise during the analysis of gear vibration signals is that they are non-stationary and most of the common signal analysis methods are not readily applicable. Time-frequency methods such as Short Time Fourier Transform (STFT) and other FFT-based methods are generally applied on gear signals which can lead to acceptable results. Frequency domain analysis based on the Fourier transform is a primary yet powerful approach for detecting characteristic frequencies and fault symptoms. The biggest drawback of this method is the low frequency resolution. Alternatives to the FFT are Hilbert Huang Transform (HHT), Wigner Vile distribution, and wavelet transform (WT). For instance, WT enables zooming in frequency or time domain to investigate fault effects. However, it has limitations

in detecting specific faults, such as distributed faults. In spite of the limitations, the aforementioned methods are primarily helpful in fault detection rather than fault severity assessment.

FFT-based, stationary, or time-dependent approaches such as WT are among the most powerful planetary gear fault detection methods. Generally, modulation sidebands around mesh frequency and its harmonics are utilized as fault indicators. Many authors conducted studies by applying FFT on experimentally recorded signals [18-19] or a combination of theoretical and experimental data [20-22]. The former method focuses on advanced signal processing tools for fault detection. The latter type tries to develop a model that simulates an actual gearbox's behavior as precisely as possible such that the model represents the actual system and can aid in fault diagnosis. Most of the studies which employed FFT, analyze sideband frequencies around mesh frequency harmonics. Sidebands are generally analyzed because the variation of gear mesh stiffness in a meshing period generates mesh frequency, and its modulation with carrier and other frequencies results in sidebands. However, the gearbox dynamics, which can be expressed in terms of its natural frequencies and modal dampings, is affected by a fault. This fact has been employed by [23] to detect planetary gear faults. They reported time-varying sidebands around resonance frequencies which are thought to be excited by impulses generated due to faults.

Once a gear fault is detected, the next major step is determining the faulty gear. Different approaches can be used to achieve this goal. For instance, Time Synchronous Average (TSA)-based methods as employed in [24], where TSA signals are divided into several segments utilizing windows associated with each planet pass. Then the windowed signals are averaged to detect the faulty planet. The drawback of these methods is that they require considerably long measured signals. Detection of a faulty planet requires geometric information of its pass from the sensor location. Peng et al. [25] take a different approach to using mesh phasing of different planet gears. They traced the gear mesh component of the faulty gear's impulse response, making it distinguishable among the planets. For this purpose, an

internal sensor was mounted on the planet carrier. TSA can extract periodic waveforms due to faulty gears, and Wavelets enable zooming in time/frequency domains. A combination of the two mentioned methods is the core of the study [26], which enabled them to detect simultaneous faults. In the case of planetary gear fault, when a fixed sensor is mounted on the ring gear, the impulse effect during the meshing of the faulty tooth is transferred to the sensor from different paths. Different vibration transfer paths complicate fault diagnosis through only one fixed sensor. To consider such effects, Guo et al. [27] devised a method combining vibration separation, TSA, and demodulation. They transferred time domain signals to the angle domain using tachometer signals and applied narrowband demodulation on TSA signals to detect planet faults. In the angle domain, the mesh period of the gears can be followed to trace the faulty tooth impulsive mesh in the spectrum. Similar methods have been used in [28-29]. The problem with this method is that it requires precise speed and gear mesh information, making it quite challenging to apply in practice. Most fault diagnosis algorithms require geometric or kinematic information about the faulty gear to isolate it successfully. A method to achieve such information is through time-frequency methods, which capture the time-dependent effects of faults. Despite their great potential in gear fault detection, the authors have yet to employ parametric non-stationary time series models frequently. This research utilizes non-stationary time series models to achieve kinematic information about the faulty tooth mesh for planetary gear fault diagnosis.

Gear vibration signals are non-stationary, and most common signal analysis methods are not readily applicable. Compared to the other non-parametric empirical methods, such as Fourier-based methods, the time series models offer several advantages, such as parametric analysis of system dynamics represented by frequencies and dampings. Time series models are employed vastly in the field of structural condition monitoring. They represent a partial dynamic system model in a particular frequency interval. According to Wang [30], the effect of a spur gear fault is periodic and synchronous with shaft speed. Therefore, it can be best detected by Synchronously Averaged time domain signals (typically in the angle domain). They showed that

when there is a fault, the residual of the signal's Autoregressive (AR) model does not have a Gaussian random distribution, and there will be spikes in the spectrum. Chen et al. [31] proposed a method based on the AR model with varying coefficients that aid in identifying the correlation between the rotating phase and AR coefficients. They claimed the method is more efficient than Support Vector Machines (SVM) for detecting tooth root crack for a randomly varying speed case. There have been attempts to detect and estimate faults using time series models as in [32-34]. Modeling gear vibrations, in general necessitates the use of non-stationary models. Many authors have conducted fault diagnosis via time series models. Linear parameter varying Autoregressive Moving Average (LPV-ARMA) [35-36], LPV-VAR [37], Time-Dependent ARMA (TARMA) [38-39], Functional Series TARMA (FS-TARMA) [40-42] and Vector Functionally Pooled ARMA (VFP-ARMA) [43] are among the typically used times series models for fault detection. The idea behind VFP-ARMA and generally the Functionally Pooled (FP) models [44, 45] is to obtain a global model that includes the variation of operating conditions inside the Vector ARMA (VARMA) model. In the LP-VAR method, the coefficients are functions of rotating phase and speed, which allows for considering the variation of operating conditions. The general approach in fault detection via time series models is to generate residuals using an estimated baseline model. A hypothesis test is subsequently carried out to determine whether the residual satisfies the normality condition, and based on the result, a fault is detected. Fault detection of gearboxes operating in varying load conditions with Autoregressive with Exogenous Input (ARX) model utilizing time-synchronously averaged (TSA) signals by applying F-test on the residuals has been attempted in [46]. Similar methods were used in [47], where AR models fitted to the healthy signals were employed as a baseline to detect the fault based on the normality test of given signals collected at different operating conditions. AR models do not account for non-stationarity, and various methods can be adopted to tackle the problem. For instance, for the particular case of periodically varying operating conditions, Periodic AR (PAR) model has been suggested in [48].

TARMA model is different from its stationary counterpart ARMA, in the sense that the model parameters are time-dependent, which allows for taking into account the change of system parameters or non-stationarity of the vibration signals. Stationary models, including AR, ARMA, ARX are generally utilized for modeling stationary signals, although they can tackle weak non-stationarity to some extent. Time series models offer great potential for the fault detection of mechanical systems, especially gearboxes. Most studies that employed time series models put effort into considering varying operating conditions inside fault detection algorithms such that they function precisely under different operating conditions. However, none considered modeling gear signals' non-stationary behavior via non-stationary models such as TAR or TARMA.

This study aims to improve planetary gear systems' fault detection process via time-frequency analysis of vibration signals using non-stationary time series approach and non-linear dynamic modeling of a planetary gear system with concentrated gear fault. In time series approach, the FS-TAR and FS-TARMA models will estimate the non-stationary gear vibration signals. It will allow for following time-dependent fault signatures at different frequency ranges. The estimated time series models associated with faulty and healthy gears will be compared with a metric which provide Euclidean distance called $AR(\infty)$ metric to detect the fault. Linear and non-linear dynamic models of a planetary gear with gear fault will be developed to aid diagnosis through the effects that faults impose on vibration response in the frequency domain.

The methodology of fault detection with the mentioned methods is described in the next subsection.

2.2 Methodology

Here, FS-TAR and FS-TARMA approaches will be used to represent non-stationary signals by time-dependent parameteric models. The core idea of the study is that, an

FS-TARMA (FS-TAR) model can precisely estimate the vibration signals and identity gearbox partial dynamics. The obtained model will make it possible to observe the variation in model dynamics in one revolution of planet carrier. The hypothesis is that any fault, other than affecting system's natural frequencies, will have an impulsive effect on the response when a faulty tooth enters a mesh with other gears. Such impulses can stimulate specific operating modes (frequencies) in the gearbox and change the dynamics of gear system in a short period. These changes which are localized in time, can best be estimated via parametric non-stationary models. To test the applicability of the approach, experimentally collected vibration signals will be used. In addition, a non-linear dynamic model of planetary gearbox with gear faults will simultaneously aid the aforementioned fault detection process. A gear dyanmic model can provide an insight into the fault influence mechansims on the response of the gearbox. It is expected to achieve a more effective fault detection algorithm based on a fusion of the data provided by non-stationary signal models and non-linear dynamic model. Figure 2.3. illustrates the process of fault detection employing the mentioned methods.

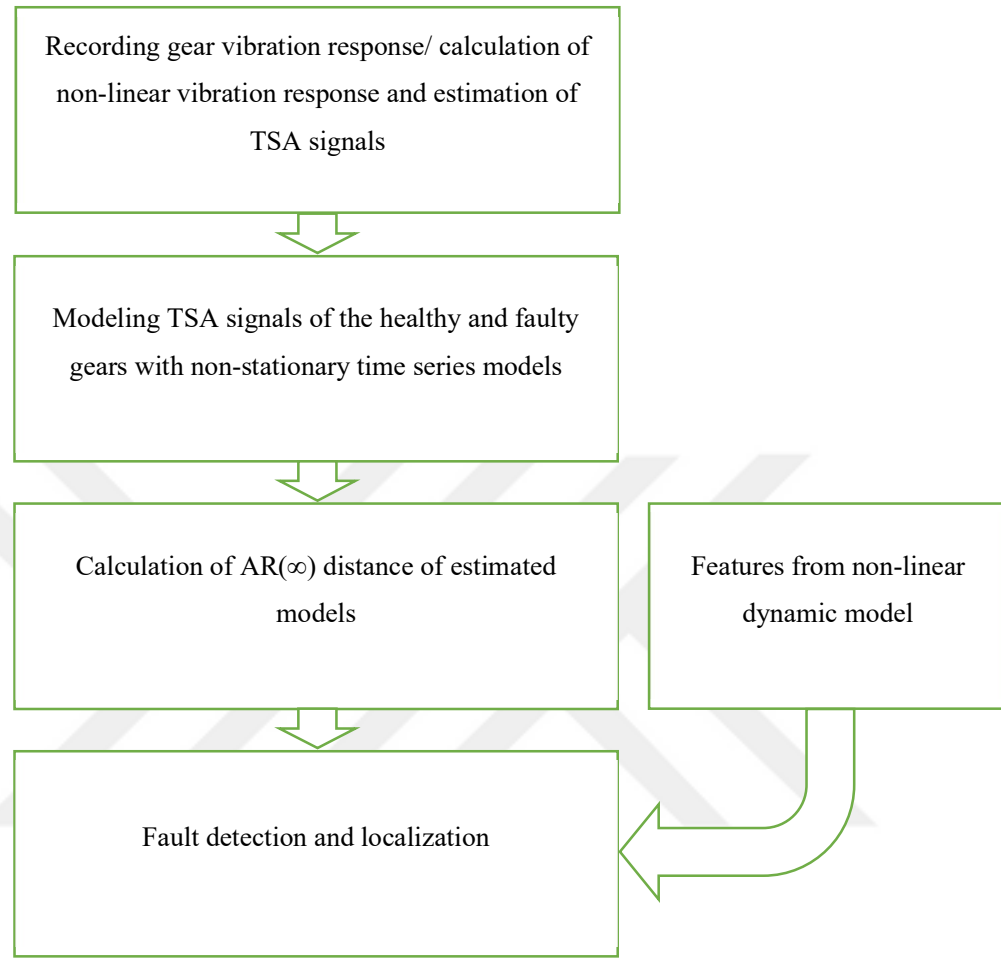


Figure 2.1 Fault detection process based on comparison of time series

2.3 Contributions to the field

The main contributions of the research are

- The use of FS-TAR and FS-TARMA approaches for the first time to estimate non-stationary planetary gearbox signals,
- Fault detection and isolation only by using a non-stationary FS-TAR model,
- Development of a method for the estimation of a cracked gear mesh stiffness. The developed method can facilitate the process of including the crack effect in dynamic models.

2.4 Objectives and scope

The objectives and scope of the study are

- Vibration-based gear fault detection via non-stationary time series approach,
- Only one type of fault is considered and a fault classification will not be carried out,
- The methods based on FFT analysis will be used as a primary tool of fault diagnosis,
- WT will be used to support the fault detection through time-frequency analysis.
- The non-linear dynamic model of the gearbox is used as a complementary tool of fault detection.
- The stability analysis of the non-linear model will not be of concern,

CHAPTER 3

Dynamic modeling of a planetary gearbox

In the current chapter, dynamic modeling of a planetary gearbox is presented. First, a linear model is developed and through a modal analysis and comparison of results with the ones available in literature, it is validated. At the next step, non-linear dynamic model of the planetary gearbox is developed. Since the final goal of the chapter is to model the fault effects on the response of a planetary gearbox, a method should be developed to allow the inclusion of faults in the dynamic model. As a primary step toward this goal, a non-linear dynamic model of a spur gear pair with gear faults such as tooth root crack and pitting is developed and verified. Having established a solid background for fault modeling, in the last part a non-linear dynamic model of a planetary gearbox is developed and simulated. The simulation results will provide an aid to gear diagnostics.

3.1 Linear dynamic model

In this part, dynamic modelling of a planetary gearbox will be realized. The gearbox considered in this study consists of a sun gear, ring gear, three planets, and a carrier. In order to do a complete analysis, ring is also assumed to be moving. The sun gear is connected to the input shaft and the input torque is applied to it while the output is carrier motion. Schematic view of the gearbox is shown in Fig 3.1. In the dynamic model, all the gears are assumed to be rigid other than the teeth which are flexible. Sun, planets, carrier and ring gear each have three degrees of freedom (DOFs) of which two are translational and one is rotational DOF. Therefore, the planetary gear system will have eighteen DOFs. The mass, mass moment of inertia, and pitch radius of the sun are shown by m_s, I_s, R_s respectively. For the carrier, mass, mass moment of inertia and the radial distance are denoted by m_c, I_c, R_c respectively. m_p, I_p ,

R_p represent the mass, mass moment of inertia and pitch radius of the planets. The stiffness of the sun, planet and carrier bearings are denoted by k_s, k_p, k_c respectively. Damping of the bearings is neglected in this phase of modeling.

In Fig 3.2, the planar motions of the sun gear, carrier and planetary gear along the DOFs are shown. Sun gear has two translational DOFs shown as x_s, y_s and one rotational DOF θ_s . Similarly for the carrier, the DOF are x_c, y_c, θ_c . In the same way the DOF of the ring gear are defined as x_r, y_r, θ_r . Considering the DOFs, displacement vector of sun, \mathbf{r}_s , and displacement vector of carrier, \mathbf{r}_c can be written as

$$\mathbf{r}_s = x_s \mathbf{i} + y_s \mathbf{j}, \mathbf{r}_c = x_c \mathbf{i} + y_c \mathbf{j} \quad (3.1)$$

According to Fig 23 (b), Absolute position of planet i , can be expressed as

$$\mathbf{r}_i = \mathbf{r}_c + \mathbf{r}'_i + \boldsymbol{\rho}_i \quad (3.2)$$

where \mathbf{r}'_i represents position vector from carrier center to planet location and $\boldsymbol{\rho}_i$ is displacement vector of planet with respect to the carrier.

Displacement vectors \mathbf{r}'_i and $\boldsymbol{\rho}_i$ are written as follows

$$\mathbf{r}'_i = R_c [\cos(\theta_c + \varphi_i) \mathbf{i} + \sin(\theta_c + \varphi_i) \mathbf{j}], \boldsymbol{\rho}_i = \xi_i \mathbf{e}_i^\xi + \eta_i \mathbf{e}_i^\eta \quad (3.3)$$

where R_c is the radial distance from carrier center to planet center, ξ_i is the motion in the radial direction between carrier and planet, \mathbf{e}_i^ξ represents unit vector, η_i is the motion in the direction normal to ξ_i , \mathbf{e}_i^η is unit vector and φ_i denotes initial circumferential position of planetary gears which are $\varphi_1 = 0^\circ, \varphi_2 = 120^\circ, \varphi_3 = 240^\circ$.

Position vector of the planet i , \mathbf{r}_i can be written as

$$\mathbf{r}_i = x_i \mathbf{i} + y_i \mathbf{j} \quad (3.4)$$

$$x_i = x_c + (R_c + \xi_i) \cos(\theta_c + \varphi_i) - (R_c + \eta_i) \sin(\theta_c + \varphi_i)$$

$$y_i = y_c + (R_c + \xi_i) \sin(\theta_c + \varphi_i) - (R_c + \eta_i) \cos(\theta_c + \varphi_i)$$

It has to be noted that the absolute rotational angle of planet i is obtained as $\theta_c + \theta_i$, where θ_i is the rotation angle measured with respect to the carrier.

Since the gear teeth are flexible, while the gears are in mesh, the overall stiffness forms an stiffness called mesh stiffness. In order to find the force induce by the meshing, the gear mesh deformation must be calculated in terms of the displacements. The Gear mesh deformation between i -th planet and sun can be expressed as

$$\begin{aligned} \delta_i^s = & [x_s - x_i + R_c \cos(\theta_c + \psi_i)] \sin(\alpha_i^s - \psi_i^s) + \\ & [y_s - y_i + R_c \sin(\theta_c + \psi_i)] \cos(\alpha_i^s - \psi_i^s) + R_s(\theta_s - \theta_c) + R_p \theta_i \end{aligned} \quad (3.5)$$

where R_s is the sun base radius, R_p represents planet base radius, α_i^s is the pressure angle between i -th planet and sun and ψ_i^s shows the angular position of i -th planet with respect to sun. the mesh deformation is the deformation of the stiffness element between the two meshing gears as shown in Fig 3.3.

In the same way, gear mesh deformation between i -th planet and the ring (see Fig 3.4) can be shown as

$$\begin{aligned} \delta_i^r = & [x_i - R_c \cos(\theta_c + \psi_i)] \sin(\alpha_i^r + \psi_i^r) \\ & - [y_i - R_c \sin(\theta_c + \psi_i)] \cos(\alpha_i^r + \psi_i^r) - R_r \theta_c - R_p \theta_i \end{aligned} \quad (3.6)$$

where ψ_i^r is position angle of i -th planet with respect to the ring, and R_r represents base radius of ring.

When the mesh stiffness is assumed to be time varying, the contact ratio comes into play. It can be written as

Contact ratio between planet and sun m_i^s

$$m_i^s = \frac{\sqrt{A_s^2 - R_s^2} + \sqrt{A_p^2 - R_p^2} - R_c \sin(\alpha_i^s)}{p_b} \quad (3.7)$$

where A_p, A_s are radii of addendum of planet and sun and p_b is base pitch of planetary gear

Contact ratio between planet and ring m_i^r

$$m_i^r = \frac{\sqrt{A_p^2 - R_p^2} - \sqrt{A_r^2 - R_r^2} - R_c \sin(\alpha_i^r)}{p_b} \quad (3.8)$$

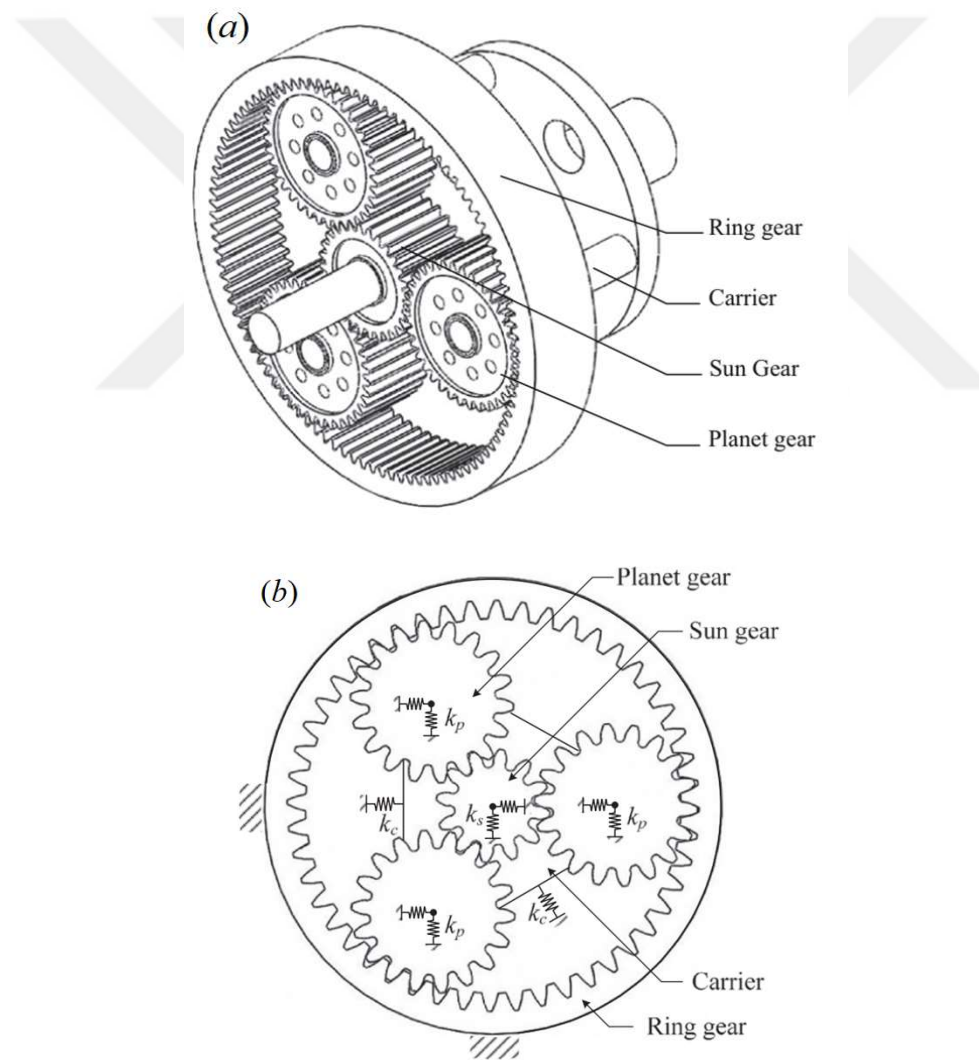


Figure 3.1 Schematic view of the planetary gearbox with three planets [49]

In the easiest form, the mesh stiffness between planet and ring, and planet and sun can be shown as in Fig 3.5, where $T_m = \frac{2\pi}{n_p \omega_p}$ is the mesh period. Here, the mesh stiffness is estimated via Fourier series as function of time with fifteen harmonics. This way, it can be easily used in numerical simulations.

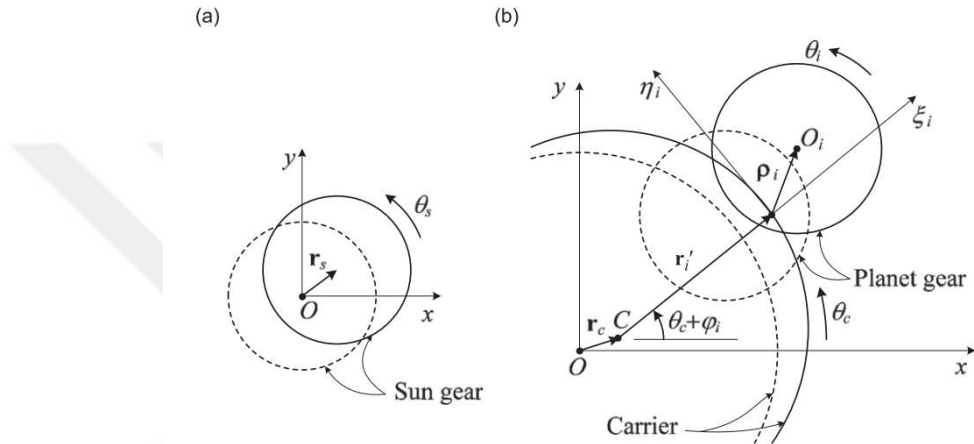


Figure 3.2 a) planar motion of the sun gear, b) the planet gear and carrier; the dashed and solid lines: positions before and after motion [49]

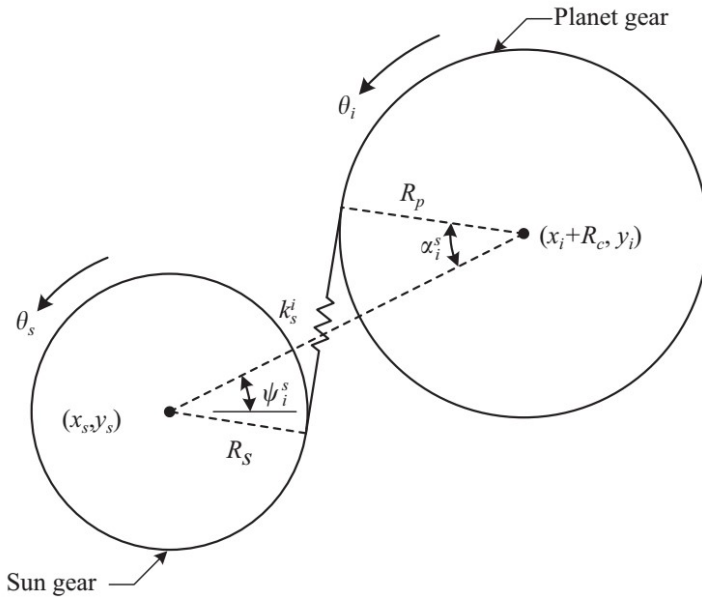


Figure 3.3 meshing between the sun and a planet [49]

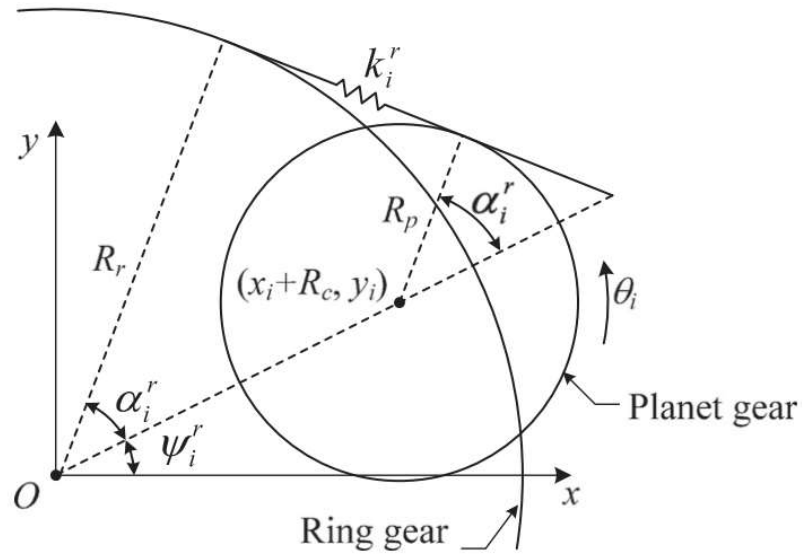


Figure 3.4 meshing between the ring and a planet [49]

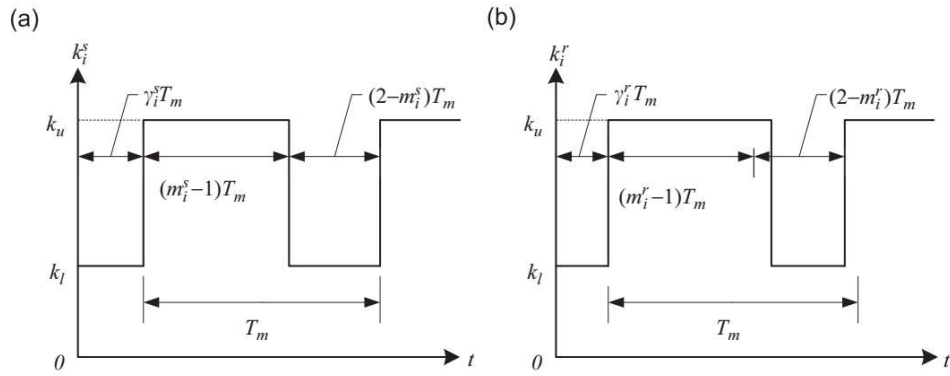


Figure 3.5 Gear mesh stiffness between a) planet i and ring and sun, b) ring gear and planet i [49]

Having calculated all the displacements and deformations, the potential and kinetic energy of the system can be obtained. then, using the Lagrange's equations (Eq 3.9), equations of motion are derived.

$$\frac{d}{dt}\left(\frac{\partial T}{\partial \dot{q}_i}\right) - \frac{\partial T}{\partial q_i} + \frac{\partial V}{\partial q_i} = Q_i, \quad (3.9)$$

Degrees of freedom can be shown in a vector form as

$$q_i = \{y_s, x_s, \theta_s, y_c, x_c, \theta_c, \eta_1, \xi_1, \theta_1, \eta_2, \xi_2, \theta_2, \eta_3, \xi_3, \theta_3\} \quad (3.10)$$

The kinetic and potential energies are obtained as

$$\begin{aligned} T &= \frac{1}{2} [m_s(\dot{x}_s^2 + \dot{y}_s^2) + I_s \dot{\theta}_s^2] + \frac{1}{2} [m_c(\dot{x}_c^2 + \dot{y}_c^2) + I_c \dot{\theta}_c^2] \\ &\quad + \sum_{i=1}^3 \frac{1}{2} [m_p(\dot{x}_i^2 + \dot{y}_i^2) + I_i(\dot{\theta}_c + \dot{\theta}_i)\dot{\theta}_i^2] \\ V &= \frac{1}{2} k_s(x_s^2 + y_s^2) + \frac{1}{2} k_c(x_c^2 + y_c^2) + \sum_{i=1}^3 \frac{1}{2} [k_p(\xi_i^2 + \eta_i^2) + k_i^s(\delta_i^s)^2 + \\ &\quad k_i^r(\delta_i^r)^2] \end{aligned} \quad (3.11)$$

The potential and energy terms are plugged into the Lagrange's equations and after the linearization, the equations of motion are obtained. Before attempting at time domain solution of the equations of motion, first a modal analysis using average stiffness is carried out and the model is verified by results available in the literature. It has to be noted that here, for the planets. Relative coordinates are used, while they can be absolute as well.

3.1.1 Linear dynamic response of the gear system

In this subsection, the response of linear dynamic system is evaluated. Before time simulation, first a modal analysis is carried out to verify the model using the available results in the literature.

The values of parameters used for the validation are given in table 3.1.

Table 3.1 Parameter values used in the simulations [50]

	Sun	Ring	carrier	Planet
Mass (kg)	0.4	2.35	5.43	0.66
Mass moment of inertia divided by the radius $\frac{J}{r^2}$ (kg)	0.39	3	6.29	0.61
Base diameter(mm)	77.4	275.0	176.8	100.3
Mesh stiffness (N/mm)	$k_i^s = k_i^r = 5 \times 10^8$			
Bearing stiffness (N/mm)	$k_p = k_s = k_r = 10^8$			
Torsional stiffness (Nm/rad)	$k_{ru} = 10^9$, $k_{su} = k_{cu} = 0$			
Pressure angle (deg)	$\alpha_s = \alpha_r = 24.6^\circ$			

Using the parameters in the Table 3.1, Natural frequencies and with a multiplicity of m are obtained as shown in Table 3.2. As it can be noticed, the obtained frequencies compare well with the results given in the literature [50]. Therefore, the model is verified and it can be used for further analysis.

A number of the mode shapes are presented in the Figs 3.6-3.11. They are obtained using the relative coordinate system and if absolute coordinates are used for the planet bearings, the results would be different.

Table 3.2 frequencies with multiplicity m and number of planets N

N = 3		
	Reference [50]	Computed
m = 1	0	0
	1475.7	1476.3
	1930.3	1930.4
	2658.3	2663.6
	7462.8	7463.6
	11775.3	11775.3
m = 2	743.2	743.17
	1102.4	1102.4
	1896.0	1896.0
	2276.4	2276.4
	6986.3	6986.3
	9647.9	9647.9

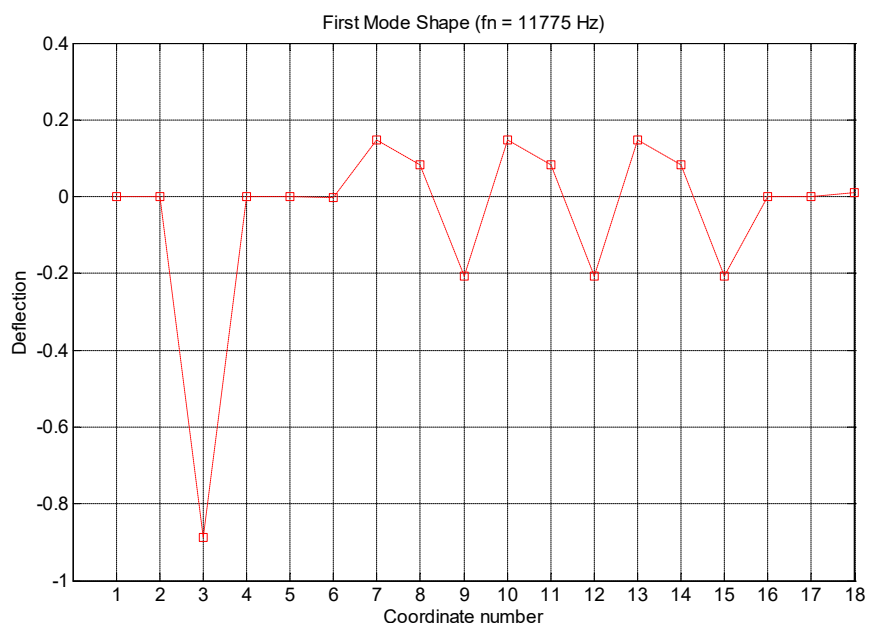


Figure 3.6 First mode of the planetary gearbox

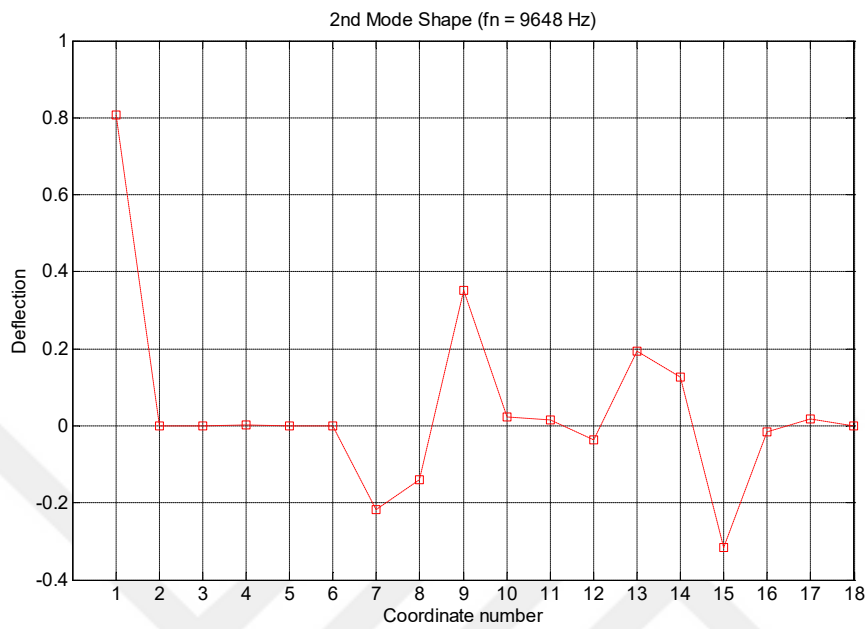


Figure 3.7 Second mode of the planetary gearbox

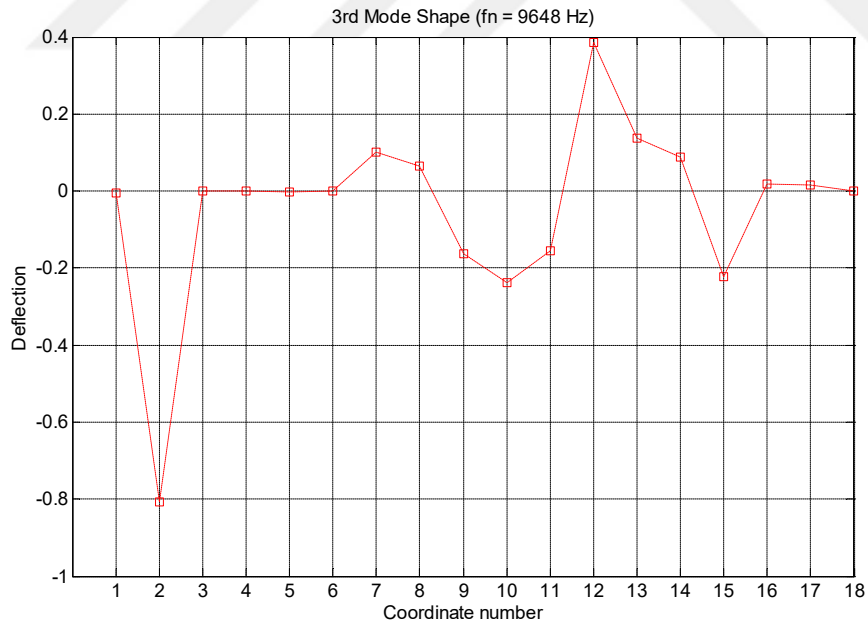


Figure 3.8 The third mode of the planetary gearbox

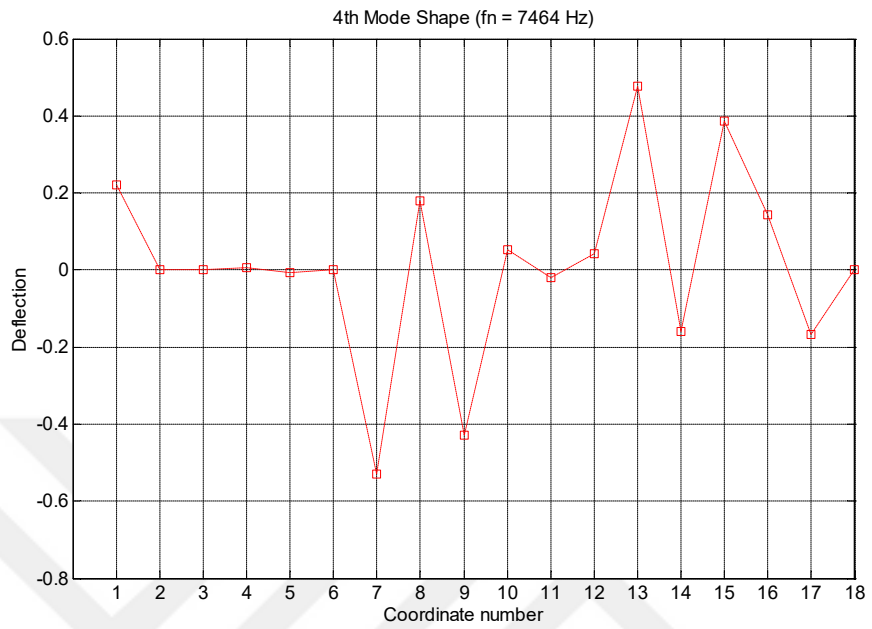


Figure 3.9 The fourth mode of the planetary gearbox

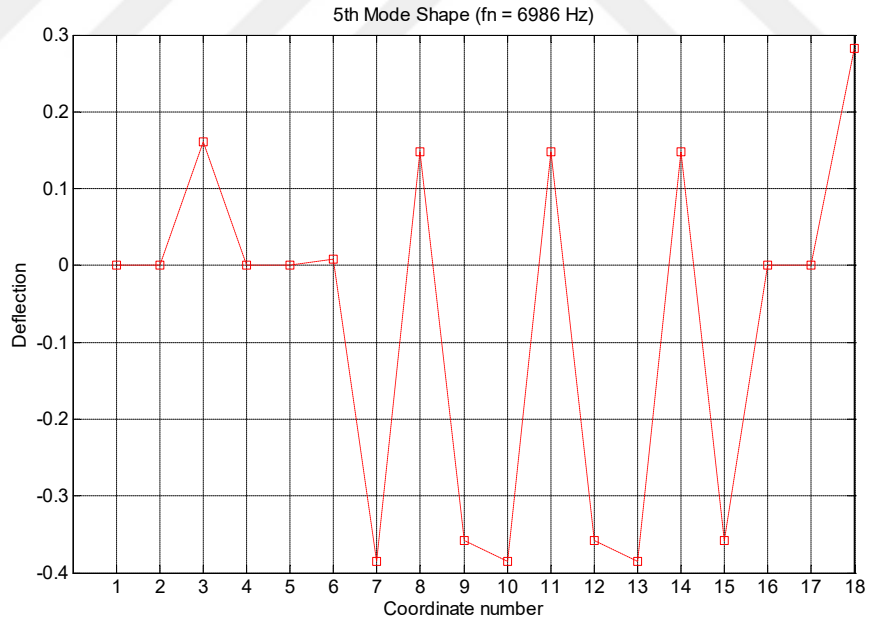


Figure 3.10 The fifth mode of the planetary gearbox

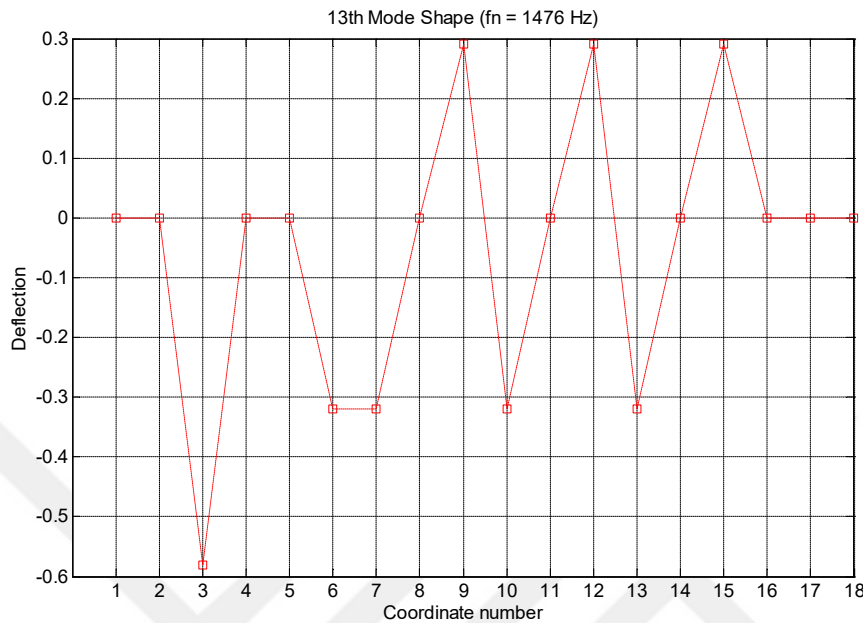


Figure 3.11 The mode thirteen of the planetary gearbox

3.2 Non-linear dynamic model

In this section, before attempting to model the non-linear vibrations of planetary gearbox, a non-linear model of a spur gear pair with the inclusion of gear faults and errors is established and solved. It will provide a basis for the analysis of fault effects on dynamic response in time and frequency domains. It has great significance as it helps understanding the fault modeling methods and fault influence mechanisms in a gear system.

3.2.1 Non-linear dynamic modeling of a spur gear pair with gear faults

In the current subsection, in order to gain insight on how to model the faults in a gear system, a non-linear dynamic model of a six DOF spur gear pair is developed and the effects of different faults including gear tooth crack and surface pitting are included in the model. This is carried out prior to modeling planetary gearbox with

fault effects because inclusion of faults in planetary gear systems is more complicated due to the multiple meshing nature of planetary gears. Therefore, this part mainly includes

- a) Non-linear dynamic modeling of a spur gear system without faults
- b) Non-linear dynamic model with inclusion of tooth root crack and pitting
- c) Investigation of the effects of faults on dynamic response in time and frequency domains
- d) Simulation results

3.2.1.1 Modeling

The purpose of this part is to develop a non-linear dynamic model of a spur gear pair which includes the effect of coupling between torsional and lateral vibrations. In this non-linear model, the time varying mesh stiffness, backlash, and gear errors are included.

The six DOF dynamic model of this study is show in Fig 3.12. This model includes four rotational DOFs (of prime mover, pinion, gear and load), and two lateral motions of the pinion and gear along the action line which in total becomes six DOF. The effects which are included in the dynamic model and hence are considered in the dynamic analysis, constitute of:

- 1- Time varying mesh stiffness and damping,
- 2- Torsional flexibility of pinion and gear shafts,
- 3- Torsional damping of shafts,
- 4- Lateral flexibility of shafts,
- 5- Stiffness and damping of bearings,
- 6- Inertia of prime mover and load,
- 7- Input and load torques,

- 8- Teeth separation during meshing,
- 9- Backlash and backside collision,
- 10- Tooth root crack
- 11- Tooth surface pitting.

The dynamic analysis is done in the plane of the gears and out of plane motions are ignored. The effects of friction between the teeth in mesh is neglected as well. Taking into account the assumptions and Fig 3.12, the equations of motion can be obtained.

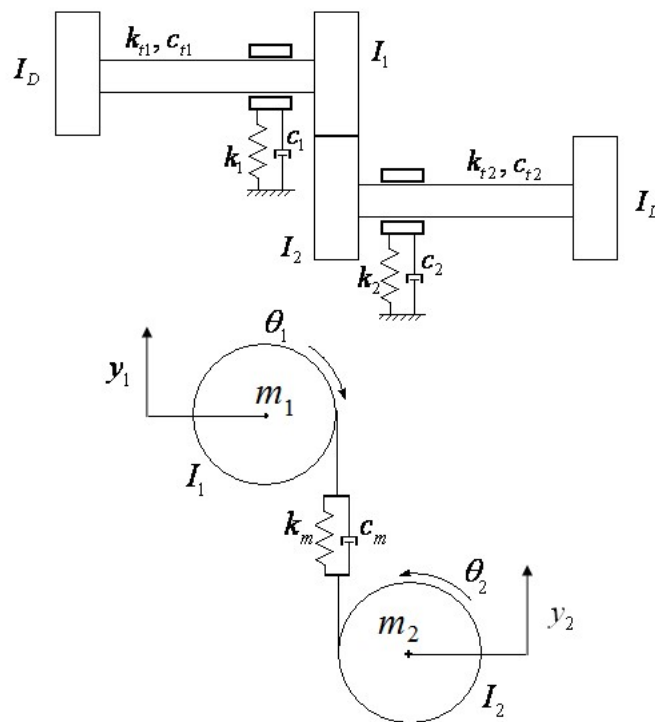


Figure 3.12 Dynamic model of a spur gear pair [1]

The equations of motion can be obtained using either Newton's second law or Lagrange's method. The result will be as expressed in equations (3.12)-(3.17)

$$I_D \ddot{\theta}_D + k_{t1} \theta_D - k_{t1} \theta_1 + c_{t1} \dot{\theta}_D - c_{t1} \dot{\theta}_1 = T_D \quad (3.12)$$

$$I_1 \ddot{\theta}_1 - k_{t1} (\theta_D - \theta_1) - c_{t1} (\dot{\theta}_D - \dot{\theta}_1) + k_m r_1 (y_1 - y_2 + r_1 \theta_1 - r_2 \theta_2) + c_m r_1 (\dot{y}_1 - \dot{y}_2 + r_1 \dot{\theta}_1 - r_2 \dot{\theta}_2) = 0 \quad (3.13)$$

$$I_2 \ddot{\theta}_2 - k_m r_2 (y_1 - y_2 + r_1 \theta_1 - r_2 \theta_2) - c_m r_2 (\dot{y}_1 - \dot{y}_2 + r_1 \dot{\theta}_1 - r_2 \dot{\theta}_2) + c_{t2} (\dot{\theta}_2 - \dot{\theta}_L) = 0 \quad (3.14)$$

$$I_L \ddot{\theta}_L + k_{t2} (\theta_2 - \theta_L) + c_{t2} (\dot{\theta}_2 - \dot{\theta}_L) = T_L \quad (3.15)$$

$$m_1 \ddot{y}_1 + k_1 y_1 + k_m (y_1 - y_2 + r_1 \theta_1 - r_2 \theta_2) + c_m (\dot{y}_1 - \dot{y}_2 + r_1 \dot{\theta}_1 - r_2 \dot{\theta}_2) = 0 \quad (3.16)$$

$$m_2 \ddot{y}_2 + k_2 y_2 - k_m (y_1 - y_2 + r_1 \theta_1 - r_2 \theta_2) - c_m (\dot{y}_1 - \dot{y}_2 + r_1 \dot{\theta}_1 - r_2 \dot{\theta}_2) = 0 \quad (3.17)$$

The equations given above can be transformed to a matrix form with mass, damping and stiffness matrices as follows

$$M = \begin{bmatrix} I_D & 0 & 0 & 0 & 0 & 0 \\ 0 & I_1 & 0 & 0 & 0 & 0 \\ 0 & 0 & I_2 & 0 & 0 & 0 \\ 0 & 0 & 0 & I_L & 0 & 0 \\ 0 & 0 & 0 & 0 & m_1 & 0 \\ 0 & 0 & 0 & 0 & 0 & m_2 \end{bmatrix} \quad (3.18)$$

$$K = \begin{bmatrix} k_{t1} & -k_{t1} & 0 & 0 & 0 & 0 \\ -k_{t1} & k_{t1} & 0 & 0 & 0 & 0 \\ 0 & k_{t2} & -k_{t2} & 0 & 0 & 0 \\ 0 & -k_{t2} & k_{t2} & 0 & 0 & 0 \\ 0 & 0 & 0 & 0 & k_1 & 0 \\ 0 & 0 & 0 & 0 & 0 & k_2 \end{bmatrix} \quad (3.19)$$

$$C = \begin{bmatrix} c_{t1} & -c_{t1} & 0 & 0 & 0 & 0 \\ -c_{t1} & c_{t1} & 0 & 0 & 0 & 0 \\ 0 & c_{t2} & -c_{t2} & 0 & 0 & 0 \\ 0 & -c_{t2} & c_{t2} & 0 & 0 & 0 \\ 0 & 0 & 0 & 0 & c_1 & 0 \\ 0 & 0 & 0 & 0 & 0 & c_2 \end{bmatrix} \quad (3.20)$$

Tooth mesh force can be expressed as

$$F_m = K_d \begin{Bmatrix} X \\ \dot{X} \end{Bmatrix} \quad (3.21)$$

where

$$X = \begin{Bmatrix} \theta_D \\ \theta_1 \\ \theta_2 \\ \theta_L \\ y_1 \\ y_2 \end{Bmatrix}, \quad \dot{X} = \begin{Bmatrix} \dot{\theta}_D \\ \dot{\theta}_1 \\ \dot{\theta}_2 \\ \dot{\theta}_L \\ \dot{y}_1 \\ \dot{y}_2 \end{Bmatrix} \quad (3.22)$$

$K_d =$

$$\begin{bmatrix} 0 & 0 & 0 & 0 & 0 & 0 & 0 & 0 & 0 & 0 & 0 & 0 \\ 0 & -k_m r_1^2 & k_m r_1 r_2 & 0 & -k_m r_1 & k_m r_1 & 0 & -c_m r_1^2 & c_m r_1 r_2 & 0 & -c_m r_1 & c_m r_1 \\ 0 & k_m r_2 r_1 & -k_m r_2^2 & 0 & k_m r_2 & -k_m r_2 & 0 & c_m r_2 r_1 & -c_m r_2 r_1 & 0 & c_m r_2 & -c_m r_2 \\ 0 & 0 & 0 & 0 & 0 & 0 & 0 & 0 & 0 & 0 & 0 & 0 \\ 0 & -k_m r_1 & k_m r_2 & 0 & -k_m & k_m & 0 & -c_m r_1 & c_m r_2 & 0 & -c_m & c_m \\ 0 & k_m r_1 & -k_m r_2 & 0 & k_m & -k_m & 0 & c_m r_1 & -c_m r_2 & 0 & c_m & -c_m \end{bmatrix} \quad (30.23)$$

Forces other than mesh force, are classified as external force given as follows

$$F_e = \begin{Bmatrix} T_D \\ 0 \\ 0 \\ T_L \\ 0 \\ 0 \end{Bmatrix} \quad (3.24)$$

Total force on the right-hand side of the equations can be calculated as

$$F = F_m + F_e \quad (3.25)$$

In the forthcoming subsection, the calculation process of mesh stiffens is described

3.2.1.2 Mesh stiffness

Mesh stiffness between two gears in contact, consists of two parts. The former is related to Hertzian deflection and the latter is associated with the bending flexibility of the gear tooth. Hertzian stiffness per unit length of gear width was first calculated by Yang [51] as

$$k_h = \frac{\pi E}{4(1-\gamma^2)} \quad (3.26)$$

where E is the Young's modulus of elasticity and γ denotes Possion's ratio.

An equation for the calculation of bending stiffens of a gear too with modified addendum, has been introduce by Kuang and Yang [52]. Stiffness per unit length of tooth width $k_i(r)$ for a tooth i at a loading position r can be estimated using the following equation [52]

$$k_i(r) = (A_0 + A_1 X_i) + (A_2 + A_3 X_i) \left[\frac{(r-R_i)}{(1+X_i)m} \right] \quad (3.27)$$

where bending stiffness per unit length of tooth face width $k_i(r)$ is measured in $N/(\mu m/mm)$. X_i is the addendum modification coefficient. Radial distance r and the pitch circal radius R are measure in mm . The coefficients obtained from curve fitting are given as follows [52]

$$A_0 = 3.867 + 1.612N_i - 0.02916N_i^2 + 0.0001553N_i^3, \quad (3.28)$$

$$A_1 = 17.06 + 0.7289N_i - 0.01728N_i^2 + 0.0000999N_i^3, \quad (3.29)$$

$$A_2 = 2.637 - 1.222N_i + 0.02217N_i^2 - 0.0001179N_i^3, \quad (3.30)$$

$$A_3 = -6.330 - 1.033N_i + 0.02068N_i^2 - 0.0001130N_i^3 \quad (3.31)$$

where N_i is the number of gear teeth.

The mesh stiffness can be obtained by combining the bending stiffness of teeth in contact between meshing gears.

According to Fig 3.13, the mesh stiffness of a pair of teeth in mesh at contact points A and B can be obtained by the combination of stiffness per unit width $k_1(r_{1A})$, $k_2(r_{2A})$, $k_1(r_{1B})$, $k_2(r_{2B})$, and k_h of the teeth in contact, as springs in series connection as follows [1]:

$$\frac{1}{k_a} = \frac{1}{k_1(r_{1A})} + \frac{1}{k_2(r_{2A})} + \frac{1}{k_h} \quad (3.32)$$

$$\frac{k_a}{f} = \frac{[k_1(r_{1A})k_2(r_{2A})k_h]}{[k_1(r_{1A})k_2(r_{2A})+k_1(r_{1A})k_h+k_2(r_{2A})k_h]} \quad (3.33)$$

$$\frac{1}{k_b} = \frac{1}{k_1(r_{2B})} + \frac{1}{k_2(r_{2B})} + \frac{1}{k_h} \quad (3.34)$$

$$\frac{k_b}{f} = \frac{[k_1(r_{1B})k_2(r_{2B})k_h]}{[k_1(r_{1B})k_2(r_{2B})+k_1(r_{1B})k_h+k_2(r_{2B})k_h]} \quad (3.35)$$

where k_a and k_b represent a pair of teeth 1 and 2 in contact points A and B, respectively and are measured in $\frac{N}{mm}$. f denotes the face width of the gear and k_h is the Hertzian stiffness per unit width of the tooth.

In the equations (3.32)-(3.35), the stiffness is a function of radial distance r which is the radial distance of contact point from the gear center. In order to find the relationship between r and the rotation angle of gears, the involute profile of gears must be taken into account.

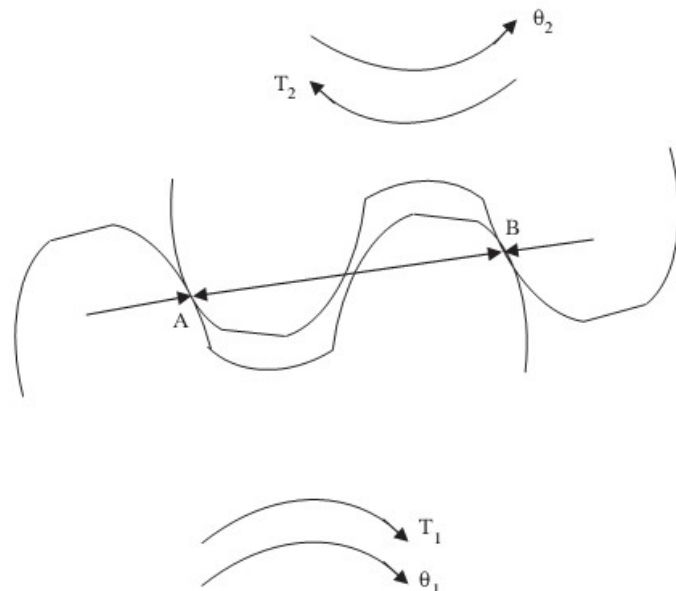


Figure 3.13 Dynamic model of a spur gear pair [1]

Time varying mesh damping can be approximated by the following equation [53]

$$C_m = 2\zeta(k_m m_e)^{1/2} \quad (3.36)$$

where m_e is the equivalent mass of the pinion and gear and it is defined as in equation (3.37) [53]

$$m_e = \frac{I_1 I_2}{I_1 R_2^2 + I_2 R_1^2} \quad (3.37)$$

Contact ratio

Since the contact ratio between meshing gears is generally greater than unity, according to the contact position of gears, at a specific instant, two or more pairs of teeth might be in mesh, this phenomenon can be seen in Fig 3.14.

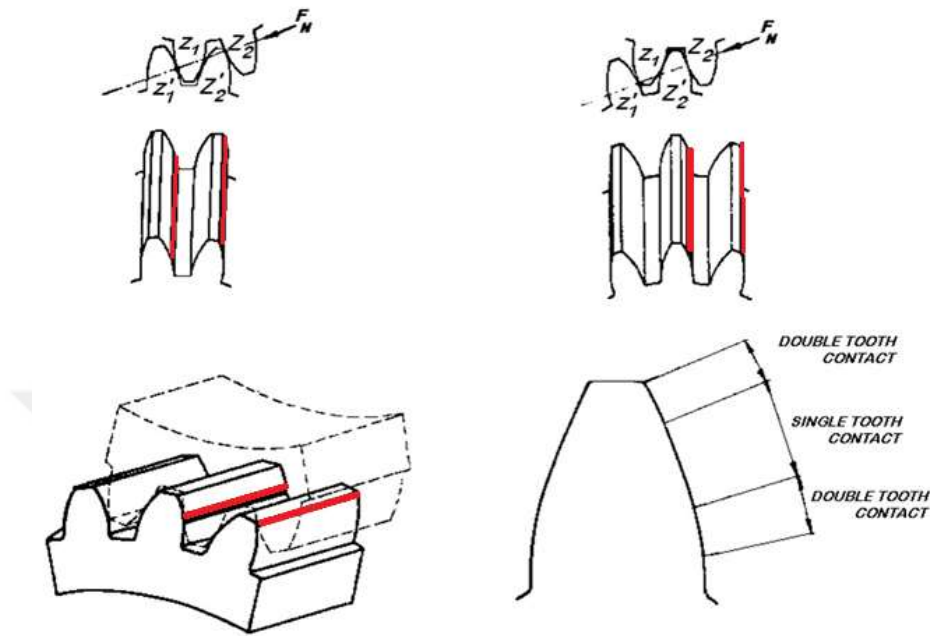


Figure 3.14 Meshing steps and the number of teeth in contact [54]

Contact ratio between the teeth in contact is defined as follows [54]:

$$CR = \frac{\text{Angle of action}}{\text{Pitch angle}} \quad (3.38)$$

The total time interval at which a tooth is in contact, is calculated by equation (3.39) [54]

$$t_{mesh} = CR \times \theta \quad (3.39)$$

where θ is the angular pitch as is obtained from the following equation

$$\theta = \frac{z}{m} \quad (3.40)$$

m and z are module and number of teeth for the gear. The time intervals at which double and a single pair of teeth are in mesh, are obtained from the equations (3.41) and (3.42) respectively.

$$t_D = (CR - 1)T \quad (3.41)$$

$$t_S = (2 - CR)T \quad (3.42)$$

where T is mesh period, and t_D and t_S represent the time intervals of double and single pair, respectively.

In Figs (3.15)-(3.17), mesh stiffness and the effect of addendum modification factors can be seen.

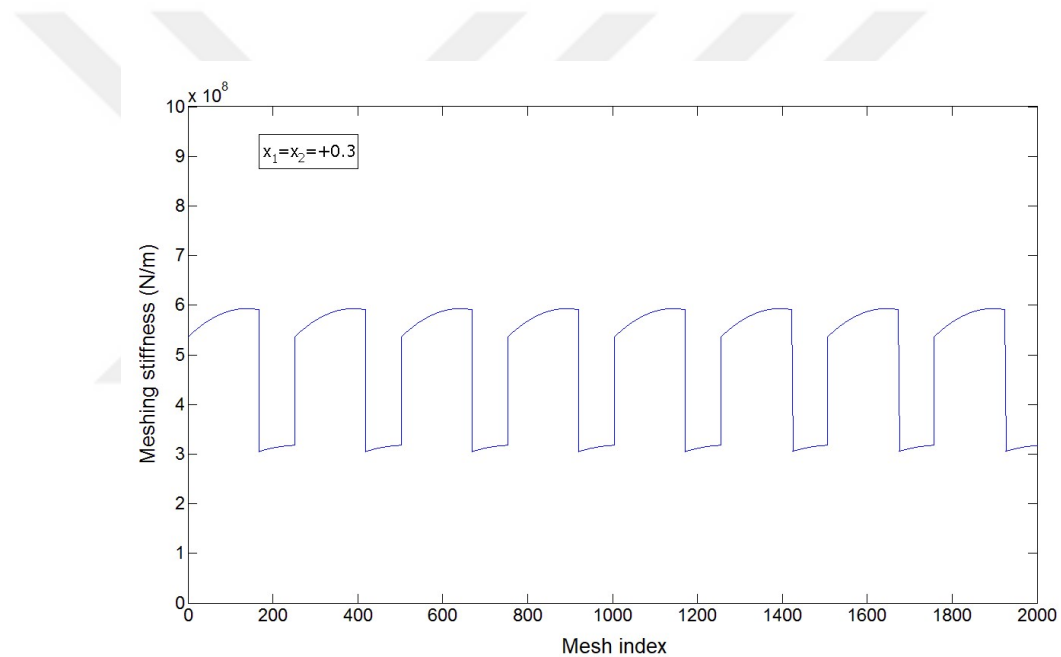


Figure 3.15 Mesh stiffness for positive modification coefficient

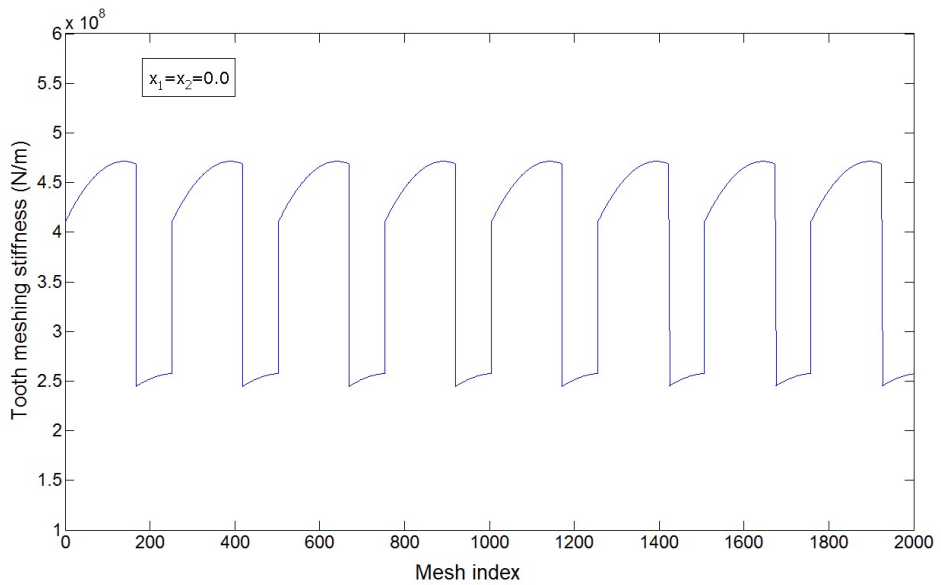


Figure 3.16 Mesh stiffness without modification

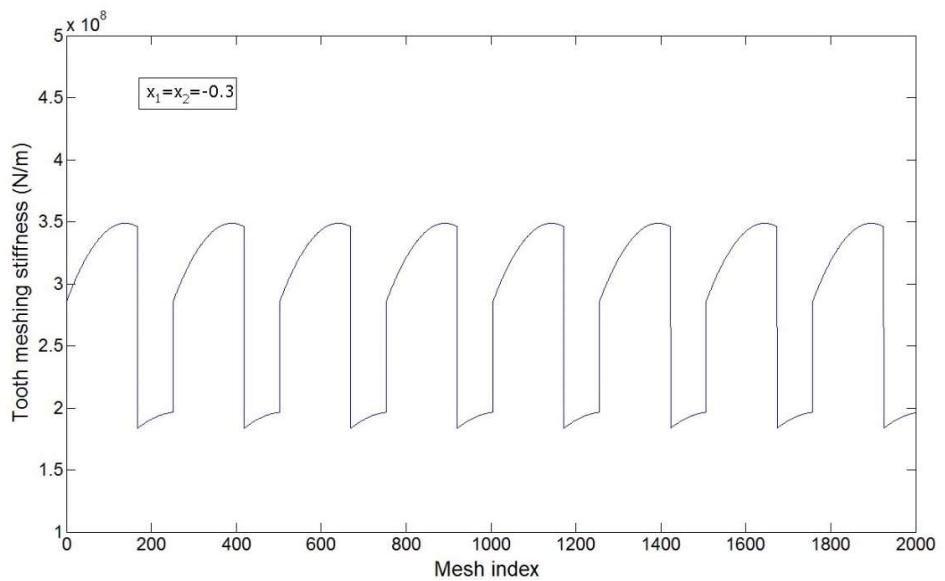


Figure 3.17 Mesh stiffness with negative modification coefficient

The next subsection, presents the modeling of faults and inclusion of their effects in the dynamic model. The faults which are considered here, include tooth surface pitting and tooth root crack. The effect of surface pitting is added to mesh force and the effect of crack, modifies the mesh stiffness.

3.2.1.3 Modeling tooth surface pitting

It has been mentioned in reference [55] that the severity and extent of a fault can be best modeled by using pulses. The pulse height has an important effect on the amplitude and it changes with the severity of fault and can increase with the fault growth.

In practice, the response of a system can be modelled well with the use of a decaying sinusoidal pulse as shown in Fig 3.18. It can be shown by the following equation [55]:

$$x(t) = \left(\frac{k}{\sqrt{1-\zeta^2}} \right) e^{-\zeta\omega_0 t} \sin \left\{ \sqrt{1-\zeta^2} \omega_0 t + \sin^{-1}(2\zeta\sqrt{1-\zeta^2}) \right\} \quad (3.43)$$

where $K = \frac{k}{\sqrt{1-\zeta^2}}$ and k is the height of the pulse. ζ denotes the damping ratio, $\omega_0 = \frac{\pi}{\Delta t}$ is the frequency of the generated pulse, $\Delta t = \frac{b}{v_a}$ is the pulse width, b shows the fault width along the tooth profile and v_a represents the relative velocity at the defected point. The relative velocity is the difference between the velocities of the two gears at contact point.

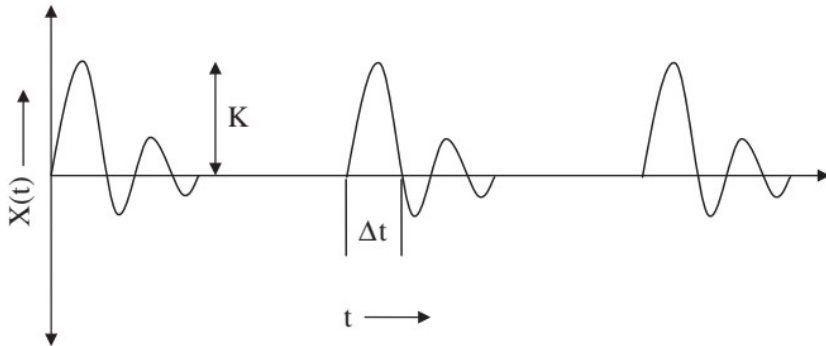


Figure 3.18 Periodic decaying sinusoidal pulse [55]

The gear mesh force without the effect of faults, F_0 , can be written as follows

$$F_0 = k_m(R_1\theta_1 - R_2\theta_2 + y_2 - y_1) + c_m(R_1\dot{\theta}_1 - R_2\dot{\theta}_2 + \dot{y}_2 - \dot{y}_1) \quad (3.44)$$

where k_m and c_m are time varying mesh stiffness and mesh damping, respectively.

After including the effect of pitting, it is modified as given in equation (3.45)

$$F = F_0 + k_h f x(t) \quad (3.45)$$

Where f denotes the defect width in the tooth face direction. Therefore, by using the modified mesh force F , the effect of pitting can be included in the model.

3.2.1.4 Modeling tooth root crack

In order to model the tooth root crack, an approximate model which is a beam with a crack as shown in Fig 3.19, is used. The beam has a crack with depth a at a distance l_c from its left end. The cross section of the beam has a width b and height h . This model can be used in lateral vibration analysis, for any beam with any boundary conditions. Since the bending stiffness at the crack location is decreased, at the cross section of crack position, a torsional spring with stiffness K_θ is used (see Fig 3.19). The main underlying theory in this modeling method is that the absorbed energy in crack growth equals the absorbed energy by the torsional spring which replaced the

crack. This theory has been introduced by Chondros [56]. The stiffness coefficient K_θ , which is a function of crack depth, geometrical properties of the beam, and beam material properties, is given by equation (3.46) [56]:

$$K_\theta = \frac{EI}{6(1-\nu^2)h} \times \frac{1}{j(\frac{a}{h})} \quad (3.46)$$

where the function $j()$ is defined as follows [56]:

$$j\left(\frac{a}{h}\right) = 1.8624\left(\frac{a}{h}\right)^2 - 3.95\left(\frac{a}{h}\right)^3 + 16.375\left(\frac{a}{h}\right)^4 - 37.226\left(\frac{a}{h}\right)^5 + 76.81\left(\frac{a}{h}\right)^6 - 126.9\left(\frac{a}{h}\right)^7 + 172\left(\frac{a}{h}\right)^8 - 143.97\left(\frac{a}{h}\right)^9 + 66.56\left(\frac{a}{h}\right)^{10} \quad (3.47)$$

Now, the equations for the cracked beam with rectangular cross section is used for modeling crack in gear tooth and by including a rotational spring at the cracked section, the bending stiffness of the cracked tooth is calculated. Dimensions of a spur gear tooth is shown in Fig 3.20 where it can be approximated with a rectangle.

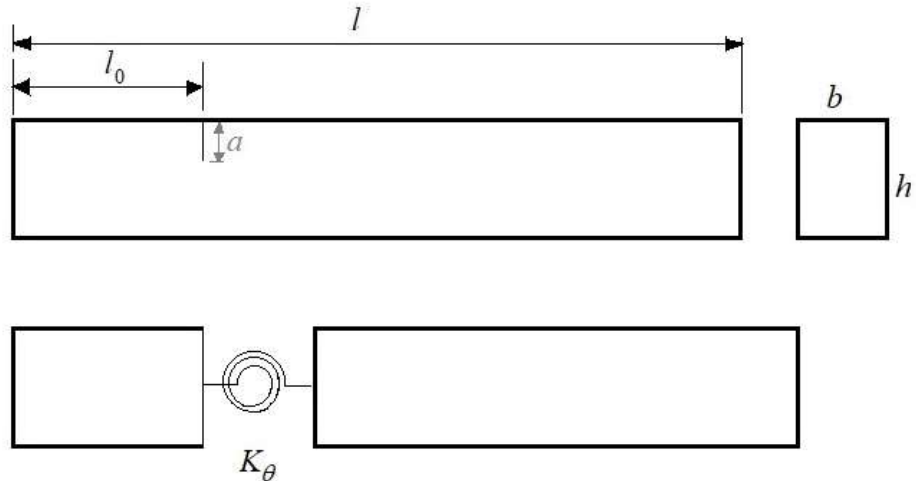


Figure 3.19 Modeling crack in a beam with rectangular cross section

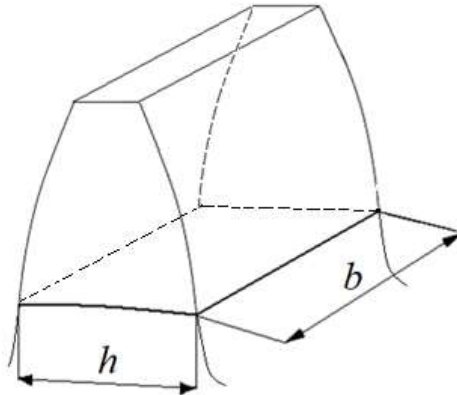


Figure 3.20 Gear tooth profile dimensions

After some manipulation considering Fig 3.21, the governing equation for the bending stiffness of cracked tooth can be written as follows

$$\frac{1}{k_C(r)} = \frac{1}{k_H(r)} + \frac{1}{K_\theta/d^2 \cos \alpha} \quad (3.48)$$

where $k_H(r)$ and $k_C(r)$ represent intact and cracked gear tooth stiffness, respectively and α denotes the pressure angle. The distance d is calculated using the following equation

$$d = r - r_r \quad (3.49)$$

Where, r_r is the root radius of the gear.

After the calculation of cracked tooth stiffness, considering the crack position and the number of cracked tooth, the mesh stiffness is modified and therefore the effect of crack can be included in the equations of motion.

In reference [57], the mesh stiffness of a gear with tooth root crack is calculated using finite element method.

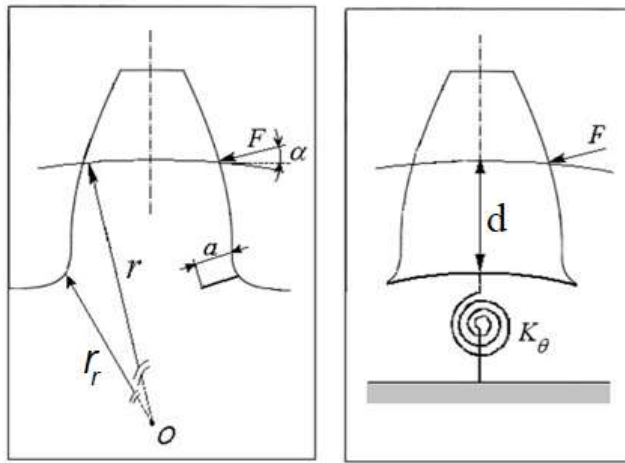


Figure 3.21 Modeling tooth root crack

According to the Fig 3.22, the mesh stiffness is decreased and it is more obvious in the single tooth contact area.

The results of cracked tooth mesh stiffness obtained using the approximate method developed in this study is shown in Fig 3.23. The results are for bending stiffness and it can be converted to torsional stiffness using appropriate coefficients. The error in the calculation of mesh stiffness using approximate method is at most about 8% which is acceptable because in the approximate model, the crack is not skewed.

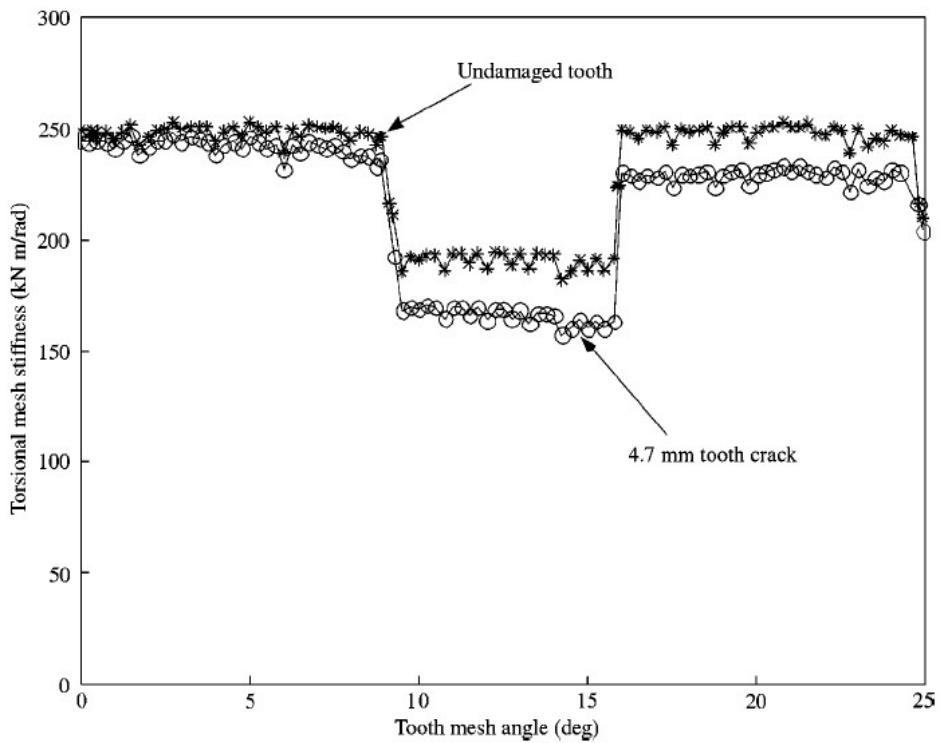


Figure 3.22 Mesh stiffness of gear with cracked tooth calculated by FEM [57]

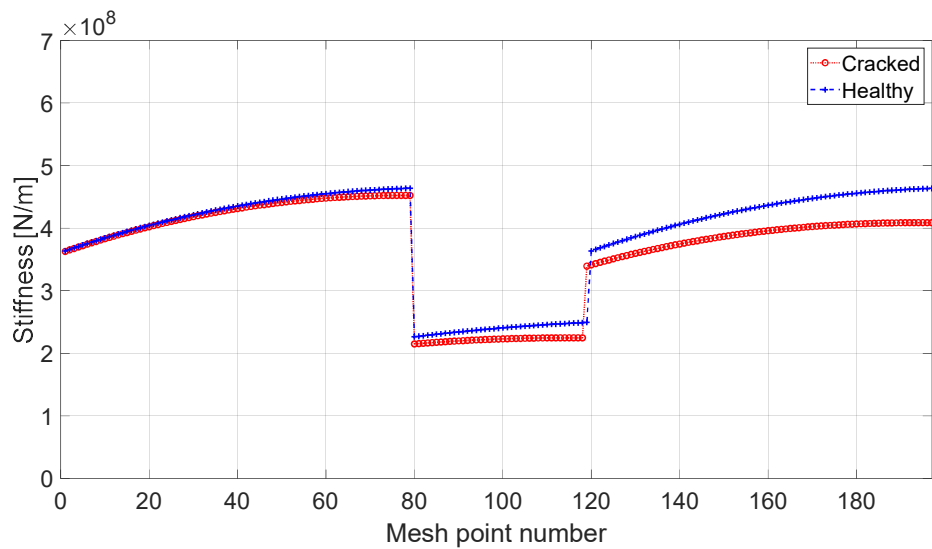


Figure 3.23 Mesh stiffness of cracked tooth calculated using the approximate method

3.2.1.5 Solution of the dynamic equations

Due to the backlash, and the fact that the mesh stiffness and mesh damping are functions of angle of rotation, the obtained equations of motion are non-linear. However, at a constant speed, the mesh stiffness and damping can be considered as functions of time. Therefore, the equations can be approximated with piecewise linear equations which are separated based on the contact condition of the meshing tooth. However, at any circumstance, the equations of motion are non-linear due to backlash.

Based on the value of mesh force, the equations are separated as given in equations (3.50) and (3.51)

For positive contact

$$F > 0 \Rightarrow F = F_0 \quad (3.50)$$

For tooth separation or backside collision

$$F \leq 0 \Rightarrow F = \begin{cases} F_0 + k_m b, & TE \geq b \\ 0, & -b < TE < b \end{cases} \quad (3.51)$$

where b is backlash and TE is dynamic transmission error which is the difference between the pinion and gear tangential displacement at pitch radius.

For the initial values of the variables, the static displacements due to input torque while the load DOF is fixed, are used.

The equations are solved using Runge-Kutta method and the dynamic response is obtained.

3.2.1.6 Simulation results

For the verification of the dynamic model, the parameter values given by Parey et al [1] are used which are presented in Table 3.3.

The obtained results for the case of intact gears set, are shown in Figs (3.24)-(3.28). Acceleration of bearings are important in the sense that in practical gear fault detection, the vibration signals are mostly collected with mounting sensors on top of the bearings.

Table 3.3 Gear system data [1]

Parameter	Pinion	Gear
Speed (rpm)	1000	952
Number of teeth	20	21
Face width (m)	0.015	0.03
Shaft diameter (m)	0.092	0.110
Module (m)	0.01	0.01
Pressure angle	20°	20°
Addendum coefficient	1.0	1.0
Dedendum coefficient	1.4	1.4
Mass (N)	36	80
Shaft torsional stiffness (N m/rad)	1917	3383
Bearing stiffness (N/m)	10^8	10^9
Shaft viscous damping coefficient (N s/rad)	0.268881	0.357188
Bearing viscous damping coefficient (N s/m)	8740.15	8740.15
Drive torque (N m)	200	

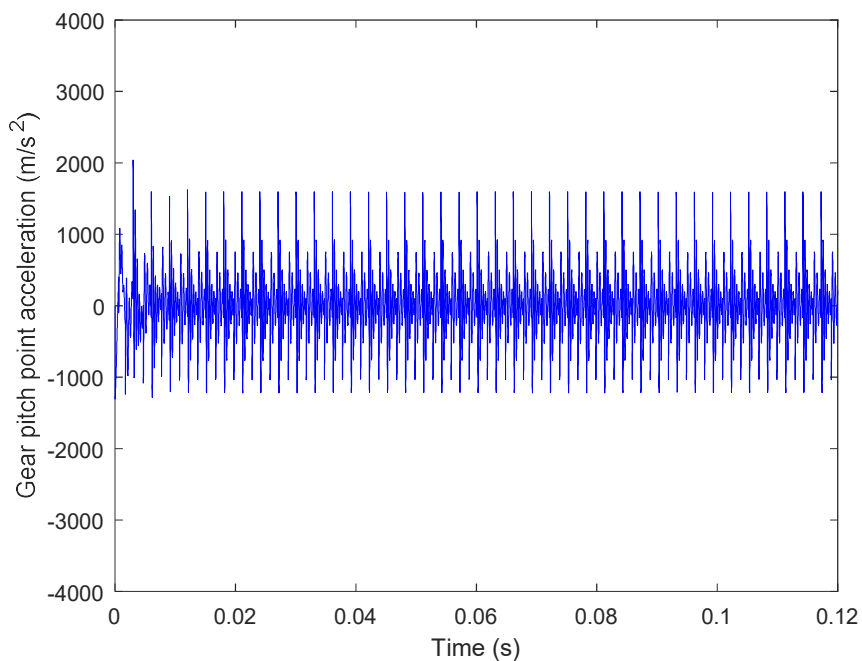


Figure 3.24 Tangential acceleration at pitch point, gear

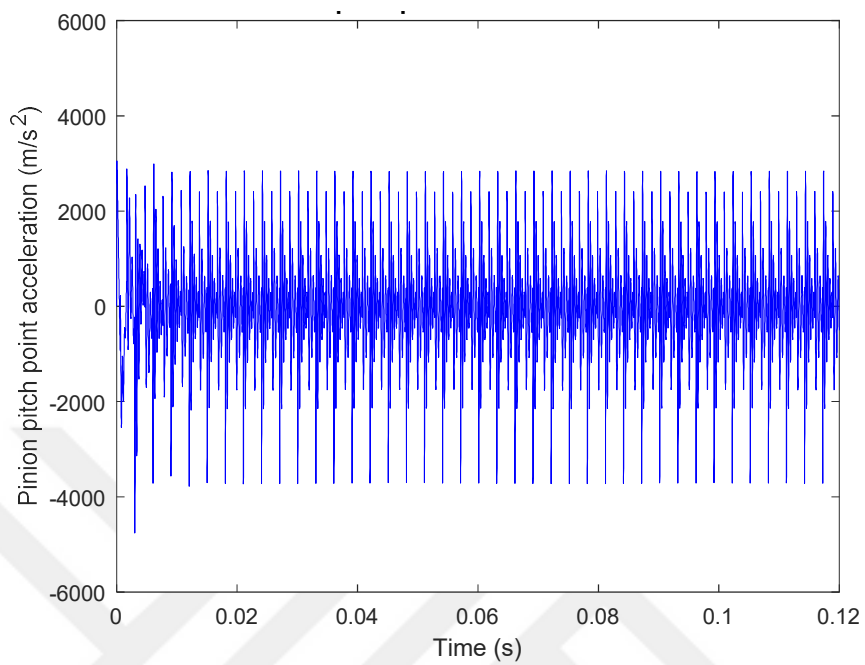


Figure 3.25 Tangential acceleration at pitch point, pinion

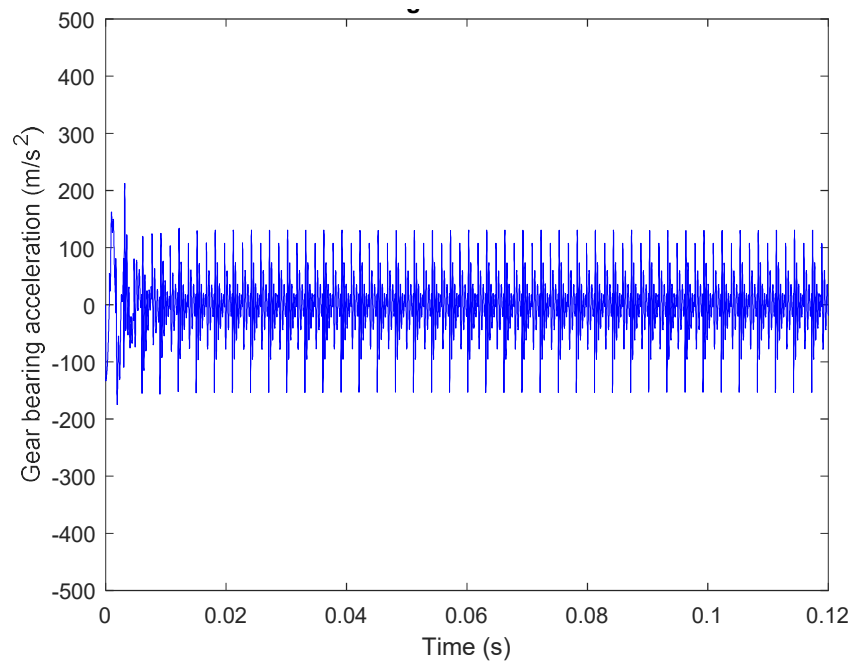


Figure 3.26 Gear bearing acceleration

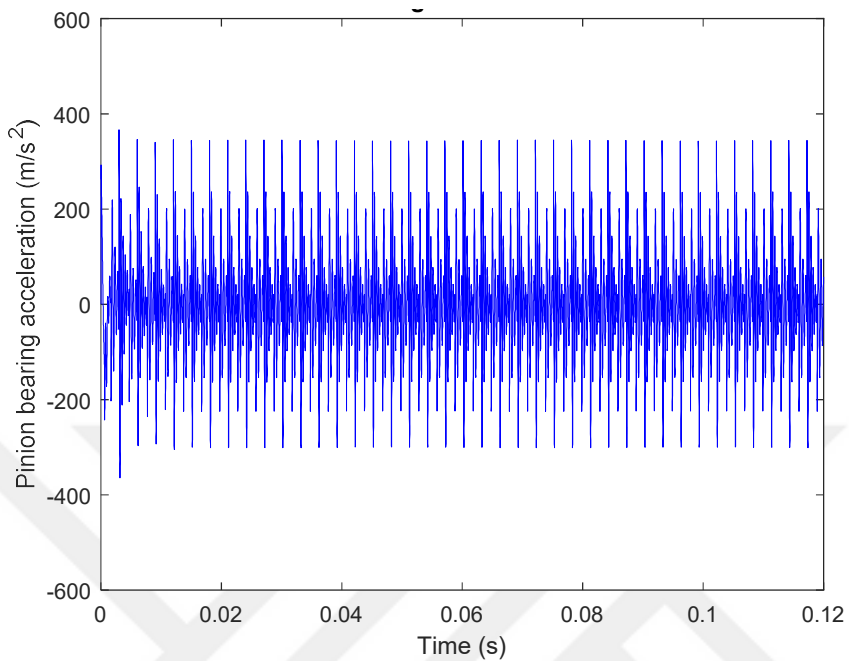


Figure 3.27 Pinion bearing acceleration

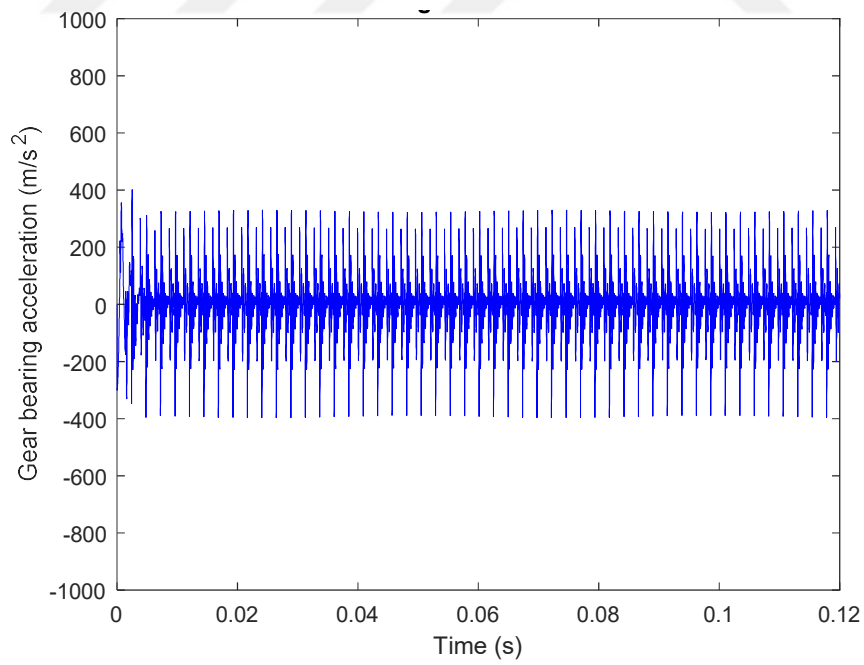


Figure 3.28 Gear bearing acceleration

In the following figures, the results of the dynamic model are compared with those given in reference [1]. By comparing the pinion bearing acceleration for the healthy case (see Figs 3.29 and 3.30), and pinion bearing acceleration for the pitted tooth case, it can be said that the results compare well both qualitatively and quantitatively. Therefore, the model is verified and it the fault modeling method can be used later in other gearbox types, which will be a planetary gearbox in our case.

In this section, a non-linear model for a six-DOF spur gear pair was obtained and verified. The procedure of modeling time varying gear mesh stiffness for the healthy and cracked case which plays an important role in the vibrations of gear systems, was given. The dynamic model and the fault modeling method was verified using the results given in the literature. Therefore, the modeling procedure can be used for the planetary gears as well. As one may know, constituent components of planetary gearboxes are mostly spur gears. As a result, the process of modeling mesh stiffness and faults are readily available for the planetary gearbox. This was carried out first, due to the fact that modeling faults and mesh stiffness directly for the planetary gears has its own complexity and cannot be handled easily.

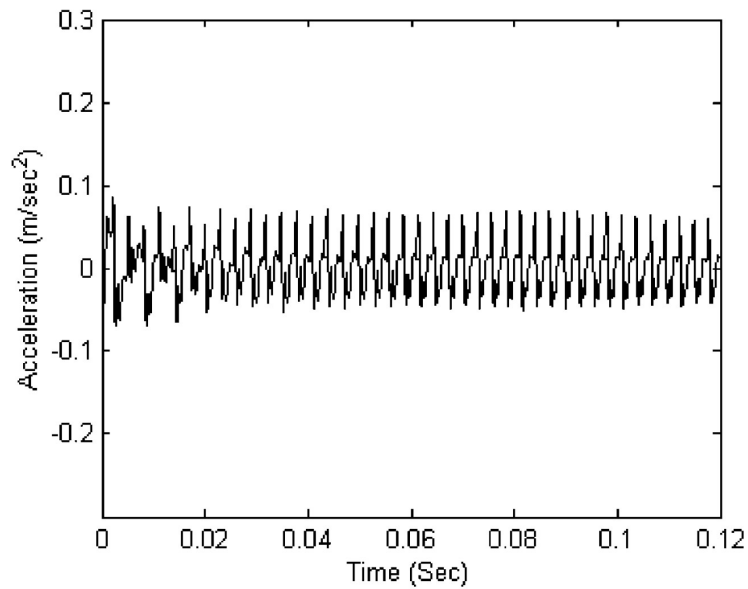


Figure 3.29 Pinion bearing acceleration [1]

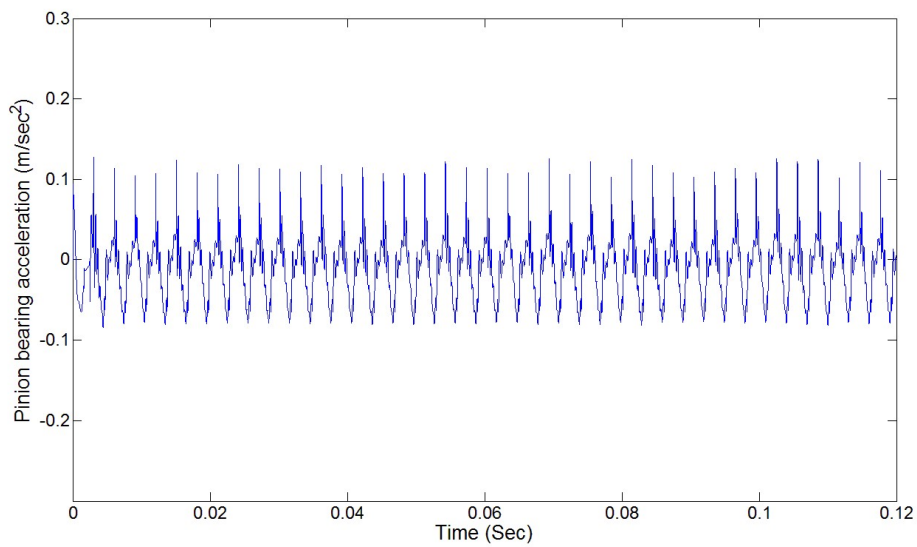


Figure 3.30 Calculated pinion bearing acceleration, intact gears

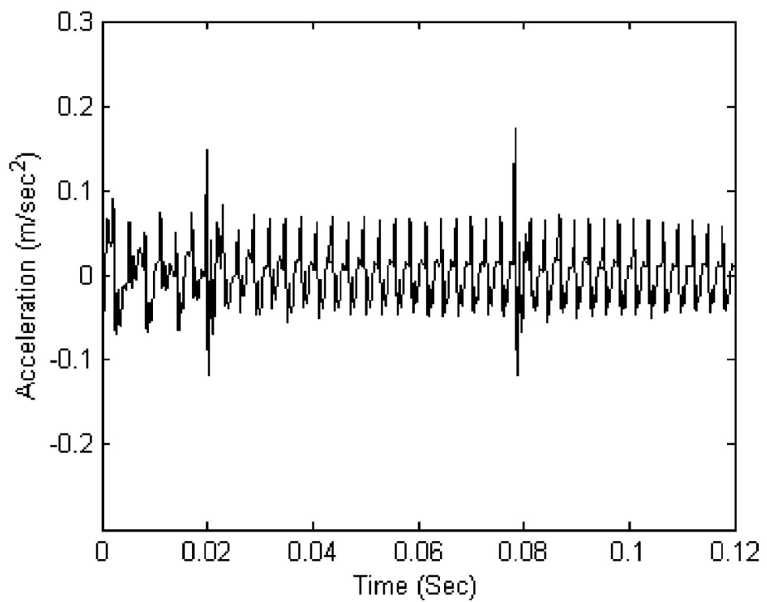


Figure 3.31 Pinion bearing acceleration, pitted tooth [1]

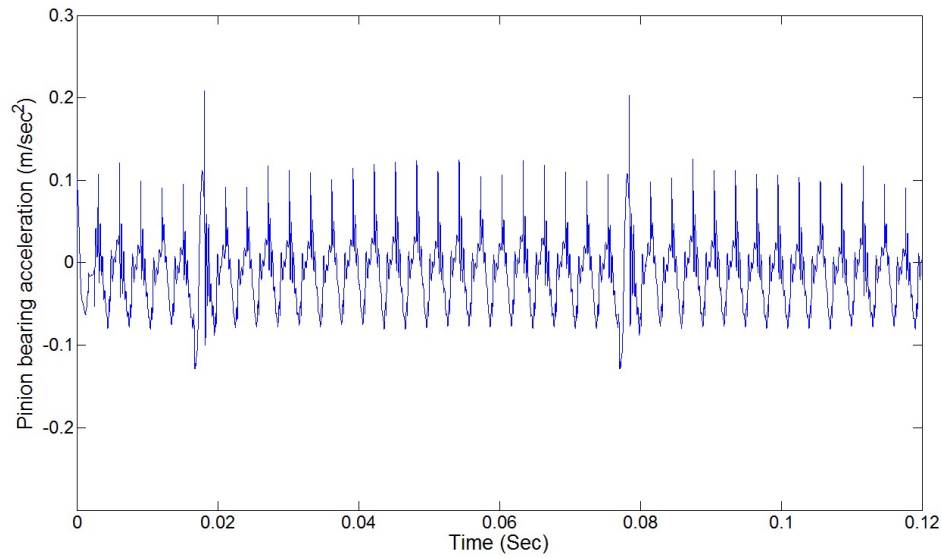


Figure 3.32 Calculated pinion bearing acceleration, pitted tooth

Once it is focused on the response in a shorter time interval, the behavior can be visualized in a better way. In Fig 3.33, tooth mesh dynamic load is shown, as it can be noticed, once the defected tooth is in mesh, due to the impulsive nature of the pitting, the mesh force changes drastically. This effect is visible in pinion and gear bearing accelerations (see Figs 3.34-3.35) as well as the pitch point accelerations (see Figs 3.36-3.37).

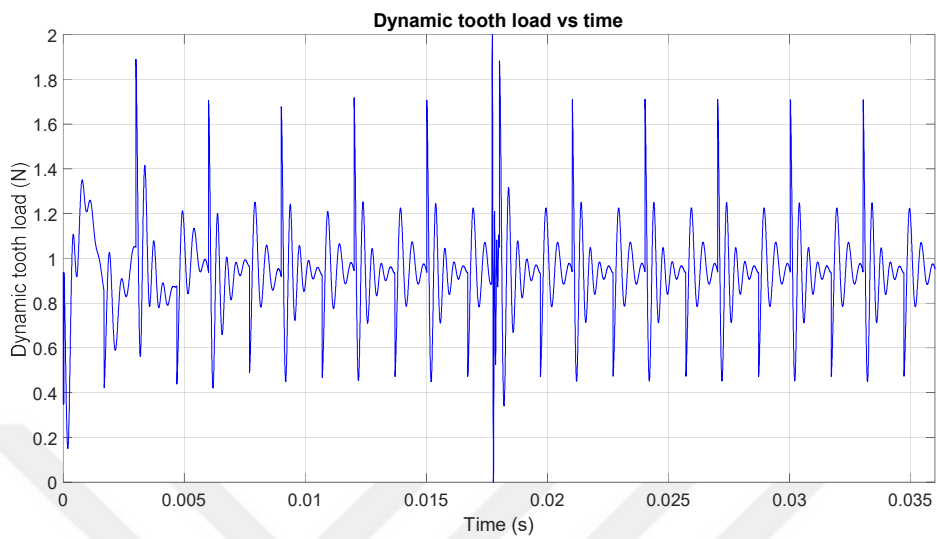


Figure 3.33 Dynamic tooth load, including pinion pitting

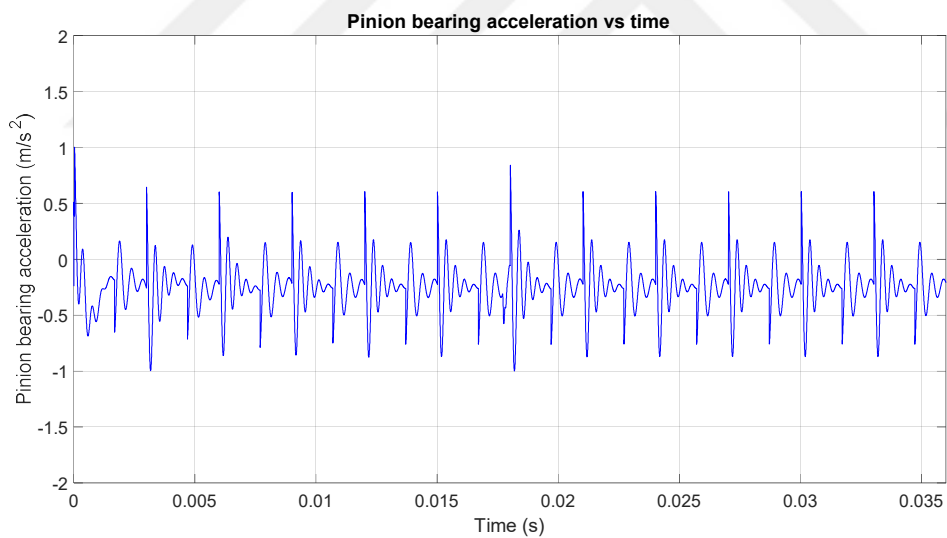


Figure 3.34 Pinion bearing acceleration, including pinion pitting

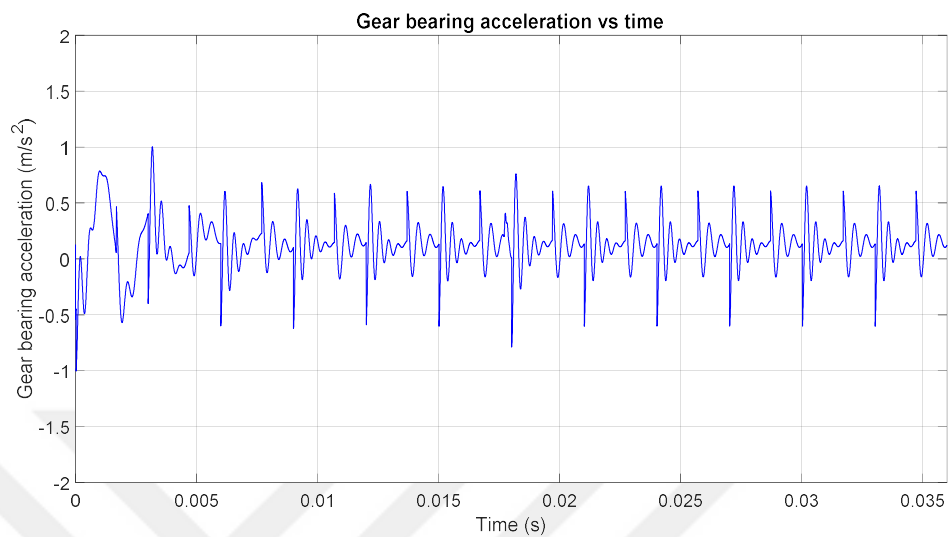


Figure 3.35 Gear bearing acceleration, including pinion pitting

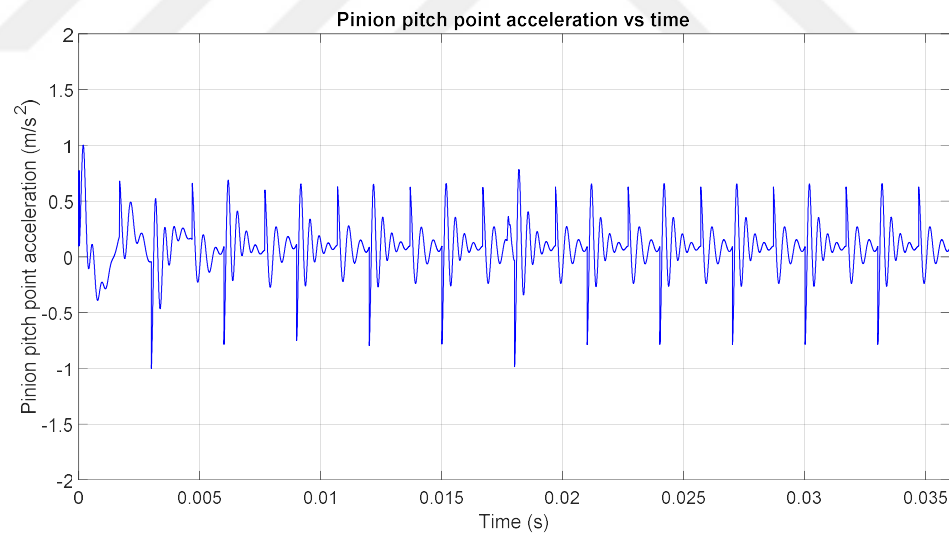


Figure 3.36 Pinion pitch point acceleration, including pinion pitting

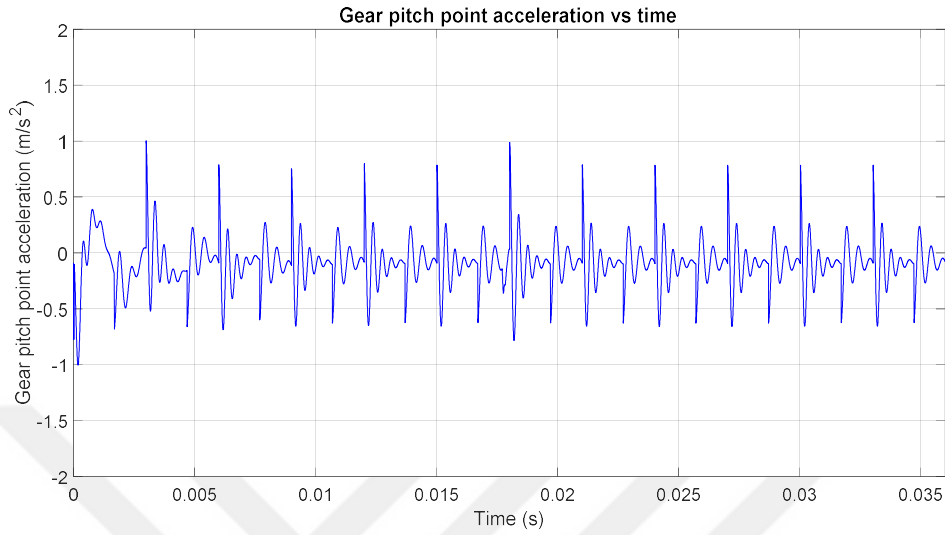


Figure 3.37 Gear pitch point acceleration, including pinion pitting

In order to investigate the effect of fault in a practical way, FFT of the response is calculated. In Fig 3.38, the FFT of the pinion bearing acceleration for the case of pitted tooth is shown. As it can be seen, the amplitude of acceleration at harmonics of mesh frequency increases. This is due to the impulsive behavior or pitting which is localized in time and therefore, distributed in frequency domain.

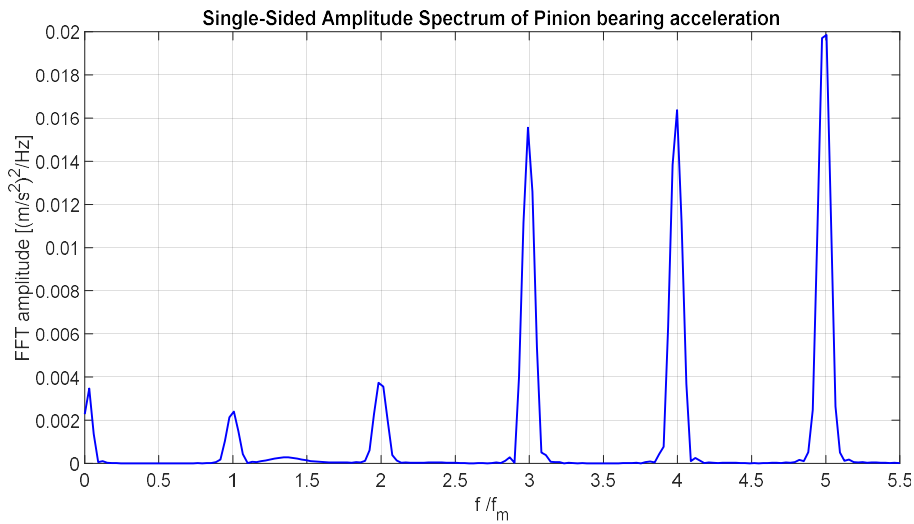


Figure 3.38 FFT of the pinion bearing acceleration with pitted pinion tooth

3.2.2 Non-linear dynamic response of a purely rotational planetary gear system with sun gear fault

This section, presents the dynamic modeling of a planetary gearbox with the sun gear fault and analysis of fault symptoms in the frequency domain by FFT method. It is in fact the same model used in the section 3.1 with the transverse DOFs constrained. To achieve the target of the section, the following subjects are discussed in advance:

- I. The procedure of including damping in the model
- II. Calculation and inclusion of gear mesh phasing between different gear pairs
- III. The process of including sun gear fault considering faulty tooth mesh period
- IV. Time integration algorithm by Generalized- α method

3.2.2.1 Modeling damping

To include damping in dynamic model, a proportionally distributed damping is calculated and added to the equations of motion. Usually, a proportional damping $[C]$ is considered as [58, pp 63-64]

$$[C] = \beta[K] + \gamma[M] \quad (3.52)$$

where $[C]$, $[K]$ and $[M]$ are damping, stiffness and mass matrices respectively. β and γ are proportionality constants. In such a case, the damped natural frequencies, damping ratios and mode shapes of the damped system will have the following forms [58, pp 63-64]:

$$\omega'_r = \bar{\omega}_r \sqrt{1 - \zeta_r^2}; \zeta_r = \beta \bar{\omega}_r / 2 + \gamma / 2 \bar{\omega}_r$$

and

$$[\Psi_{damped}] = [\Psi_{undamped}] \quad (3.53)$$

where $\bar{\omega}_r$ and ω'_r represent undamped and damped natural frequencies, and ζ_r is modal damping ratio. Ψ stands for mode matrix.

As the mesh stiffness, i.e. the elements of stiffness matrix are a function of gear flexibility and it is related with internal material or hysteresis damping, referencing [58], only β is nonzero and the damping is set proportional to stiffness only.

3.2.2.2 Calculation of gear mesh phasing

The gear mesh stiffness varies with time as an influence of alternating number of teeth in contact. In the dynamic modeling and analysis of gears, the correct relative of different gear meshes must be taken into account. In a planetary gearbox, multiple planets mesh with sun gear and ring gear and the relative phasing between different pairs should be calculated and considered in the mesh stiffness functions.

Here, $k_{sn}(t)$, $k_{rn}(t)$ denote the mesh stiffness functions of the n-th planet with sun and ring gears, respectively. They are time dependent and vary with time during the mesh period. Sun-planet mesh stiffness functions has the same shape for all planet-sun meshes but they are not in phase with each other. It holds for planet-ring meshes as well.

Fig 3.39 shows a purely rotational dynamic model of a planetary gear generally used in dynamic analyses. The phasing between different meshes as shown in Fig 3.40, are γ_{sn} which is relative phase between n-th planet-sun gear and arbitrarily chosen first planet-sun mesh, γ_{rn} that denotes phase between n-th planet-ring and first planet-ring mesh, and $\gamma_{rs}^{(n)}$ that represents relative mesh phase between n-th planet-ring and n-th planet-sun mesh. It is shown as well that, $\gamma_{rs}^{(n)}$ is independent of the planet chosen. Although the relations of phasing γ_{sn} , γ_{rn} and $\gamma_{rs}^{(n)}$ are referenced to the contact on pitch point of planet-sun and planet-ring meshes, they can be measured with respect to any point within the mesh period of a given gear pair. The phasing are given as a fraction of the gear mesh period T_m . Here, only the decimal part of the fraction of γ_{sn} , γ_{rn} and $\gamma_{rs}^{(n)}$ is retained. The range of the phases is as $-1 < \gamma_{sn}, \gamma_{rn}, \gamma_{rs}^{(n)} < 1$, although it can be confined to $0 \leq \gamma_{sn}, \gamma_{rn}, \gamma_{rs}^{(n)} < 1$.

The governing relationships of mesh phasing, depend on the direction of the planet rotation which actually depends on which gear is considered to be fixed and which ones is the input and what is its direction of rotation. Based on different arrangements, multiple possible configurations are listed in Table 3.4.

The equations of the mesh phasing are given as follows [59]:

For clockwise rotation of planet

$$\gamma_{sn} = \frac{Z_s \psi_n}{2\pi}, \gamma_{rn} = -\frac{Z_r \psi_n}{2\pi} \quad (3.54)$$

For counterclockwise rotation of planet

$$\gamma_{sn} = -\frac{Z_s \psi_n}{2\pi}, \gamma_{rn} = \frac{Z_r \psi_n}{2\pi} \quad (3.55)$$

where Z_s and Z_r represent the tooth number of sun and planet respectively, and ψ_n is the circumferential phase difference between the planets (see Fig 3.39) which is positive when measured counterclockwise. For instance, for the first planet, $\psi_1 = 0$. In the equations (3.54) -(3.55), the sign is important as it shows phase lead for negative and phase lag for positive sign. The phase ψ_n , is in fact the relative phase difference between two arbitrarily chosen planetary gears. Such that for planet i and planet j , it can be written as $\psi_n = \psi_i - \psi_j$. The equations given in (3.54) and (3.55) are for relative phasing of planet-sun and planet-ring mesh, individually. It is required to define phasing between sun-planet and planet-ring mesh for the same planet, $\gamma_{rs}^{(n)}$. It can vary between -1 and +1, and it changes based on odd or even number of teeth for the planet.

Another phasing which is defined for meshing between different sun-planet and planet-ring mesh, is $\hat{\gamma}_{rn}$. It is defined as the phase between n-th planet and ring mesh with first planet and sun mesh. The $\gamma_{rs}^{(n)}$ can be obtained using the following equation [59]

$$\gamma_{rs}^{(n)} = \hat{\gamma}_{rn} - \gamma_{sn} = (\gamma_{rn} + \gamma_{rs}^{(1)}) - \gamma_{sn} = \left(-\frac{Z_r \psi_n}{2\pi} + \gamma_{rs}^{(1)}\right) - \frac{Z_s \psi_n}{2\pi} = \gamma_{rs}^{(1)} - (Z_s + Z_r) \frac{\psi_n}{2\pi} \quad (3.56)$$

where $\hat{\gamma}_{rn}$ is the phase difference between n -th planet and ring mesh with first planet and sun mesh (at an arbitrary reference point, e.g., pitch point) and $\gamma_{rs}^{(1)}$ represents phase difference between the planet-sun and planet-ring mesh for the first planet gear.

In a planetary gearbox, the circumferential location of each of planets (ψ_n) must be an integer multiple of the least mesh angle, such that [59]

$$\psi_n = p_n \frac{2\pi}{Z_s + Z_r} \quad (3.57)$$

where p_n is an integer which depends on the selected planet.

It can be shown that relative phase between the sun-planet and ring-planet is the same for all planets. The mesh phase difference of n -th planet and ring and first planet and sun (referenced to pitch point) can be calculated as [59]

$$\hat{\gamma}_{rn} = \gamma_{rs} + \gamma_{rn} = \gamma_{sn} + \gamma_{rs} \quad (3.58)$$

The first equation represents the phase between planet 1 and sun mesh and planet 1 and ring mesh, plus the phase difference between n -th planet and ring mesh with planet 1 and planet 1 and ring mesh. the second equation shows the phase difference between planet n and sun mesh and planet 1 and sun mesh plus planet n and ring mesh and planet n and sun mesh.

The equation (3.58) is a very important equation that helps determination of relative phase relationships. Assuming that the relative phasing of planet-sun meshes is obtained, the next task is to determine the relative phasing of ring-planet meshes with respect to sun-planet meshes. For the first sun-planet and planet-ring gear, it is trivial and only the term γ_{rs} is included in the stiffness term. However, when it comes to ring-planet mesh for planets other than the first, the relative phasing of ring-planet mesh to the first planet and ring mesh, i.e., γ_{rn} must be added and this results in $\hat{\gamma}_{rn}$.

From equation (3.58) it can be deduced that $\gamma_{rn} = \gamma_{sn}$.

Having defined the mesh phase relationships, the mesh stiffness variation function will be governed by [59]

$$k_{sn}(t) = k_{s1}(t - \gamma_{sn} T_m) \quad (3.59)$$

where T_m is the period of stiffness variation for all planet-sun meshes. $t = 0$ can be referenced to contact at pitch point for planet 1 and sun mesh. k_{sn} and k_{s1} can be approximated by Fourier series as follows [59]

$$k_{s1}(t) = \sum_{n=0}^{\infty} [a_n \sin n\omega_m t + b_n \cos n\omega_m t]$$

$$k_{sn}(t) = \sum_{n=0}^{\infty} [a_n \sin n\omega_m (t - \gamma_{sn} T_m) + b_n \cos n\omega_m (t - \gamma_{sn} T_m)] \quad (3.60)$$

Similar equations can be written for planet-ring meshes. The only difference is that, γ_{rs} must be included as phasing. The Fourier series forms of the ring-planet stiffness can be written as

$$\begin{aligned} \kappa_{r1}(t) &= \sum_{n=0}^{\infty} [c_n \sin n\omega_m t + d_n \cos n\omega_m t] \\ k_{r1}(t) &= \sum_{n=0}^{\infty} [c_n \sin n\omega_m (t - \gamma_{rs} T_m) + d_n \cos n\omega_m (t - \gamma_{rs} T_m)] \\ k_{rn}(t) &= \sum_{n=0}^{\infty} [c_n \sin n\omega_m (t - \hat{\gamma}_{rn} T_m) + d_n \cos n\omega_m (t - \hat{\gamma}_{rn} T_m)] \end{aligned} \quad (3.61)$$

The results given here is valid for spur and helical gears with modified or unmodified teeth.

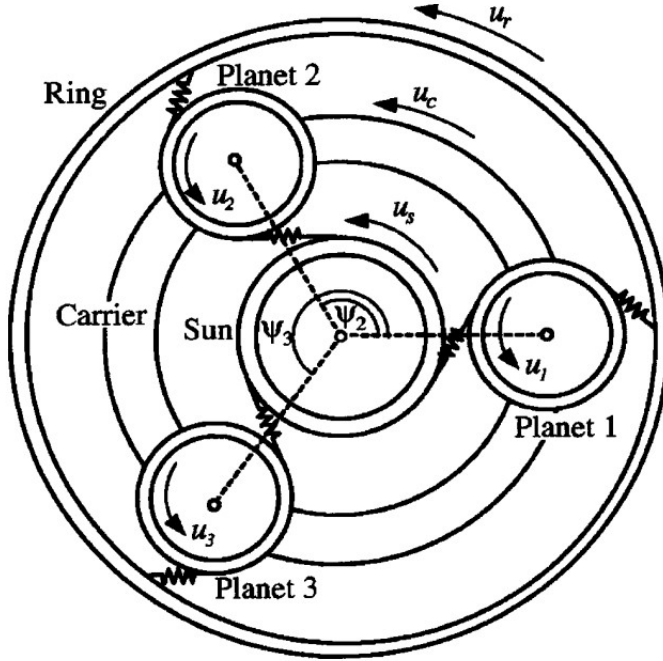


Figure 3.39 Schematic of a planetary gearbox. $u_s, u_c, u_r, u_{1,2,3}$ represent degrees of freedom of the model [59]

Table 3.4 Possible configurations at line of action based on fixed element, input element, and the direction of rotation for input.

a) direction of rotation of planet gear and b) mesh direction on the line of action. The points B_1, E_1, B_2, E_2 are shown in Fig 3(b). CCW and CW stand for counterclockwise and clockwise [59]

Fixed Element	Input	Input Rotation	Planet Rotation	Contact Progression on Line of Action (see Figure 3b)	
				Sun-Planet Mesh	Ring-Planet Mesh
Ring	Sun	CW	CCW	$B_1 \rightarrow E_1$	$B_2 \rightarrow E_2$
	Sun	CCW	CW	$B_1 \rightarrow E_1$	$B_2 \rightarrow E_2$
	Carrier	CW	CCW	$E_1 \rightarrow B_1$	$E_2 \rightarrow B_2$
	Carrier	CCW	CW	$E_1 \rightarrow B_1$	$E_2 \rightarrow B_2$
Sun	Carrier	CW	CW	$B_1 \rightarrow E_1$	$B_2 \rightarrow E_2$
	Carrier	CCW	CCW	$B_1 \rightarrow E_1$	$B_2 \rightarrow E_2$
	Ring	CW	CW	$E_1 \rightarrow B_1$	$E_2 \rightarrow B_2$
	Ring	CCW	CCW	$E_1 \rightarrow B_1$	$E_2 \rightarrow B_2$
Carrier	Sun	CW	CCW	$B_1 \rightarrow E_1$	$B_2 \rightarrow E_2$
	Sun	CCW	CW	$B_1 \rightarrow E_1$	$B_2 \rightarrow E_2$
	Ring	CW	CW	$E_1 \rightarrow B_1$	$E_2 \rightarrow B_2$
	Ring	CCW	CCW	$E_1 \rightarrow B_1$	$E_2 \rightarrow B_2$

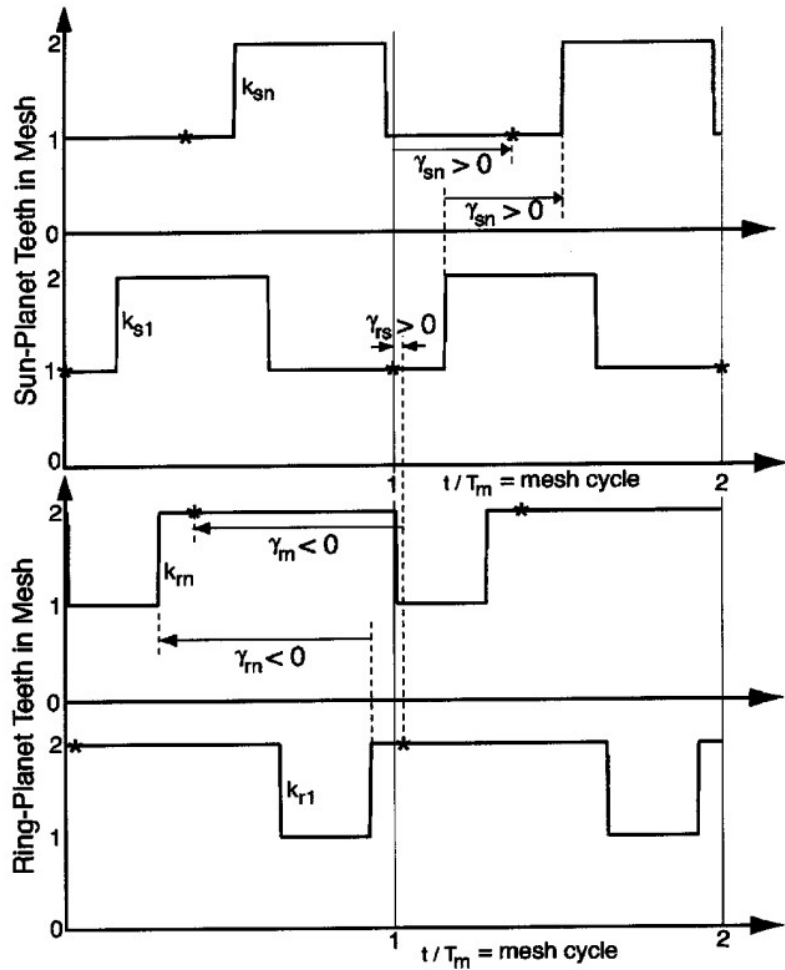


Figure 3.40 Mesh phases of a planetary gearbox shown on the periodic mesh stiffness $\gamma_{sn}, \gamma_m, \gamma_{rs}, \gamma_{s1} = 0$, and $t=0$ corresponds to pitch point contact at first plant and sun mesh. The symbol * refers to starting point of contact a pitch point [59]

3.2.2.3 Analytical calculation of k_{sn} , k_m and γ_{rs}

Here, p denotes pitch point (b) Mesh progression of sun-planet and planet-ring mesh on the line of action and base circle of gears. R_{sb}, R_{pb}, R_{rb} represent base radii of sun, planet and ring gears, respectively. R_{so}, R_{po} are tip radii of sun, planet, respectively.

R_{ro} denotes root radius of ring gear. The points B, C, P, D and E are related to the points shown in part (a), i.e. periodic mesh stiffness [59]

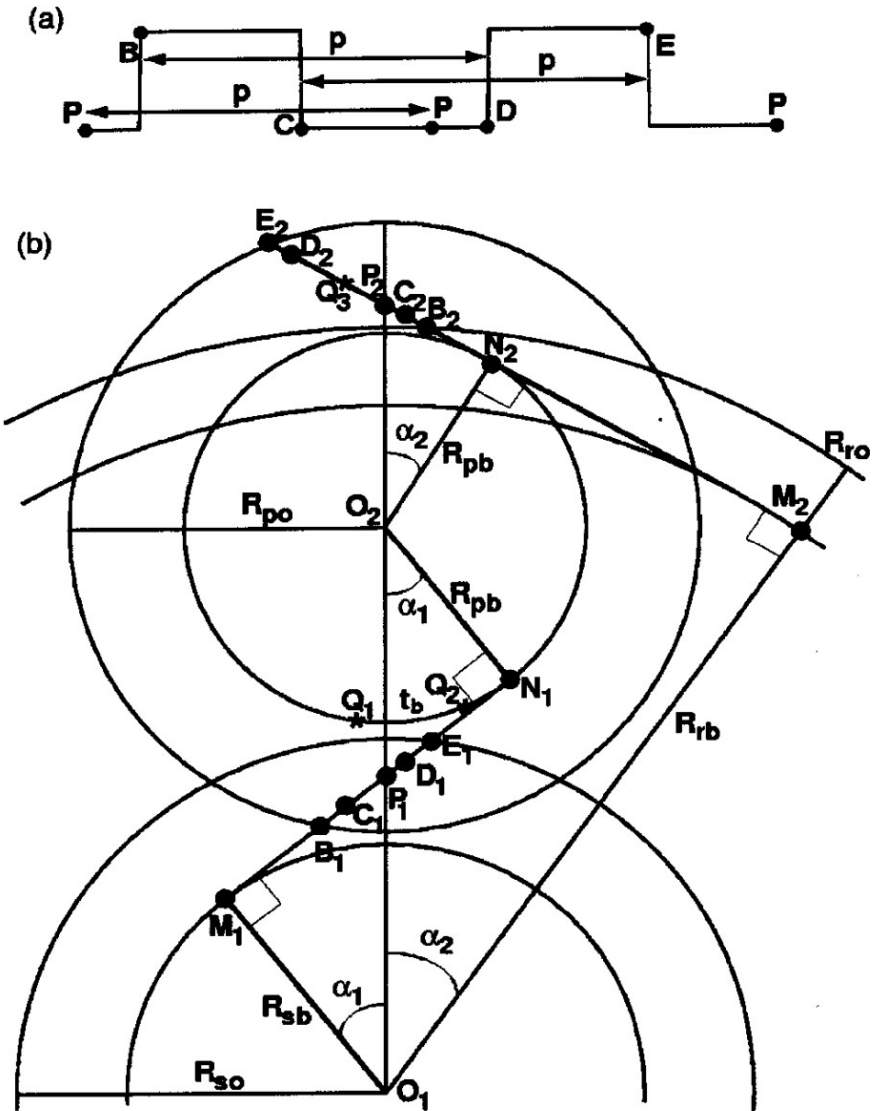


Figure 3.41 (a) Schematic of contact points progression on periodic mesh stiffness [59]

Here for unmodified, involute spur gears the mesh phasing relationships are obtained considering the contact points shown in Fig 3.41. In this figure, the contact points are B, point where second tooth starts meshing; C, point where the first tooth leaves the mesh; P where second tooth contacts at pitch point; D point at which third tooth enters mesh; and finally at point E, third second tooth exits contact. To find the phasing, it is only required to calculate the lengths BE, BC, BP and BD as shown in Fig 3.41(a). The calculations is done based on contact points shown in Fig 3.41(b).

The equation for planet-sun mesh can be written as

$$B_1E_1 = M_1E_1 + B_1N_1 - M_1N_1 = \sqrt{R_{so}^2 - R_{sb}^2} + \sqrt{R_{po}^2 - R_{pb}^2} - (R_{sb} + R_{pb})\tan \alpha_1 \quad (3.62)$$

where α_1 is the pressure angle of sun gear, R_{sb} and R_{so} denote base and tip radius of the sun gear respectively. R_{pb} and R_{po} denote base and tip radius of the planetary gear respectively.

For B_1P_1 , it can be written

$$B_1P_1 = M_1P_1 + M_1B_1 = R_{sb}\tan \alpha_1 - \left(\sqrt{R_{so}^2 - R_{sb}^2} - B_1E_1 \right) \quad (3.63)$$

The base pitch which is the same for all gears, is $p = 2\pi R_{sb}/Z_s = 2\pi R_{pb}/Z_p$, therefore

$$B_1C_1 = B_1E_1 - p, \quad B_1D_1 = p \quad (3.64)$$

In a similar way, the equations for planet-ring mesh can be obtained as follows

$$B_2E_2 = M_2N_2 + N_1E_2 - M_2B_2 = O_1O_2\sin \alpha_2 + \sqrt{R_{po}^2 - R_{pb}^2} - \sqrt{R_{ro}^2 - R_{rb}^2} \quad (3.65)$$

$$B_2P_2 = M_2P_2 - M_2B_2 = R_{rb}\tan \alpha_2 - \sqrt{R_{ro}^2 - R_{rb}^2} \quad (3.66)$$

$$B_2C_2 = B_2E_2 - p, \quad B_2D_2 = p \quad (3.67)$$

where $O_1O_2 = (R_{sb} + R_{pb})/\cos \alpha_1$.

By using the equations (3.62) -(3.67), the mesh phasing γ_{rs} can be obtained which fully defines the mesh stiffness functions $k_{s1}(t)$ and $\kappa_{r1}(\tau)$. Where $t = 0$ and $\tau = 0$ corresponds to mesh at pitch point of $k_{s1}(t)$ and $\kappa_{r1}(\tau)$, respectively. To define k_{sn} , the equations (3.54) -(3.55) and (3.59) are sufficient, while for k_{rn} , it is required to determine γ_{rs} considering the points $Q_{1,2,3}$ based on Fig 3.41(b). These points are actually the locations of pitch point of planet-ring mesh with respect to the pitch point of planet-sun mesh. If the line of contact is wrapped on planet base circle, P_1 will be mapped on Q_1 . The mesh of planet-ring occurs at the opposite face of the mating teeth compared with planet-sun mesh. Here, point Q_2 is used whose distance from Q_1 is t_b where t_b denotes planet tooth thickness at base circle. To find out about phase difference between sun-planet and planet-ring mesh, the first contact point of ring-planet, when the sun-planet mesh at pitch point, B_2E_2 is calculated. It is at a distance of integer multiples of base pitch. This point is Q_3 and to find it, the following length is calculated

$$Q_2B_2 = P_1P_2 - B_2P_2 - t_b = [R_{pb}\tan \alpha_1 + R_{pb}(\pi - \alpha_1 - \alpha_2) + R_{pb}\tan \alpha_2] - B_2P_2 - t_b \quad (3.68)$$

The distance of Q_3 from B_2 measured on B_2P_2 is estimated as

$$B_2Q_3 = p - p[dec(Q_2B_2/p)] \quad (3.69)$$

where $dec()$, shows decimal portion. Therefore, $P_2Q_3 = |B_2Q_3 - B_2P_2|$. For the sun-planet mesh at pitch point, the planet-ring mesh at point Q_3 . Finally, the absolute value of the mesh phase between sun-planet and planet-ring is obtained as

$$|\gamma_{rs}| = (P_2Q_3)/p \quad (3.70)$$

The value of γ_{rs} is independent of direction of rotation and which gear is fixed. Later, the sign of γ_{rs} must be determined, which can be decided based on 1) whether Q_3 is included in B_2P_2 or P_2E_2 , and 2) whether mesh occurs on contact line from B to E or E to B. The mesh direction on line of action is given in Table 3.4.

For the ring-planet mesh occurring from B to E or E to B, $\gamma_{rs} = -|\gamma_{rs}|$ if planet-ring start contact at point Q_3 which is after point P_2 , and $\gamma_{rs} = |\gamma_{rs}|$ (i.e. positive), if Q_3 is located before point P_2 (see Table 3.4). While equations (3.62) -(3.67) are valid for unmodified gears, γ_{rs} is independent of tooth profile modification.

3.2.2.4 Calculation of the mesh phasing for the planetary gearbox under consideration

This section presents the calculation of phasing for a planetary gearbox with three planets, sun input and carrier output, with the properties given in Table 3.5.

The mesh phasing of different planet-sun mesh γ_{sn} is calculated using the following equation

$$\gamma_{sn} = -\frac{z_s}{2\pi} \times n\psi_n, \psi_n = \frac{\pi}{p}, n = 0,1,2,3 \quad (3.71)$$

Table 3.5 Gear parameters for planetary gearbox

Parameter	Sun	Planet	Ring
Number of teeth	28	36	100
Base radius (mm)	25.5	32.7	90.9
Tip radius (root radius for ring) (mm)	30.20	38.20	97.80
Sun-planet mesh pressure angle: $\alpha_1 = 24.60 \text{ deg}$ Planet-ring mesh pressure angle: $\alpha_2 = 24.60 \text{ deg}$ Tooth thickness of planet at base circle: 5.7072mm Circumferential spacing of planets: 0, $2\pi/3, 4\pi/3$			

where p is the number of planets, which is equal to three in this case. Similarly, the mesh phasing of ring-planet mesh γ_{rn} is given by

$$\gamma_{rn} = \frac{z_r}{2\pi} \times n\psi_n, \psi_n = \frac{\pi}{p}, n = 0,1,2,3 \quad (3.72)$$

To calculate the relative sun-planet and ring-planet mesh phasing, i.e. γ_{rs} , the equations (3.62)-(3.70) are used. The sign of γ_{rs} is decided by which gear is input and the direction of rotation of planetary gear. Here, the assumption is that the ring gear is fixed, the input gear is sun and the direction of rotation of planetary gear is counterclockwise. With the given assumptions, the contact will progress as $B_2P_2Q_3E_2$ and this leads to a negative sign for γ_{rs} .

It has to be noted that the obtained mesh phasing are a fraction of mesh period T_m and if one requires the phasing as time –lead or –lag, the phasing must be multiplied by T_m .

Table 3.6 The calculated values of mesh phasing.

Parameter	Value
γ_{sn}	$\begin{cases} 0 \\ -1/3 \\ -2/3 \end{cases}$
γ_{rn}	$\begin{cases} 0 \\ 1/3 \\ 2/3 \end{cases}$
γ_{rs}	-0.2811

3.2.2.5 Modeling sun gear fault

In an attempt to model gear faults of a planetary gearbox, first sun gear fault is considered. The fault type is gear tooth root crack that influences mesh stiffness of planet-sun gear pair for all planetary gears.

Before including the fault, some definitions are given. One of them is tidal period and for sun gear for instance is define as such [60]: time interval required for sun gear's faulty tooth to mesh with the same planet once again. In this definition, the planetary gears are treated differently.

Phase difference of two planets in a equally-spaced planetary gears, equals $2\pi/N$ where N is the number of planets.

According to Fig 3.42., when the faulty tooth meshes for the next time, the sun gear should at least rotate $2\pi/N$ more than the carrier does such that:

$$\theta_s - \theta_c = 2\pi/N \quad (3.73)$$

The time interval corresponding to this angular difference is [60]

$$t_{sun} = \frac{\theta_s - \theta_c}{\omega_s - \omega_c} = \frac{\theta_s - \theta_c}{N(f_s - f_c)} \quad (3.74)$$

where t_{sun} denotes the time period of faulty sun gear mesh, ω_s and ω_c represents sun and carrier rotational speed, and f_s and f_c indicate sun and carrier frequencies, respectively. Equation (3.73) defines the relationship between carrier and sun frequencies [61]

$$f_{sun} = \frac{Z_s + Z_r}{Z_s} f_c \quad (3.75)$$

where Z_s and Z_r denote the number of teeth of the sun and ring gear, respectively.

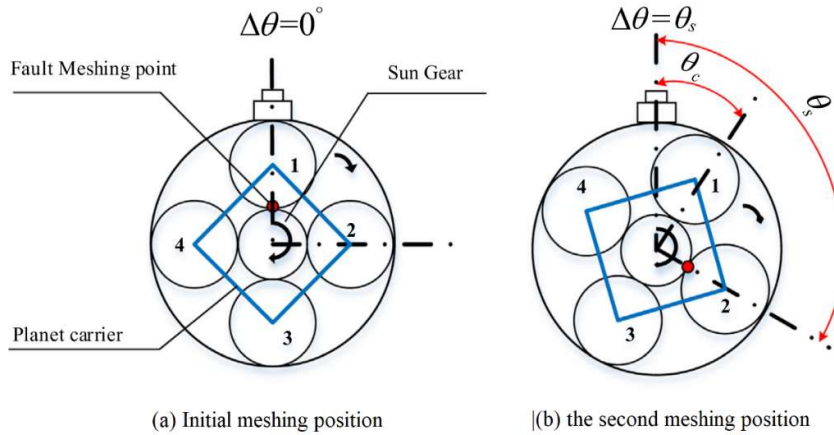


Figure 3.42 Rotation of sun and carrier between two successive fault mesh of sun gear [60]

Using equations (3.74) and (3.75), θ_s and θ_c can be obtained as follows [60]

$$\theta_s = \frac{z_s + z_r}{Nz_r} \cdot 2\pi \quad (3.76)$$

and

$$\theta_c = \frac{z_s}{Nz_r} \cdot 2\pi \quad (3.77)$$

meaning that the sun and carrier angles can readily be calculated once the geometry of the gearbox is known.

Based on the calculations given above, which provides the time period of sun gear fault, crack or pitting can be included in the model. As shown in section 3.2.1.4, tooth root crack causes a reduction in mesh stiffness throughout meshing time of cracked tooth. The process of cracked gear mesh stiffness was given in section 3.2.1.4.

Once the time difference between different planets and faulty sun mesh is considered in the mesh stiffness, the graph of Fig 3.43 is obtained. Here, the mesh phasing between two arbitrarily chosen planets is not considered. By including the mesh phasing, the mesh stiffness functions will be ready for use in the dynamic equations. Fig 3.44 shows a sample graph of planet-sun mesh stiffness for different planets (three planets here). As it can be noticed from the graph, the mesh stiffness of different pairs have a phase difference and it has to be considered in the simulations. Otherwise, the obtained response will not be realistic.

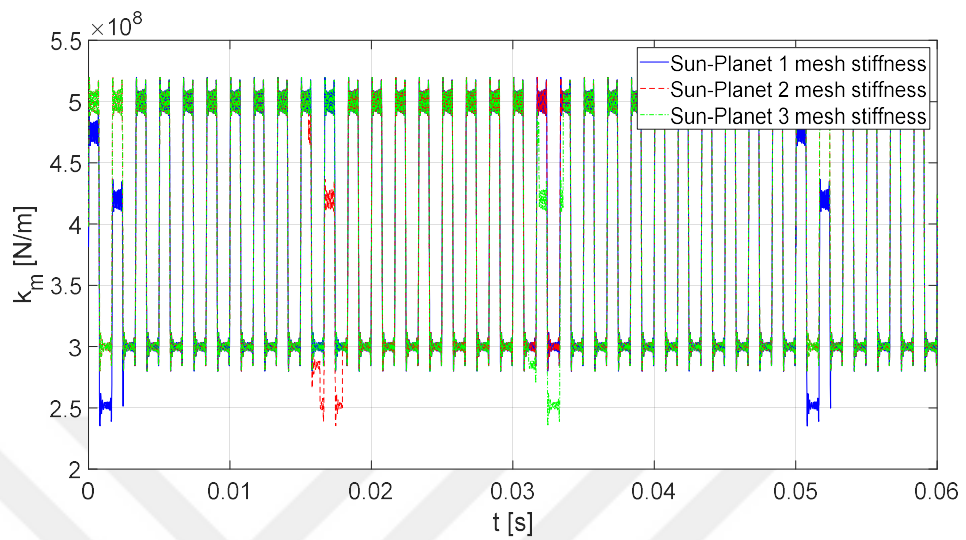


Figure 3.43 Mesh stiffness of different planet-sun meshes for faulty sun gear

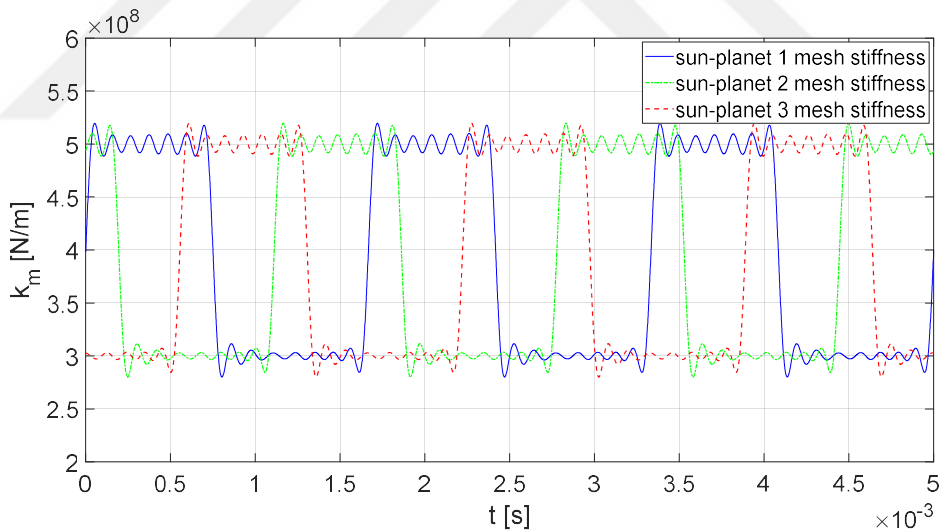


Figure 3.44 Mesh stiffness of different sun gear with different planets with mesh phasing included

Once the dynamic model with faults is obtained, the resulting ODE sets must be solved to generated vibration response of the gearbox. For this purpose, Generalized- α method is employed. In what follows, the method is described.

3.2.2.6 Generalized- α method for the time integration of ODE sets

For the solution of the obtained ODEs in second order form, a method called Generalized- α , will be employed. It has better stability and damping in low and high frequencies. These properties make it a suitable candidate for the time integration of gear dynamics as the order of eigenvalues is much different in gear systems. First introduced by Chung and Hulbert [62], the Generalized- α is a numerical solution method developed for time integration of dynamic systems that offers improved numerical dissipation. The integration algorithms such as the Newmark and Hilber-Hughes-Taylor- α methods are subclasses of the Generalized- α method.

The general matrix form of a linear structural dynamic system can be expressed as

$$\mathbf{M}\ddot{\mathbf{X}} + \mathbf{C}\dot{\mathbf{X}} + \mathbf{K}\mathbf{X} = \mathbf{F} \quad (3.78)$$

where \mathbf{M} , \mathbf{C} and \mathbf{K} stand for the mass, damping and stiffness matrices, respectively. \mathbf{F} and \mathbf{X} denote forcing and displacement vectors, respectively. The equation (3.78), together with the initial conditions given in equation (3.79)-(3.81), forms an initial value problem for which the solution vector $\mathbf{X}(t)$ satisfies the equation (3.78) for all time points in $t \in [0, t_N]$, $t_N > 0$.

$$\mathbf{X}(0) = \mathbf{d} \quad (3.79)$$

$$\dot{\mathbf{X}}(0) = \mathbf{v} \quad (3.80)$$

where \mathbf{d} and \mathbf{v} are prescribed initial displacements and velocities, respectively. In the time integration algorithms, the following forms are used: \mathbf{d}_n , \mathbf{v}_n and \mathbf{a}_n stand as approximations to $\mathbf{X}(t_n)$, $\dot{\mathbf{X}}(t_n)$ and $\ddot{\mathbf{X}}(t_n)$, respectively. The terms \mathbf{d}_{n+1} and \mathbf{v}_{n+1} are expressed based on \mathbf{d}_n , \mathbf{v}_n , \mathbf{a}_n and \mathbf{a}_{n+1} . To determine \mathbf{a}_{n+1} , another equation must be written. This type of equations are called one-step, three-stage time integration methods. It is a one-step method as the solution at time step t_{n+1} is only a function of the solution at t_n . It is a three-stage method due to the fact that the solution is determined by three vectors \mathbf{d}_n , \mathbf{v}_n and \mathbf{a}_n . The Generalized- α method provides an optimal compound of high-frequency and low-frequency dissipation.

Algorithm of the Generalized- α method

According to [62], the Generalized- α method, in its basic form can be expressed by the following equations

$$\mathbf{d}_{n+1} = \mathbf{d}_n + \Delta t \mathbf{v}_n + \Delta t^2 \left(\left(\frac{1}{2} - \beta \right) \mathbf{a}_n + \beta \mathbf{a}_{n+1} \right) \quad (3.81)$$

$$\mathbf{v}_{n+1} = \mathbf{v}_n + \Delta t ((1 - \gamma) \mathbf{a}_n + \gamma \mathbf{a}_{n+1}) \quad (3.82)$$

$$\mathbf{M} \mathbf{a}_{n+1-\alpha_m} + \mathbf{C} \mathbf{v}_{n+1-\alpha_f} + \mathbf{K} \mathbf{d}_{n+1-\alpha_f} = \mathbf{F} (t_{n+1-\alpha_f}) \quad (3.83)$$

$$\mathbf{d}_0 = \mathbf{d} \quad (3.84)$$

$$\mathbf{v}_0 = \mathbf{v} \quad (3.85)$$

$$\mathbf{a}_0 = \mathbf{M}^{-1} (\mathbf{F}(0) - \mathbf{C} \mathbf{v} - \mathbf{K} \mathbf{d}) \quad (3.86)$$

where

$$\mathbf{d}_{n+1-\alpha_f} = (1 - \alpha_f) \mathbf{d}_{n+1} + \alpha_f \mathbf{d}_n \quad (3.87)$$

$$\mathbf{v}_{n+1-\alpha_f} = (1 - \alpha_f) \mathbf{v}_{n+1} + \alpha_f \mathbf{v}_n \quad (3.88)$$

$$\mathbf{a}_{n+1-\alpha_m} = (1 - \alpha_m) \mathbf{a}_{n+1} + \alpha_m \mathbf{a}_n \quad (3.89)$$

$$t_{n+1-\alpha_f} = (1 - \alpha_f) t_{n+1} + \alpha_f t_n \quad (3.90)$$

where $n \in \{0, 1, \dots, N - 1\}$, N denotes the number of time steps and Δt represents time step. The equations (3.81) and (3.82) are the same of Newmark method. The algorithmic parameters α_f , α_m , β and γ are given as follows [62]

$$\gamma = \frac{1}{2} - \alpha_m + \alpha_f \quad (3.91)$$

$$\beta = \frac{1}{4} (1 - \alpha_m + \alpha_f)^2 \quad (3.92)$$

$$\alpha_m = \frac{1}{2} \quad (3.93)$$

$$\alpha_f = \frac{1}{2} \quad (3.94)$$

It has to be noted that the given values for α_m and α_f are typical values for a stable algorithm and the Generalized- α algorithm is unconditionally stable for [62]

$$\alpha_m \leq \alpha_f \leq \frac{1}{2}, \beta \geq \frac{1}{4} + \frac{1}{2}(\alpha_f - \alpha_m) \quad (3.95)$$

The Generalized- α method allows for the solution of the ODEs in second order form without a need for transforming them to first order ODE set.

3.2.2.7 Results and discussion

In this simulation, the angular speed of the input gear, i.e., sun, was given as 360rpm . Subsequently, the angular acceleration of the sun, carrier and planets of the linear system were calculated for one revolution of the carrier. Figures 3.45-3.47 show the accelerations of sun, carrier and planet gear, respectively. In Fig 3.45-a, shows the acceleration throughout the revolution of carrier, and 3.45-b focuses in a smaller period to demonstrate its variation after it has reached a steady-state. The acceleration of the carrier and one of the planets is depicted in Figs 3.46 and 3.47, respectively. As it can be seen, all of the responses have periodic patterns. Fig 3.48, shows the acceleration of faulty sun gear. As it can be noticed, when the faulty gear meshes with sun or ring gear, an impulse is generated which lasts for a short time.

A characteristic frequency which is a feature of gear systems is gear mesh frequency which is common between all gears. It can be calculated as $f_m = N_p f_p$, where N_p and f_p represent tooth number and rotation frequency of planetary gear. To check for the mesh frequency, FFT of the response is obtained and the spectra are investigated in frequency domain. The gear mesh frequency equals 600Hz for the gear system under study. Generally, it is expected to have the mesh frequency and its harmonics in gear vibration response. The figures 3.49-3.51 illustrate frequency spectrum of different gears. Gear mesh frequency and harmonics can be clearly noticed in the

graphs. This is clearer in case of pinion gear FFT and the third harmonic is dominant in the given frequency band.

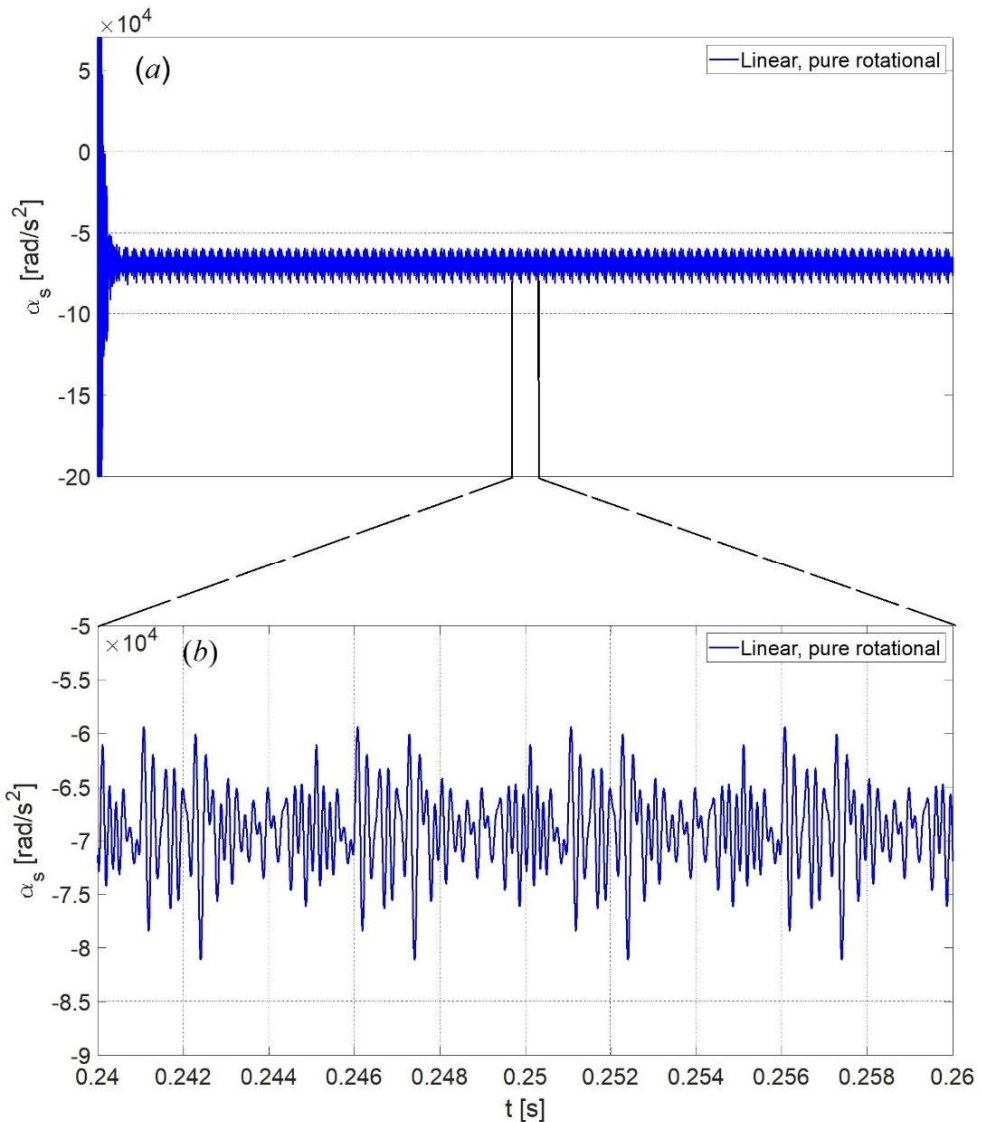


Figure 3.45 Sun gear acceleration, healthy gearbox

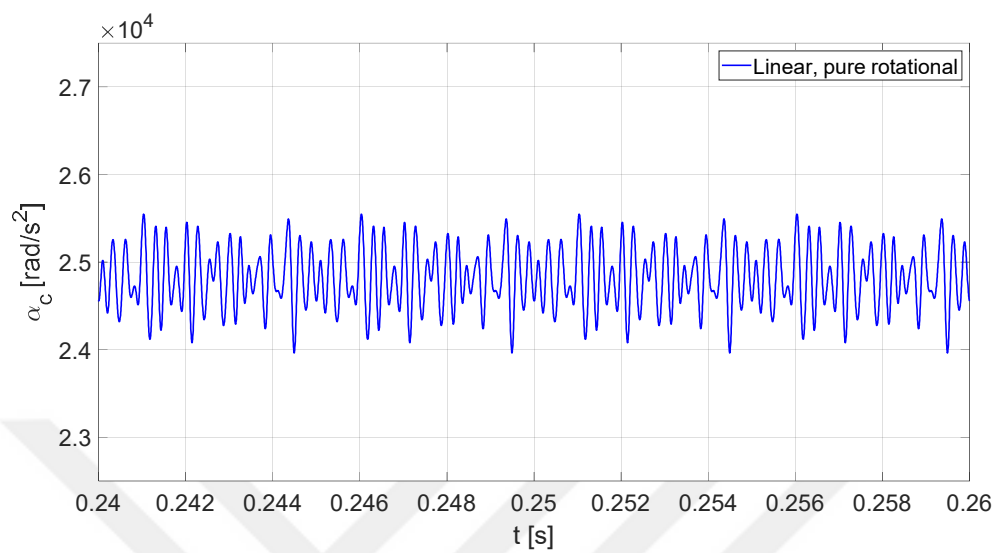


Figure 3.46 Carrier acceleration, healthy gearbox

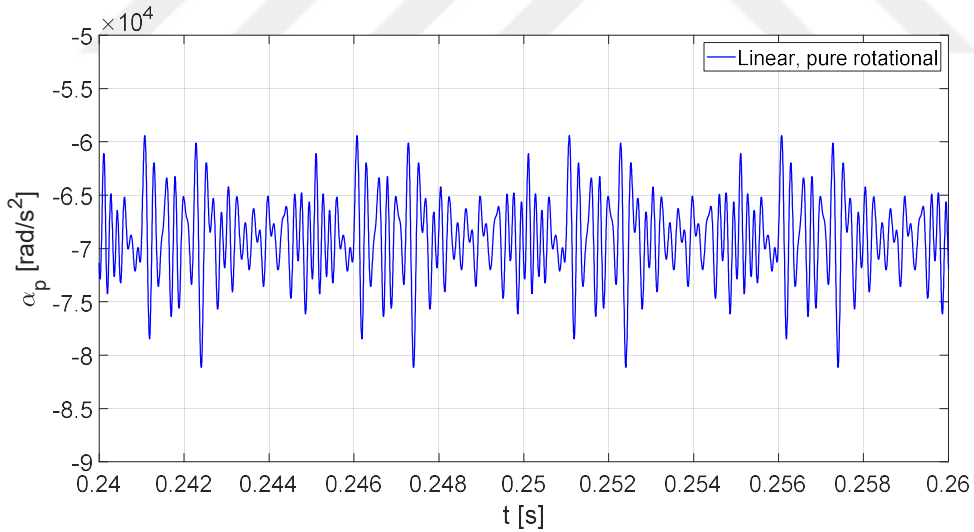


Figure 3.47 Planetary gear acceleration, healthy gearbox

When it comes to faulty gearbox with a faulty sun gear, the effect of sun gear tooth crack will show itself as impulses generated in a certain period. The spectra of the

response, other than mesh frequency which shared among all gears, will be quite different as well. The effect of fault can be better identified through its symptoms in frequency domain. To detect fault symptoms, the FFT of faulty gear response is analyzed and shown in Figure 3.52. The fault shows itself by sidebands spaced around gear mesh frequency given by [63]: $kf_m + lf_c + pf_s$ ($n \in N$, $l, p \in Z$). According to the given equation, the sidebands are detected in the FFT that suggests that a sun gear fault exists. Such sideband frequencies were not present as expected.

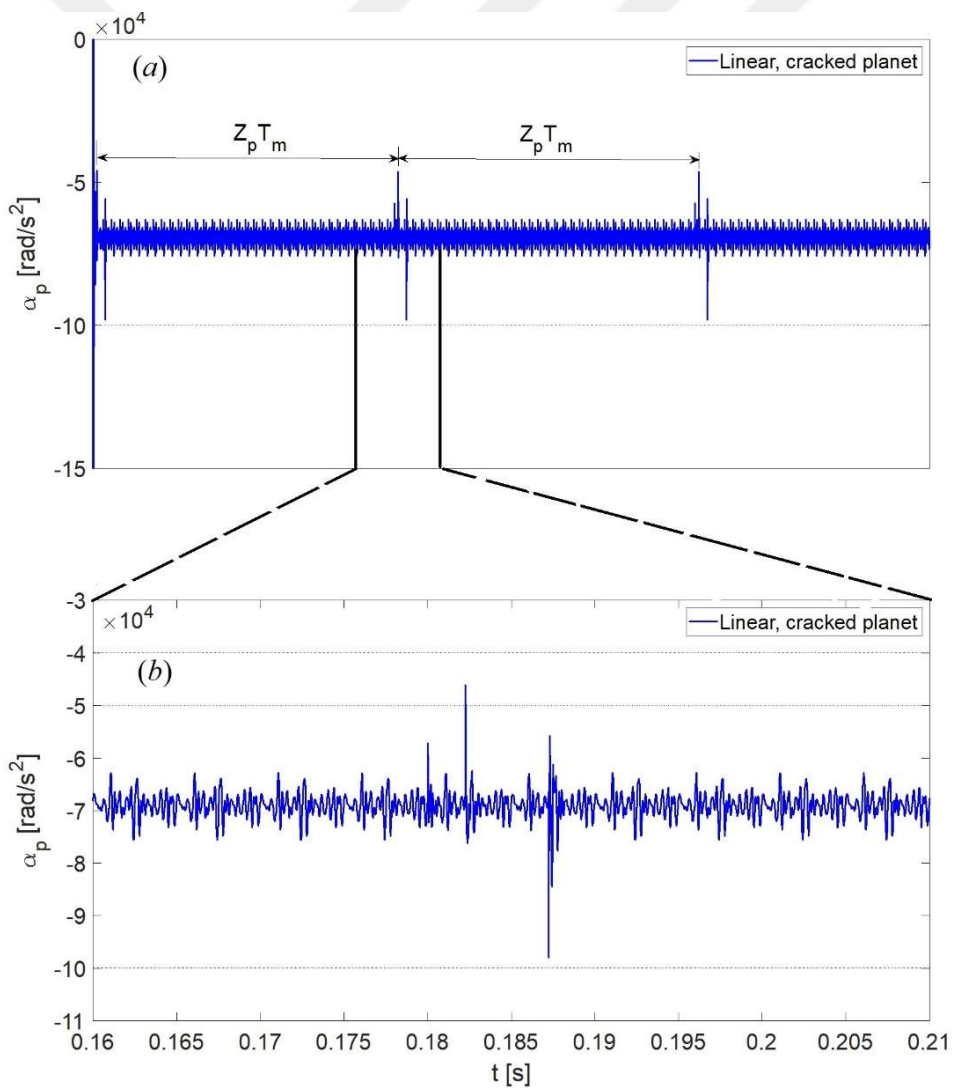


Figure 3.48 Acceleration of faulty planet gear, cracked planet

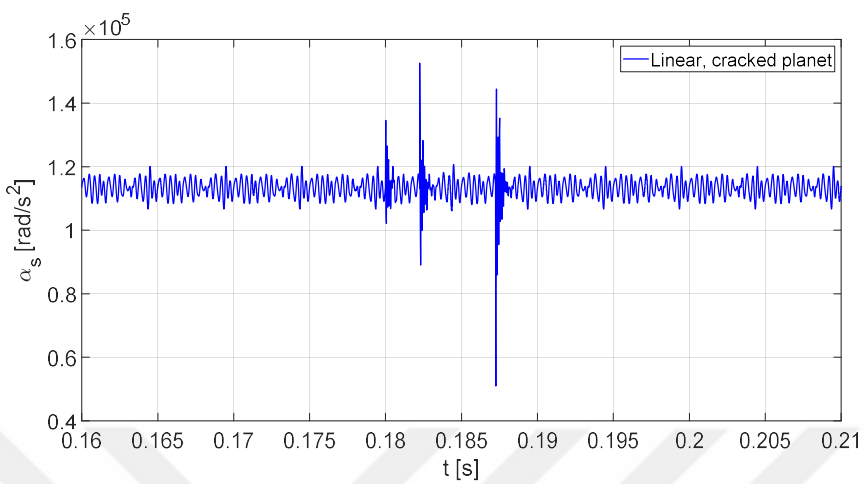


Figure 3.49 Acceleration of sun gear, cracked planet

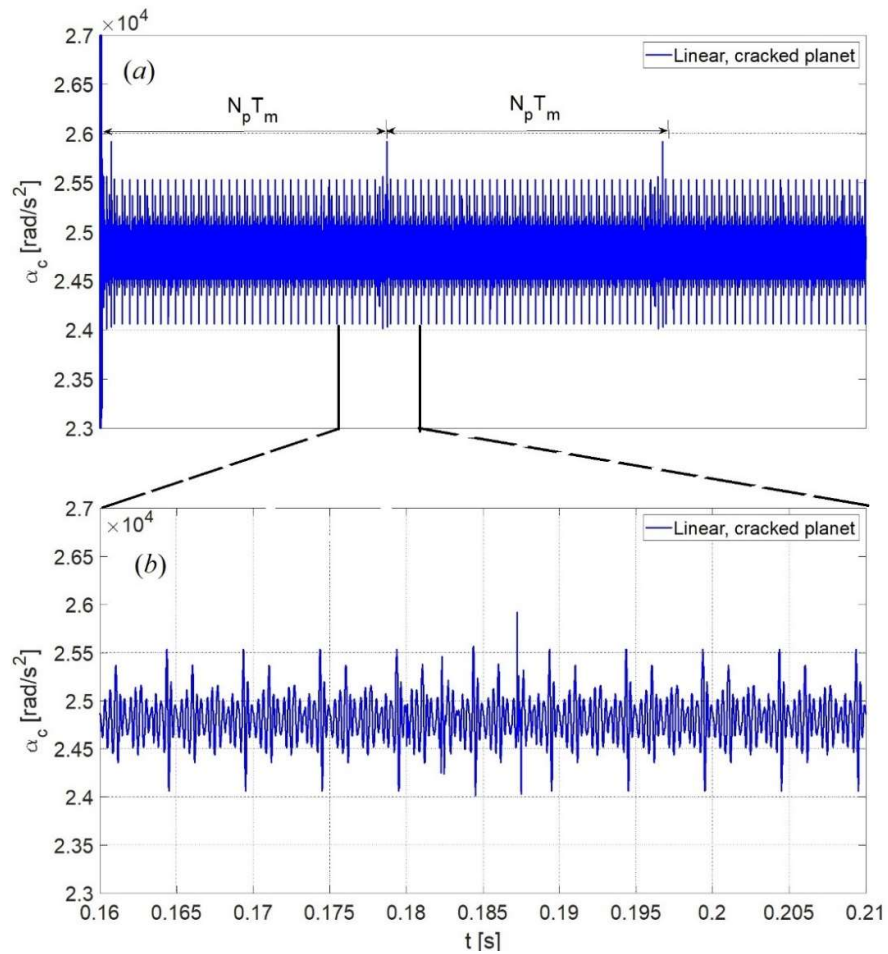


Figure 3.50 Acceleration of the carrier, cracked planet

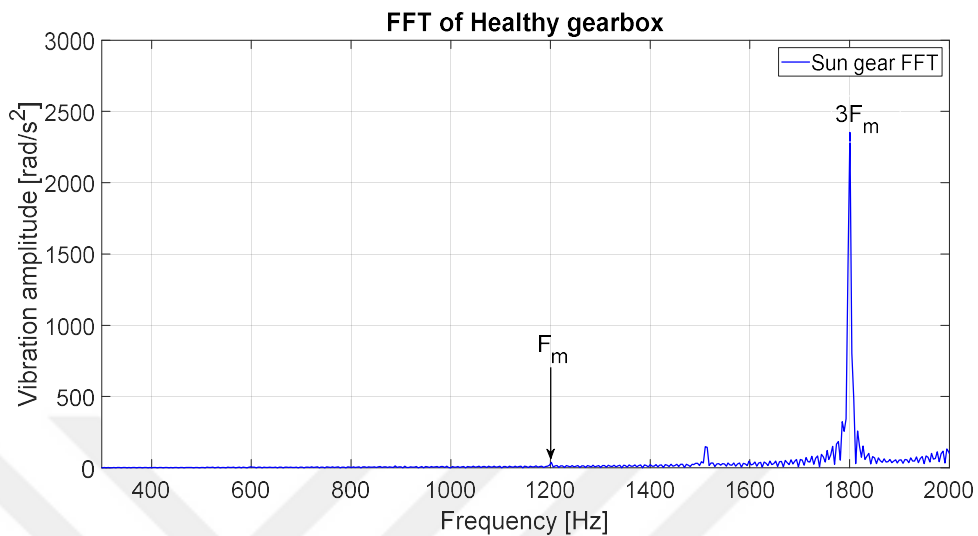


Figure 3.51 FFT of sun gear acceleration, healthy gearbox

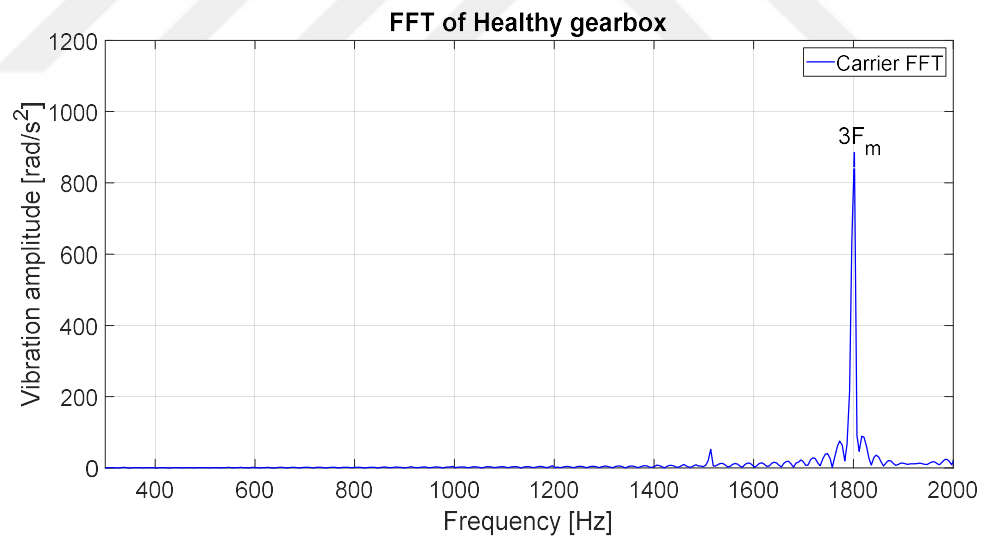


Figure 3.52 FFT of carrier acceleration, healthy gearbox

Fig 3.55, depicts the FFT of sun gear acceleration for healthy and faulty cases. Although the frequencies precisely match for both cases, appearance of sideband

frequencies around mesh harmonics is notable. For instance, Fig 3.55-b shows the sidebands around harmonic fifteen of gear mesh frequency which is due to the crack.

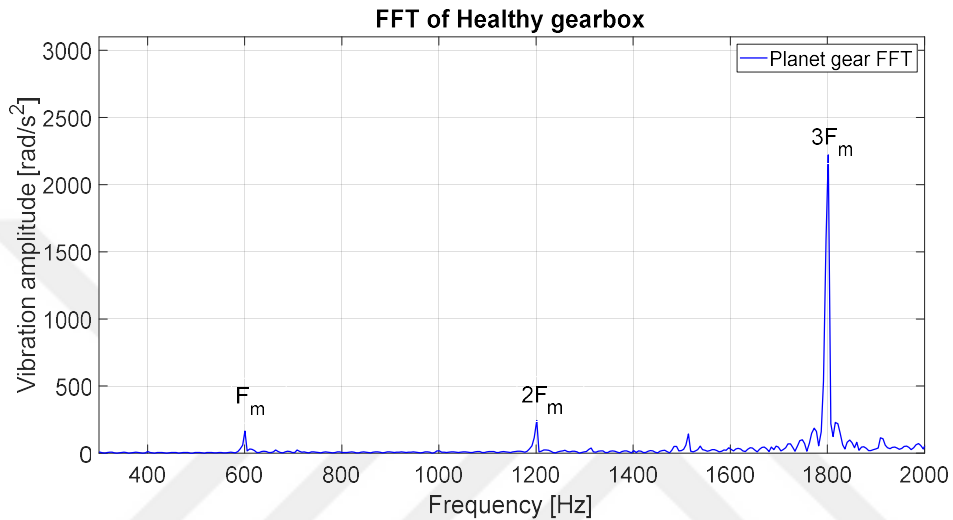


Figure 3.53 FFT of a planetary gear acceleration, healthy gearbox

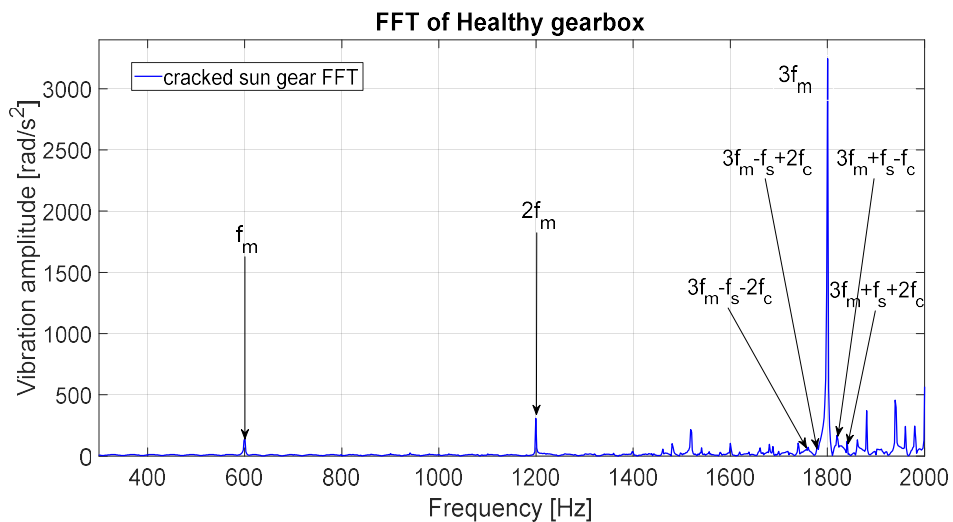
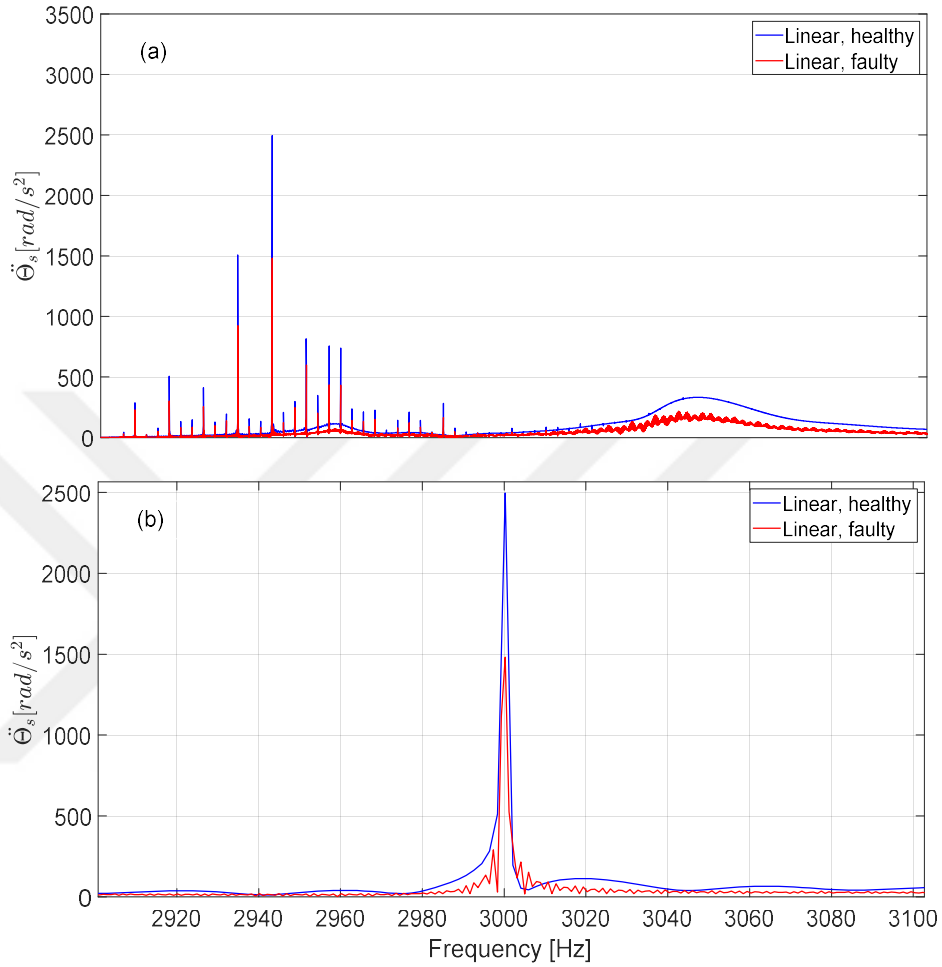


Figure 3.54 FFT of sun gear acceleration, cracked sun



3.55 FFT of sun gear acceleration, healthy vs cracked planet (a) general view, (b) smaller frequency interval

3.2.2.7.1 Conclusion

In this section, a purely rotational six DOF planetary gear system was modelled with the effects of sun gear fault and time varying mesh included. The fault considered here is sun gear crack which causes a reduction in mesh stiffness during meshing of faulty tooth with planetary gears. The method of modeling cracked mesh stiffness was developed in the spur gear dynamic analysis part of the current study. The same

idea is used for sun-planet pair and the mesh stiffness is modified accordingly. To obtain the mesh stiffness, the period of sun-planet mesh for faulty tooth must be considered. Therefore, it was included in the mesh stiffness function to achieve the required faulty gear mesh stiffness. Furthermore, the relative mesh phasing between different gear pairs were properly calculated and included in the mesh stiffness functions.

The obtained equations of motion in second order ODE form were integrated with Generalized- α method and the response of the gear system was analyzed in time and frequency domains. According to the obtained results, the fault mainly shows itself by impulsive pattern in time domain and certain sideband frequencies around mesh frequency harmonics.

The model will be further extended to include the effect of gear bearings, carrier and sun gear shaft flexibility as it was carried out in the modal analysis part of the study. It will allow the analysis of the response transmitted through bearings which is more realistic.

3.2.3 Non-linear dynamic modeling of a planetary gear system including translational DOFs of the gears with a planet gear fault

In this subsection, a planetary gear non-linear dynamic model which includes translational DOFs of the bearings, in healthy and faulty cases will be developed. The fault considered, is a tooth root crack of one of the planets. It is assumed that the direction of rotation of the input gear, i.e., sun, is such that the tooth crack is opened when the faulty tooth meshes with the sun gear. Therefore, only the mesh stiffness of the planet-sun pair will be decreased when the faulty tooth meshes.

Fig 3.55 presents the schematic view of the gear system which includes bearing stiffnesses. The DOFs include the rotation of the planets, sun and carrier, and translational motions of the gears and carrier. Therefore, the system will have fifteen DOFs. The ring gear is fixed and the sun gear is considered as the input gear.

According to the Figure 3.56, the position vector of the sun and carrier can be expressed as follows

$$\mathbf{r}_s = x_s \hat{i} + y_s \hat{j}, \quad \mathbf{r}_c = x_c \hat{i} + y_c \hat{j} \quad (3.96)$$

where x_s, y_s and x_c, y_c are displacements of sun and carrier in the x and y directions, respectively. The position vector of the i -th planet gear with respect to the origin, is written as

$$\mathbf{r}_s = \mathbf{r}_c + \mathbf{r}'_i + \boldsymbol{\rho}_i \quad (3.97)$$

where \mathbf{r}'_i denotes the position vector of the planet with respect to carrier center and $\boldsymbol{\rho}_i$ is the relative position of the planet with respect its connection point with the carrier. The vectors \mathbf{r}'_i and $\boldsymbol{\rho}_i$ can be expressed as

$$\mathbf{r}'_i = R_c [\cos(\theta_c + \varphi_i) \hat{i} + \sin(\theta_c + \varphi_i) \hat{j}], \quad \boldsymbol{\rho}_i = \xi_i e_{\xi_i} + \eta_i e_{\eta_i} \quad (3.98)$$

where R_c is the radial distance of planet bearing center from the carrier centers, φ_i represents the initial angular positions of the planets. Since they are symmetrically located, the angles are $\varphi_1 = 0, \varphi_2 = 120^\circ$, and $\varphi_3 = 240^\circ$. The DOFs ξ_i and η_i are radial and tangential motions of the planet i , relative to their connection points to the carrier. The absolute position vector of the planet i , can be expressed as

$$\mathbf{r}_i = x_i \hat{i} + y_i \hat{j} \quad (3.99)$$

where x_i and y_i can be obtained from the following equation

$$\begin{aligned} x_i &= x_c + (\xi_i + R_c) \cos(\theta_c + \varphi_i) - \eta_i \sin(\theta_c + \varphi_i), \\ y_i &= y_c + (\xi_i + R_c) \sin(\theta_c + \varphi_i) + \eta_i \cos(\theta_c + \varphi_i) \end{aligned} \quad (3.100)$$

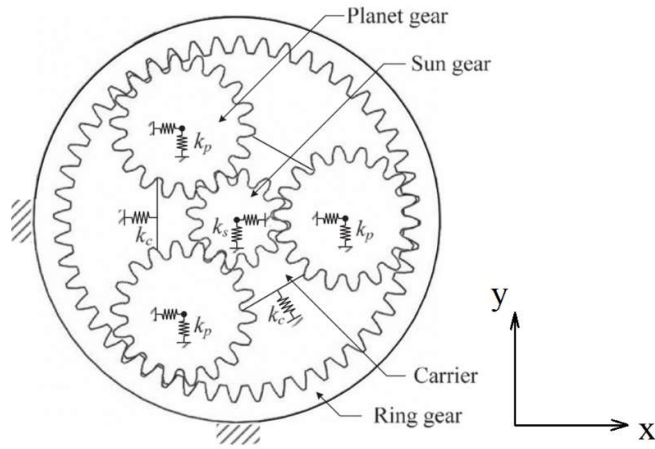


Figure 3.57 Lumped parameter model of a planetary gear system [49]

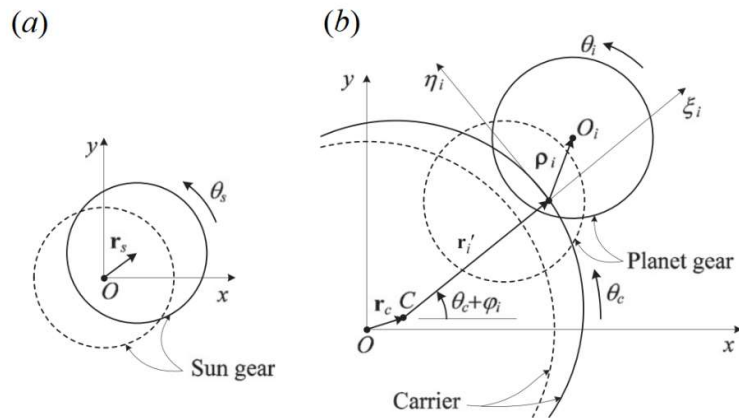


Figure 3.58 Initial and displaced locations of (a) sun gear; (b) carrier and planet [49]

The gear mesh deformation between the sun and the planet i can be obtained considering the mesh configuration as shown in Fig 3.58. The sun-planet mesh stiffness is represented by k_i^s , the pressure angle of contact for the sun-planet is α_i^s and the instantaneous angular position of the planets with respect to sun gear is

shown by ψ_i^s . The base circle radius of the sun and planets are expressed by R_s and R_p , respectively.

In a similar fashion, the mesh model between the ring and planet i is shown in Fig 3.59, where k_i^r is the mesh stiffness of the ring-planet i pair, α_i^r is the pressure angle of contact, ψ_i^r represents the position angle of the planet i relative to the ring, and R_r denotes the base radius of the ring gear.

The angles ψ_i^s and ψ_i^r at each time instant can be calculated using the following equations.

$$\psi_i^s = \frac{y_i - y_s}{x_i - x_s}, \quad \psi_i^r = \frac{y_i}{x_i}, \quad i = 1, 2, 3 \quad (3.101)$$

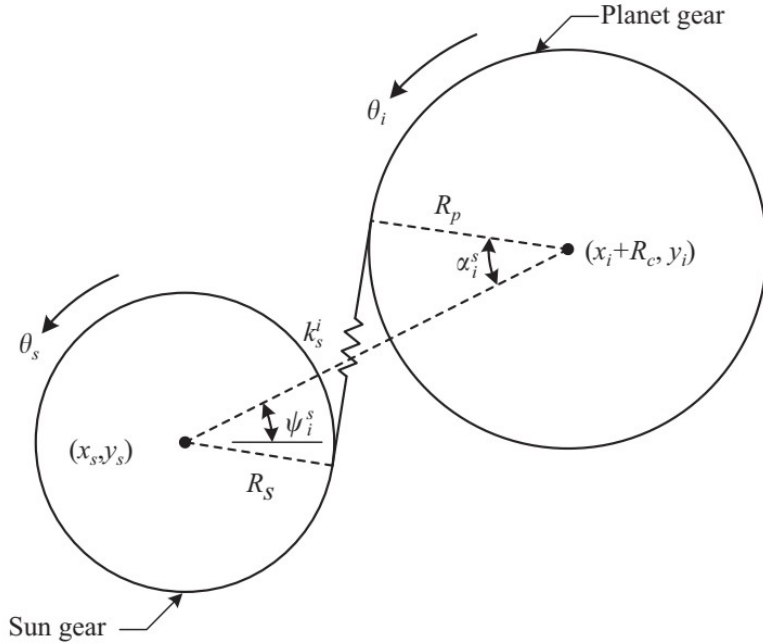


Figure 3.59 Gear mesh between sun and planet i [49]

The DOFs of the gear system are defined as

$$\{x_s, y_s, u_s, x_c, y_c, \theta_c, \xi_1, \eta_1, \theta_1, \xi_2, \eta_2, \theta_2, \eta_2, \xi_3, \eta_3, \theta_3\} \quad (3.102)$$

The equations of motion are obtained with the use of Lagrange's equation which is written as follows

$$\frac{d}{dt} \left(\frac{\partial T}{\partial \dot{q}_i} \right) - \frac{\partial T}{\partial q_i} + \frac{\partial V}{\partial q_i} = Q_i, i = 1, \dots, N; N = \text{no. of DOFs} \quad (3.103)$$

The potential and kinetic energy must be calculated before the application of Lagrange's equation. The equations of motion are given in a concise form, for more detailed expressions, the reader is referred to Appendix A. They can be obtained as follows

Kinetic energy

$$T = \frac{1}{2} m_s (\dot{y}_s^2 + \dot{x}_s^2) + \frac{1}{2} I_s \dot{\theta}_s^2 + \frac{1}{2} m_c (\dot{y}_c^2 + \dot{x}_c^2) + \frac{1}{2} I_c \dot{\theta}_c^2 + \frac{1}{2} \sum_{i=1}^3 [m_p (\dot{x}_i^2 + \dot{y}_i^2) + I_p (\dot{\theta}_c + \dot{\theta}_i)^2] \quad (3.104)$$

$\theta_i, i = 1, 2, 3$: angular displacement of planet i

Potential energy

$$V = \frac{1}{2} \sum_{i=1}^3 k_i^s (\delta_i^s)^2 + \frac{1}{2} \sum_{i=1}^3 k_i^r (\delta_i^r)^2 + \frac{1}{2} k_s (x_s^2 + y_s^2) + \frac{1}{2} \sum_{i=1}^3 k_p (\xi_i^2 + \eta_i^2) + \frac{1}{2} k_c (x_c^2 + y_c^2) \quad (3.105)$$

The sun-planet and planet-ring contact pressure angles are as follows:

$$\alpha_i^s = \alpha_i^r = 24.6^\circ$$

The gear mesh deformation for the planets are defined as

δ_i^s : gear mesh deformation between sun and i -th planet

δ_i^r : gear mesh deformation between ring and i -th planet

and are obtained using the following equations

$$\begin{aligned}
\delta_i^s &= [x_s - x_c - \cos(\theta_c + \varphi_i) \xi_i + \sin(\theta_c + \varphi_i) \eta_i] \sin(\alpha_i^s - \psi_i^s) + \\
&[y_s - y_c - \sin(\theta_c + \varphi_i) \xi_i - \cos(\theta_c + \varphi_i) \eta_i] \cos(\alpha_i^s - \psi_i^s) + R_s(\theta_s - \theta_c) + R_p \theta_i
\end{aligned} \tag{3.106}$$

$$\begin{aligned}
\delta_i^r &= [x_c + \cos(\theta_c + \varphi_i) \xi_i - \sin(\theta_c + \varphi_i) \eta_i] \sin(\alpha_i^r + \psi_i^r) - [y_c + \\
&\sin(\theta_c + \varphi_i) \xi_i + \cos(\theta_c + \varphi_i) \eta_i] \cos(\alpha_i^r + \psi_i^r) - R_r \theta_c - R_p \theta_i
\end{aligned} \tag{3.107}$$

Derivatives of potential energy terms can be obtained using the following equations

$$\frac{\partial V}{\partial y_s} = \sum_{i=1}^3 k_i^s \frac{\partial \delta_i^s}{\partial y_s} \delta_i^s + k_s y_s, \quad \frac{\partial \delta_i^s}{\partial y_s} = \cos(\alpha_i^s - \psi_i^s) \tag{3.108}$$

$$\frac{\partial V}{\partial x_s} = \sum_{i=1}^3 k_i^s \frac{\partial \delta_i^s}{\partial x_s} \delta_i^s + k_s x_s, \quad \frac{\partial \delta_i^s}{\partial x_s} = \sin(\alpha_i^s - \psi_i^s) \tag{3.109}$$

$$\frac{\partial V}{\partial \theta_s} = \sum_{i=1}^3 k_i^s \frac{\partial \delta_i^s}{\partial \theta_s} \delta_i^s, \quad \frac{\partial \delta_i^s}{\partial \theta_s} = R_s \tag{3.110}$$

$$\frac{\partial V}{\partial x_c} = k_c x_c + \sum_{i=1}^3 \left(k_i^s \frac{\partial \delta_i^s}{\partial x_c} \delta_i^s + k_i^r \frac{\partial \delta_i^r}{\partial x_c} \delta_i^r \right) \tag{3.111}$$

$$\frac{\partial V}{\partial y_c} = k_c y_c + \sum_{i=1}^3 \left(k_i^s \frac{\partial \delta_i^s}{\partial y_c} \delta_i^s + k_i^r \frac{\partial \delta_i^r}{\partial y_c} \delta_i^r \right) \tag{3.112}$$

$$\frac{\partial V}{\partial \theta_c} = \sum_{i=1}^3 \left(k_i^s \frac{\partial \delta_i^s}{\partial \theta_c} \delta_i^s + k_i^r \frac{\partial \delta_i^r}{\partial \theta_c} \delta_i^r \right) \tag{3.113}$$

$$\begin{aligned}
\frac{\partial \delta_i^s}{\partial \theta_c} &= [\sin(\theta_c + \varphi_i) \xi_i + \cos(\theta_c + \varphi_i) \eta_i] \sin(\alpha_i^s - \psi_i^s) + [-\cos(\theta_c + \varphi_i) \xi_i + \\
&\sin(\theta_c + \varphi_i) \eta_i] \cos(\alpha_i^s - \psi_i^s) - R_s
\end{aligned} \tag{3.114}$$

$$\begin{aligned}
\frac{\partial \delta_i^r}{\partial \theta_c} &= [-\sin(\theta_c + \varphi_i) \xi_i - \cos(\theta_c + \varphi_i) \eta_i] \sin(\alpha_i^r + \psi_i^r) - [-\cos(\theta_c + \varphi_i) \xi_i - \\
&\sin(\theta_c + \varphi_i) \eta_i] \cos(\alpha_i^r + \psi_i^r) - R_r
\end{aligned} \tag{3.115}$$

$$\frac{\partial V}{\partial \xi_j} = \left(k_p \xi_i + k_i^s \frac{\partial \delta_i^s}{\partial \xi_j} \delta_i^s + k_i^r \frac{\partial \delta_i^r}{\partial \xi_j} \delta_i^r \right) \delta_{ij} \tag{3.116}$$

where δ_{ij} is the Kronecker delta.

$$\frac{\partial \delta_i^s}{\partial \xi_j} = -[\cos(\theta_c + \varphi_j) \sin(\alpha_j^s - \psi_j^s) + \sin(\theta_c + \varphi_j) \cos(\alpha_j^s - \psi_j^s)] \tag{3.117}$$

$$\frac{\partial \delta_i^r}{\partial \xi_j} = [\cos(\theta_c + \varphi_j) \sin(\alpha_j^r + \psi_j^r) - \sin(\theta_c + \varphi_j) \cos(\alpha_j^r + \psi_j^r)] \quad (3.118)$$

$$\frac{\partial V}{\partial \eta_j} = \left(k_p \eta_i + k_i^s \frac{\partial \delta_i^s}{\partial \eta_i} \delta_i^s + k_i^r \frac{\partial \delta_i^r}{\partial \eta_i} \delta_i^r \right) \delta_{ij} \quad (3.119)$$

$$\frac{\partial \delta_i^s}{\partial \eta_j} = [\sin(\theta_c + \varphi_i) \sin(\alpha_i^s - \psi_i^s) - \cos(\theta_c + \varphi_i) \cos(\alpha_i^s - \psi_i^s)] \delta_{ij} \quad (3.120)$$

$$\frac{\partial \delta_i^r}{\partial \eta_j} = -[\sin(\theta_c + \varphi_i) \sin(\alpha_i^r + \psi_i^r) + \cos(\theta_c + \varphi_i) \cos(\alpha_i^r + \psi_i^r)] \delta_{ij} \quad (3.121)$$

$$\frac{\partial V}{\partial \theta_j} = (k_i^s R_p \delta_i^s - k_i^r R_p \delta_i^r) \delta_{ij} \quad (3.122)$$

Derivatives of the kinetic energy terms are calculated as follows

$$\frac{d}{dt} \left(\frac{\partial T}{\partial \dot{x}_s} \right) = m_s \ddot{x}_s \quad (3.123)$$

$$\frac{d}{dt} \left(\frac{\partial T}{\partial \dot{y}_s} \right) = m_s \ddot{y}_s \quad (3.124)$$

$$\frac{d}{dt} \left(\frac{\partial T}{\partial \dot{\theta}_s} \right) = I_s \ddot{\theta}_s \quad (3.125)$$

$$\frac{d}{dt} \left(\frac{\partial T}{\partial \dot{x}_c} \right) = m_c \ddot{x}_c + \sum_{i=1}^3 m_p \ddot{x}_i \quad (3.126)$$

where

$$\begin{aligned} \ddot{x}_i &= \ddot{x}_c + \ddot{\xi}_i \cos(\theta_c + \varphi_i) - 2\dot{\xi}_i \dot{\theta}_c \sin(\theta_c + \varphi_i) - (\xi_i + R_c) \ddot{\theta}_c \sin(\theta_c + \varphi_i) - \\ &(\xi_i + R_c) \dot{\theta}_c^2 \cos(\theta_c + \varphi_i) - \ddot{\eta}_i \sin(\theta_c + \varphi_i) - 2\dot{\eta}_i \dot{\theta}_c \cos(\theta_c + \varphi_i) - \\ &\eta_i \ddot{\theta}_c \cos(\theta_c + \varphi_i) + \eta_i \dot{\theta}_c^2 \sin(\theta_c + \varphi_i) \end{aligned} \quad (3.127)$$

$$\begin{aligned} \ddot{y}_i &= \ddot{y}_c + \ddot{\xi}_i \sin(\theta_c + \varphi_i) + 2\dot{\xi}_i \dot{\theta}_c \cos(\theta_c + \varphi_i) + (\xi_i + R_c) \ddot{\theta}_c \cos(\theta_c + \varphi_i) - \\ &(\xi_i + R_c) \dot{\theta}_c^2 \sin(\theta_c + \varphi_i) + \ddot{\eta}_i \cos(\theta_c + \varphi_i) - 2\dot{\eta}_i \dot{\theta}_c \sin(\theta_c + \varphi_i) - \\ &\eta_i \ddot{\theta}_c \sin(\theta_c + \varphi_i) - \eta_i \dot{\theta}_c^2 \cos(\theta_c + \varphi_i) \end{aligned} \quad (3.128)$$

$$\frac{d}{dt} \left(\frac{\partial T}{\partial \dot{y}_c} \right) = m_c \ddot{y}_c + \sum_{i=1}^3 m_p \ddot{y}_i \quad (3.129)$$

$$\frac{\partial T}{\partial \dot{\theta}_c} = I_c \dot{\theta}_c + \sum_{i=1}^3 m_p \left[\dot{x}_i \frac{\partial \dot{x}_i}{\partial \dot{\theta}_c} + \dot{y}_i \frac{\partial \dot{y}_i}{\partial \dot{\theta}_c} \right] + \sum_{i=1}^3 I_p (\dot{\theta}_c + \dot{\theta}_i) \quad (3.130)$$

$$\frac{\partial \dot{x}_i}{\partial \dot{\theta}_c} = -[(\xi_i + R_c) \sin(\theta_c + \varphi_i) + \eta_i \cos(\theta_c + \varphi_i)] \quad (3.131)$$

$$\frac{\partial \dot{y}_i}{\partial \dot{\theta}_c} = [(\xi_i + R_c) \cos(\theta_c + \varphi_i) - \eta_i \sin(\theta_c + \varphi_i)] \quad (3.132)$$

$$\frac{\partial T}{\partial \theta_c} = \sum_{i=1}^3 m_p \left[\dot{x}_i \frac{\partial \dot{x}_i}{\partial \theta_c} + \dot{y}_i \frac{\partial \dot{y}_i}{\partial \theta_c} \right] \quad (3.133)$$

Since in the Lagrange's equation the term $\frac{d}{dt} \left(\frac{\partial T}{\partial \dot{\theta}_c} \right) - \frac{\partial T}{\partial \theta_c}$ will appear simultaneously, the overall term should be obtained.

The same approach is used for ξ_i and η_i coordinates such that the following terms are calculated

$$\frac{d}{dt} \left(\frac{\partial T}{\partial \dot{\xi}_i} \right) - \frac{\partial T}{\partial \xi_i}, \frac{d}{dt} \left(\frac{\partial T}{\partial \dot{\eta}_i} \right) - \frac{\partial T}{\partial \eta_i} \quad (3.134)$$

For the coordinate θ_i , the derivatives are straightforward, and can be expressed as

$$\frac{d}{dt} \left(\frac{\partial T}{\partial \dot{\theta}_i} \right) = I_p \ddot{\theta}_c + I_p \ddot{\theta}_i \quad (3.135)$$

The equations of motions, are obtained by plugin in the derivatives. Subsequently, the equation of motion can be arranged as follows

$$\mathbf{M}(\mathbf{x}) \ddot{\mathbf{x}} + \mathbf{N}(\mathbf{x}, \dot{\mathbf{x}}) = \mathbf{f} \quad (3.136)$$

where \mathbf{M} is the mass matrix, \mathbf{N} represents the non-linear force vector, \mathbf{f} denotes the external force vector, and \mathbf{x} is the displacement vector. Here, \mathbf{N} is a combination of linear and non-linear stiffness, and non-linear mass related terms.

3.2.3.1 Solution

In the solution phase which is realized by the Generalized-Alpha method, given the initial values, the initial guess for the displacement, velocity and acceleration, can be obtained from the following equation

$$\mathbf{d}_0 = \mathbf{x}(0), \mathbf{v}_0 = \dot{\mathbf{x}}(0), \mathbf{a}_0 = -M^{-1}(\mathbf{x}(0))N(\mathbf{x}(0), \dot{\mathbf{x}}(0)) \quad (3.137)$$

Before solving the equations of motions to get the response, to reduce the computational cost, they are left multiplied by the transpose of the modal matrix Φ^T . The matrix Φ^T includes mass-normalized mode vectors of the time invariant linear system calculated using a mean mesh stiffness value. The vector \mathbf{x} is substituted by $\mathbf{x} = \Phi\mathbf{q}$, where \mathbf{q} denotes the modal coordinates corresponding to the linear system discussed above.

Once the above-mentioned operations are carried out, the equations of motions in its residual form can be expressed as follows

$$\begin{bmatrix} 1 & \dots & 0 \\ \vdots & \ddots & \vdots \\ 0 & \dots & 1 \end{bmatrix} \{\ddot{\mathbf{q}}\} + 2\zeta \begin{bmatrix} \omega_1 & \dots & 0 \\ \vdots & \ddots & \vdots \\ 0 & \dots & \omega_r \end{bmatrix} \{\dot{\mathbf{q}}\} + \begin{bmatrix} \omega_1^2 & \dots & 0 \\ \vdots & \ddots & \vdots \\ 0 & \dots & \omega_r^2 \end{bmatrix} \{\mathbf{q}\} + \Phi^T \{K^t \Phi \mathbf{q} + M^t \Phi \ddot{\mathbf{q}} - f(t)\} = \{0\} \quad (3.138)$$

where K^t and M^t are time dependent parts of the linear stiffness and mass matrices, respectively. K_N and M_N denote non-linear stiffness and mass related force vectors, respectively. $f(t)$ is the force vector, $\omega_r, r = 1, \dots, N$ represents r -th natural frequency of the system, where N is the number of the DOFs. ζ is the modal damping ratio. Through this application, it is assumed that the damping matrix is proportional with the mass matrix.

3.2.3.2 Validation of the non-linear model

In this subsection, to validate the non-linear model at the first stage, the response of the system with very large bearing stiffness values ($k_p = k_c = k_s = 10^{18} N/m$) is compared with that of the purely rotational linear system. The comparison is carried out in time domain and subsequently in frequency domain via FFT. Fig 3.60, demonstrates the time domain response of the sun gear of the non-linear system with rigid bearings, while Fig 3.61 shows the response of the purely rotational model. As it can be seen, the results compare well both qualitatively and quantitatively. Since

a comparison in time domain is not straightforward or accurate, it is performed in the frequency domain via FFT analysis.

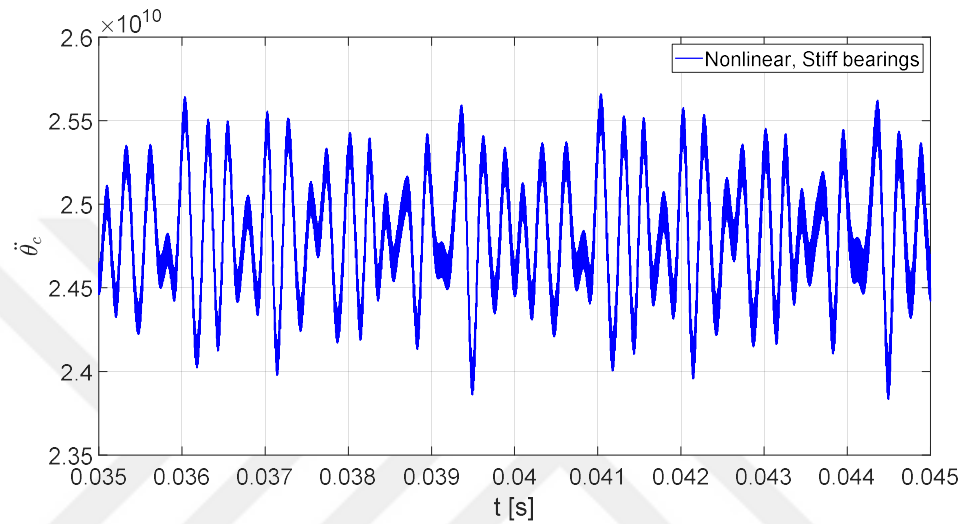


Figure 3.60 Angular acceleration of sun gear, purely rotational model

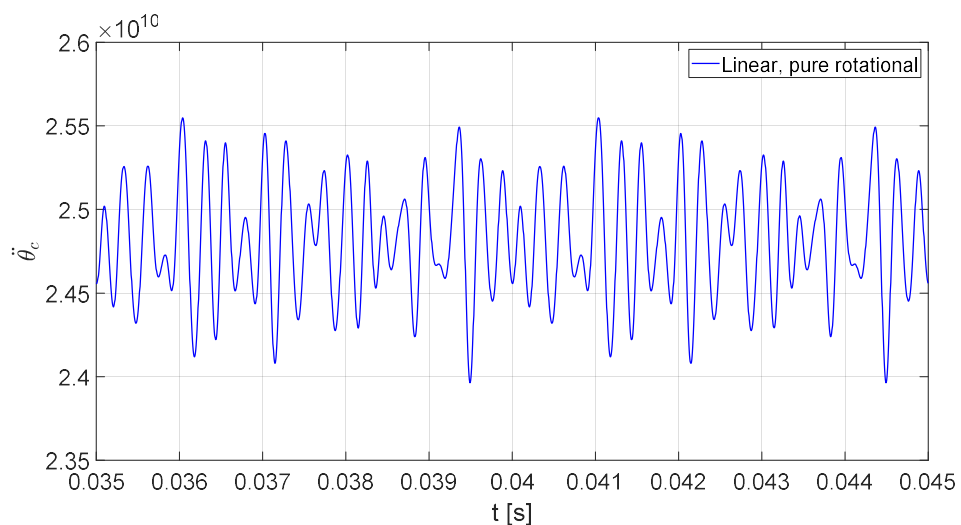


Figure 3.61. Angular acceleration of sun gear, non-linear model

Fig 3.62, depicts the FFT of sun gear acceleration of the both systems. Once more, the results are approximately equal which validates the non-linear model. In Fig 3.62, other than a smooth background curve with a relatively smooth peaks which are the natural frequencies, there exist spiky peaks. They are associated with gear mesh frequency and its harmonics. Gear mesh frequency (GMF) appears due to the parametric excitation of the mesh stiffness and it is one of the characteristics frequencies in a gear system's dynamic response.

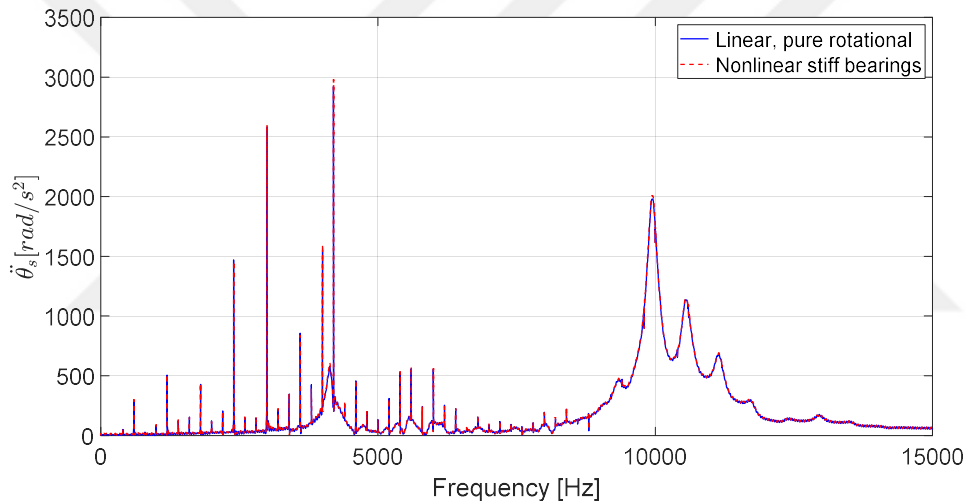


Figure 3.62 Comparison of FFT of sun gear angular acceleration for non-linear case with $k_p = k_c = k_s = 10^{18} N / m$ and purely rotational model

3.2.3.3 Results of the non-linear system and discussion

As the correctness of the non-linear model is validated, further analysis is carried out using the model.

In the first part, the response of the healthy system is presented and subsequently the results of the faulty gearbox are demonstrated.

3.2.3.3.1 The dynamic response of the healthy gear system

Figs 3.63-3.68 presents the response of the nonlinear planetary gear system along different DOFs. In each figure, first a general view of the response for one revolution of the carrier is depicted and then it is focused on a specific part to show the vibration trend. Some of the outputs, such as \ddot{x}_s , shown in Fig 3.66, might seem growing large with time, however, the trend is of a periodic nature and only a segment of it is shown here.

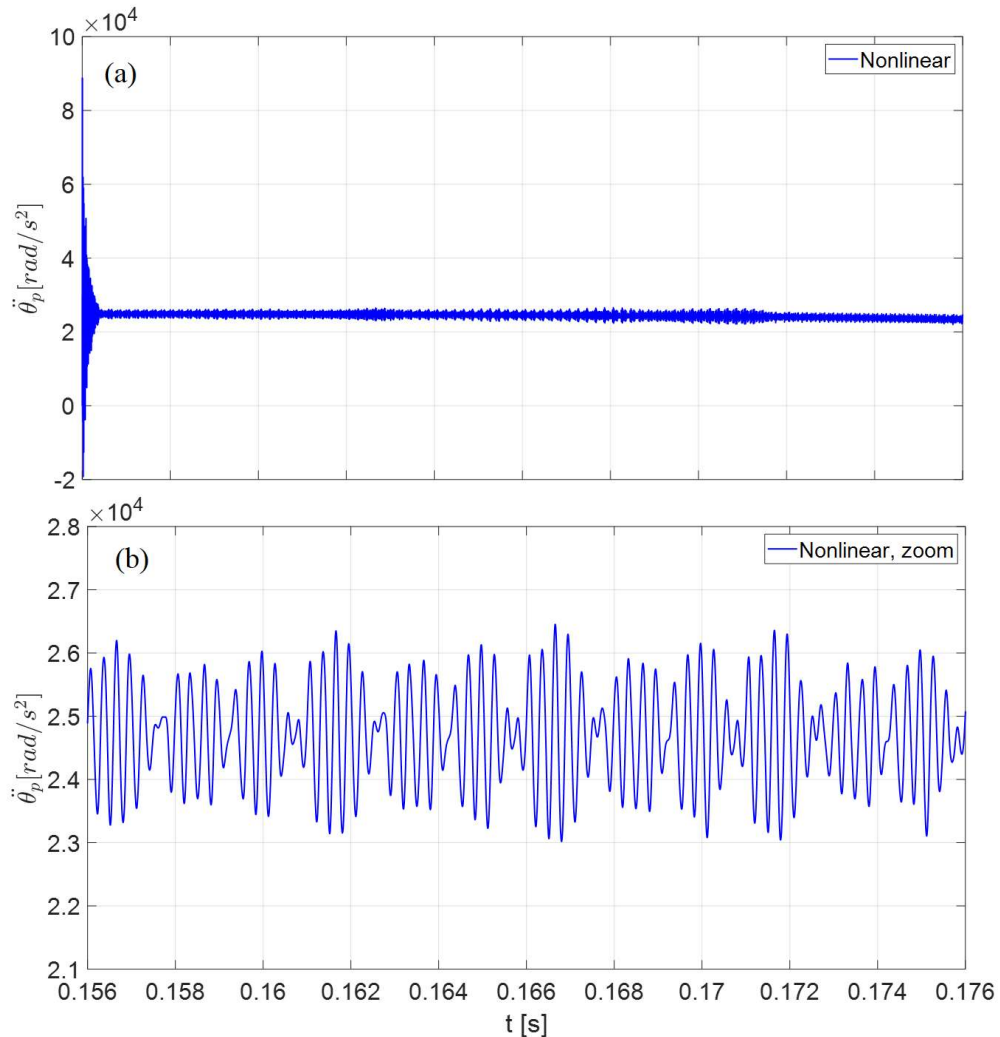


Figure 3.63 Angular acceleration of a planet, healthy nonlinear system

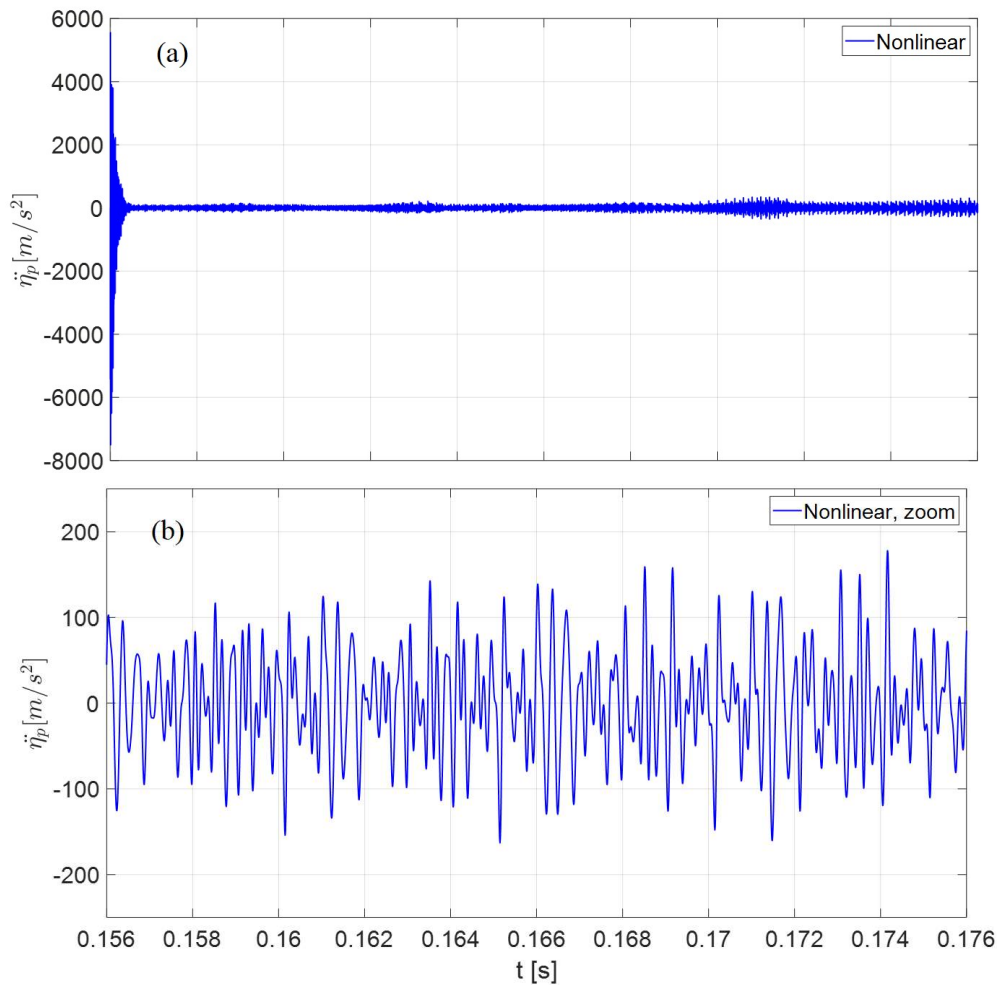


Figure 3.64 Translational acceleration of a planet in radial direction η , healthy nonlinear system

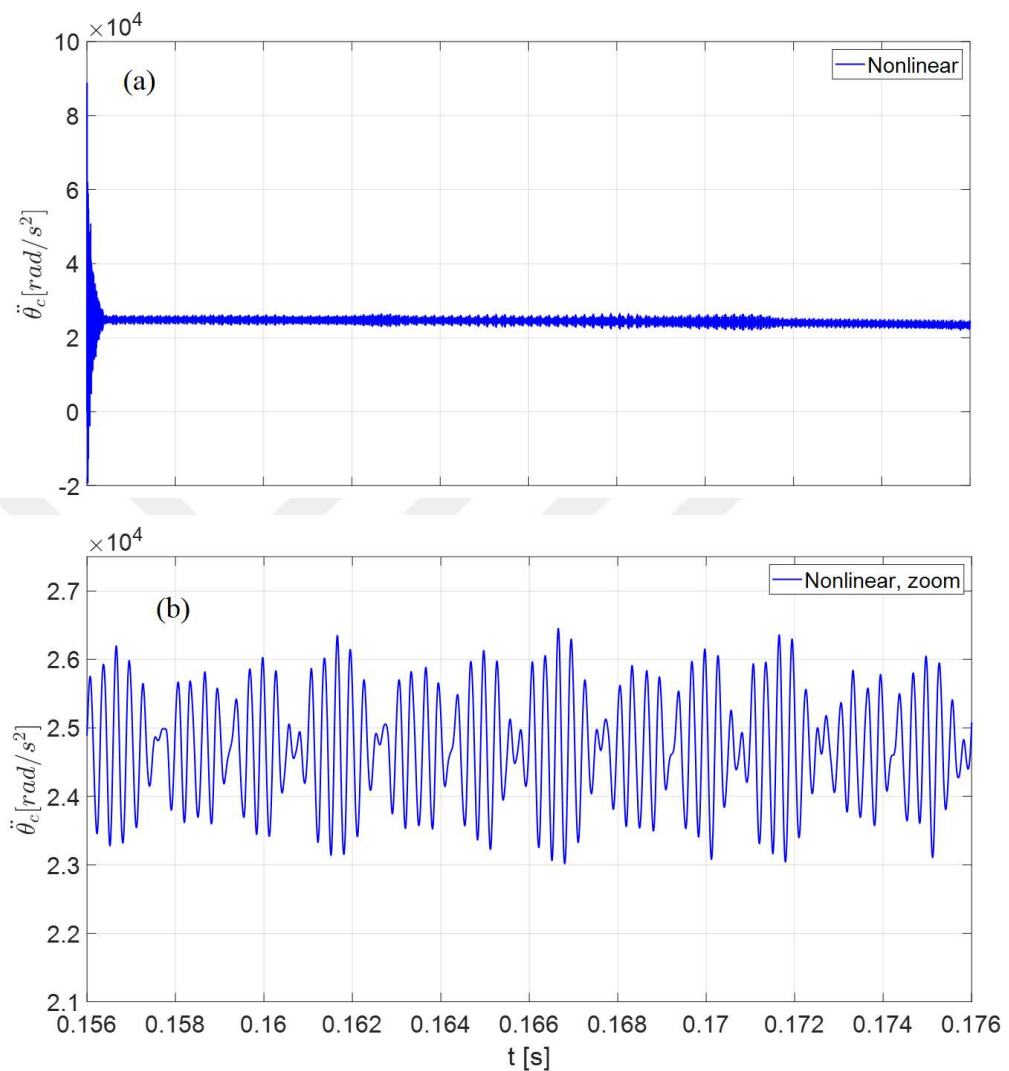


Figure 3.65 Angular acceleration of the carrier, healthy nonlinear system

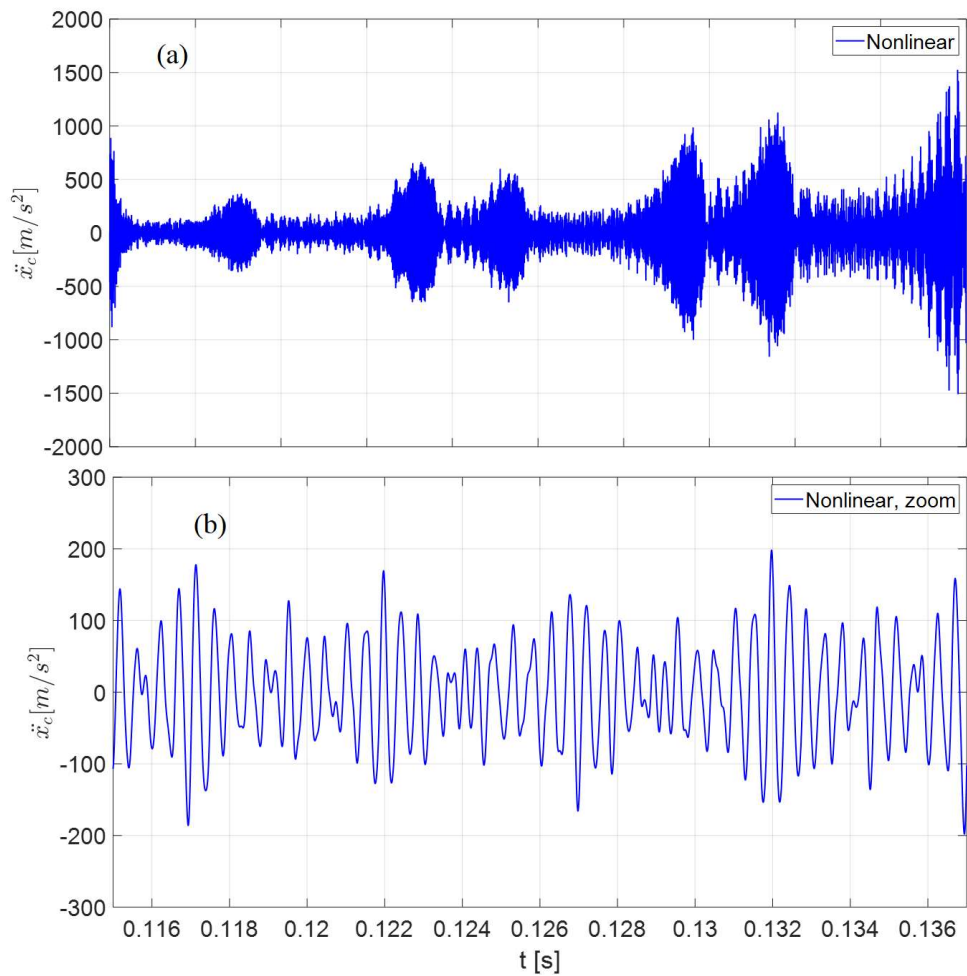


Figure 3.66 Translational acceleration of the carrier in x direction, healthy nonlinear system

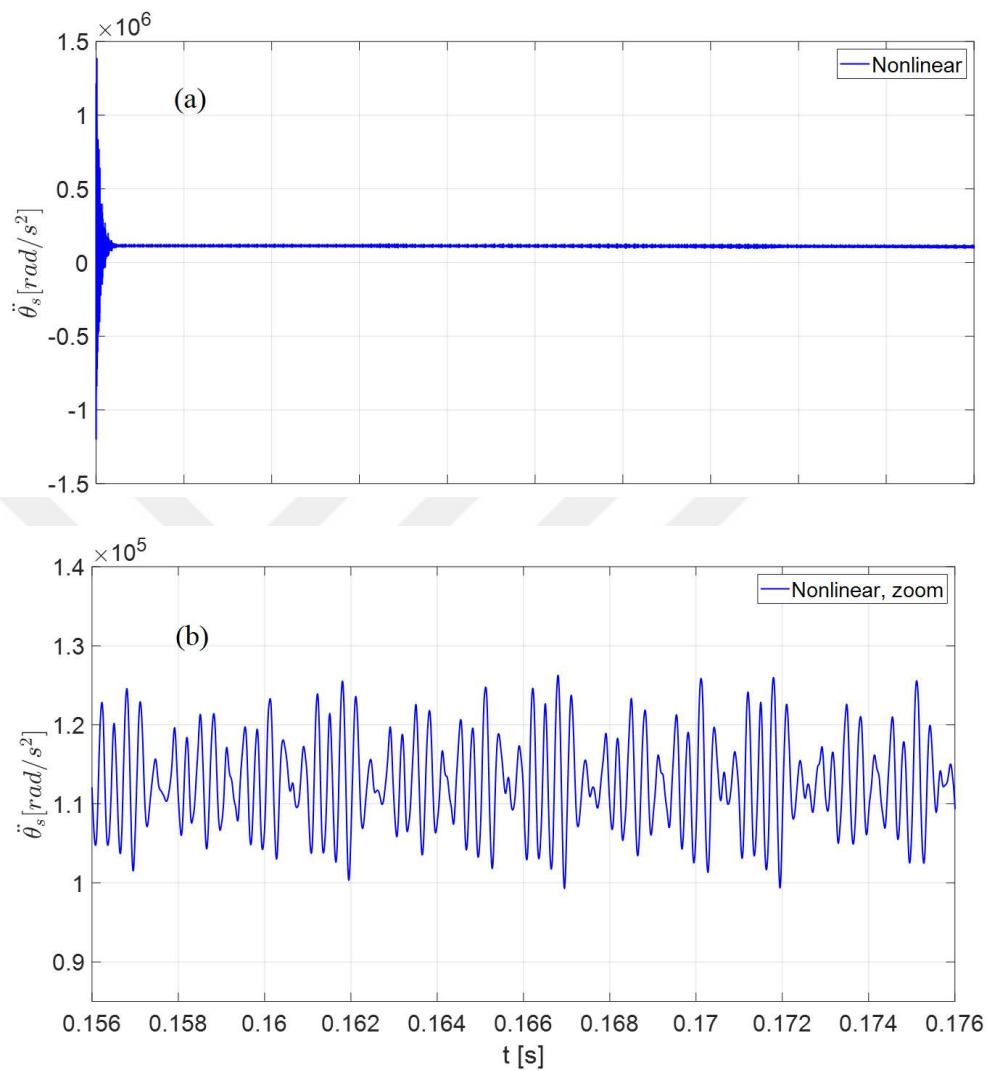


Figure 3.67 Angular acceleration of the sun gear, healthy nonlinear system

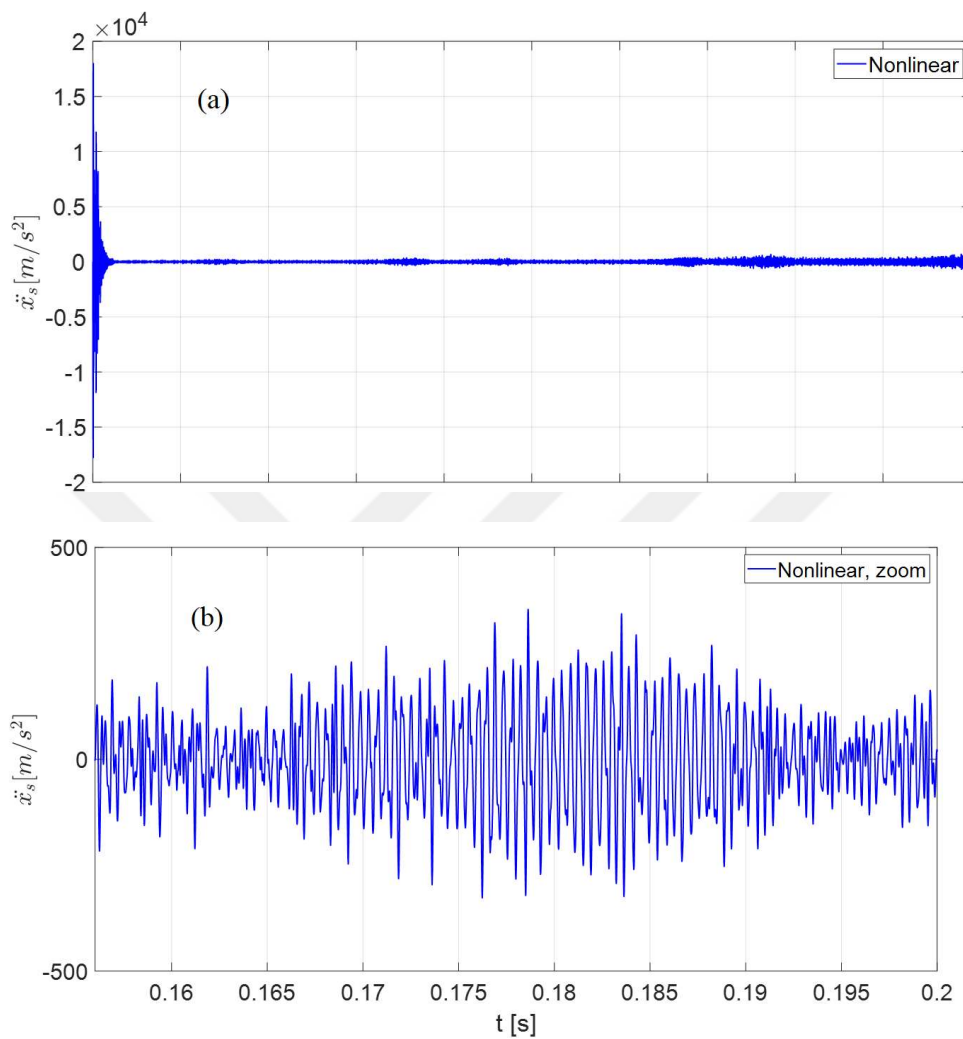


Figure 3.68 Translational acceleration of the sun gear in x direction, healthy nonlinear system

3.2.3.3.2 Results of the faulty system

In this subsection, the dynamic response of the nonlinear planetary gear system is presented. Figs 3.69-3.71 demonstrates the response of the faulty gearbox with planet tooth crack along some specific directions. These are selected among the outputs as

the fault it is most identifiable in them. As it can be noticed, the effect of the fault is an impulse which is repeated in a specific period related to planet gear angular speed.

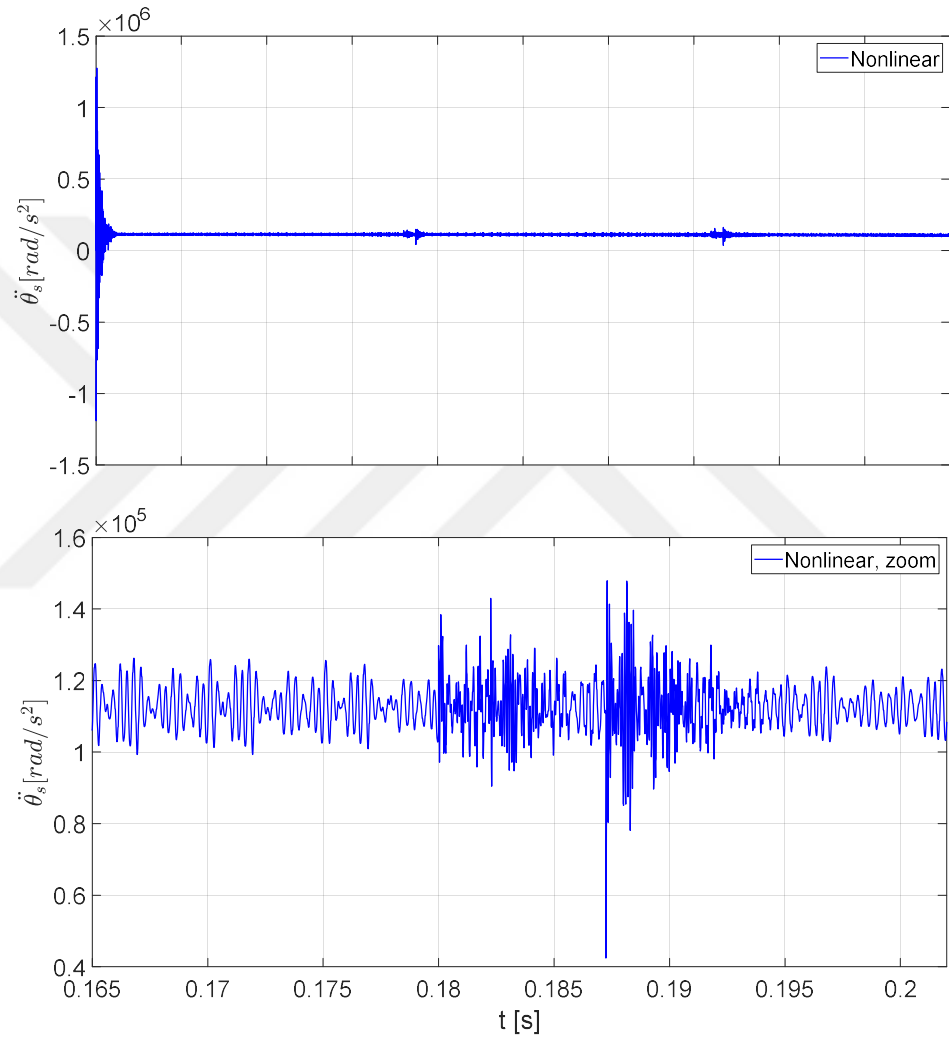


Figure 3.69 Angular acceleration of the sun gear, faulty nonlinear system

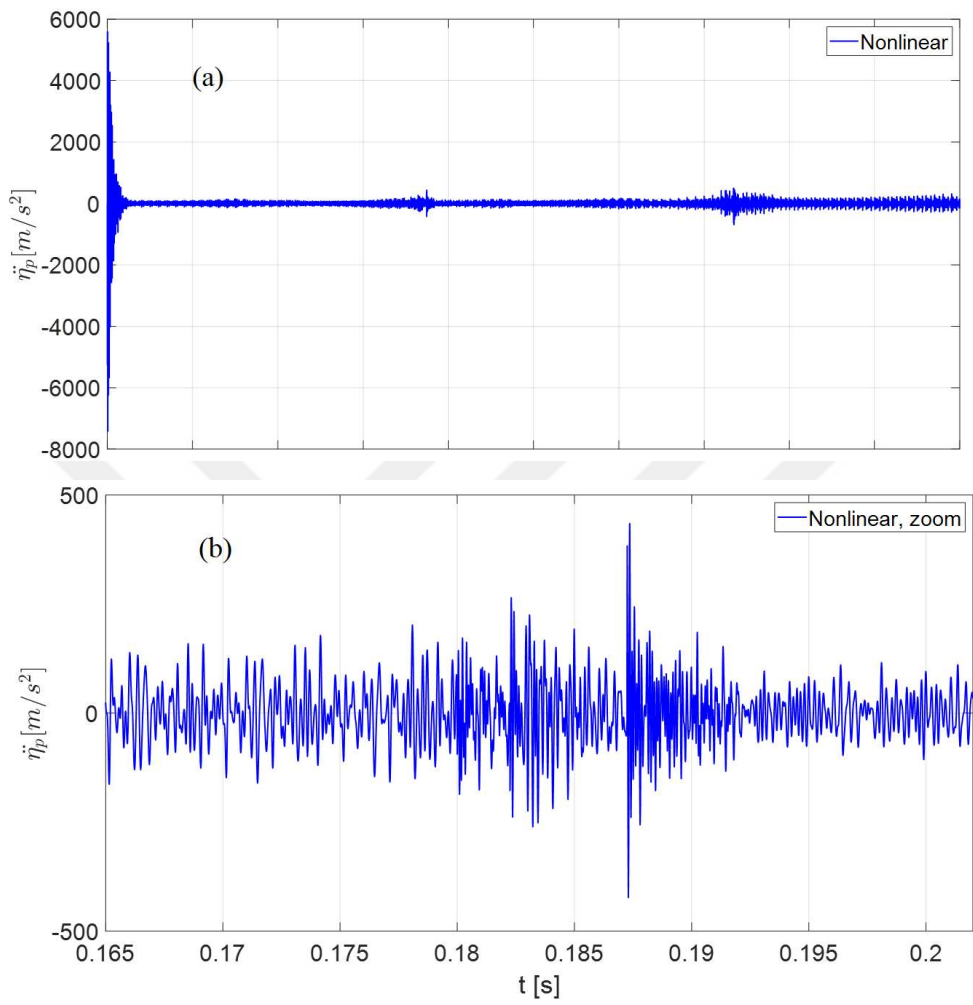


Figure 3.70 Translational acceleration of a planet in radial direction η , healthy nonlinear system

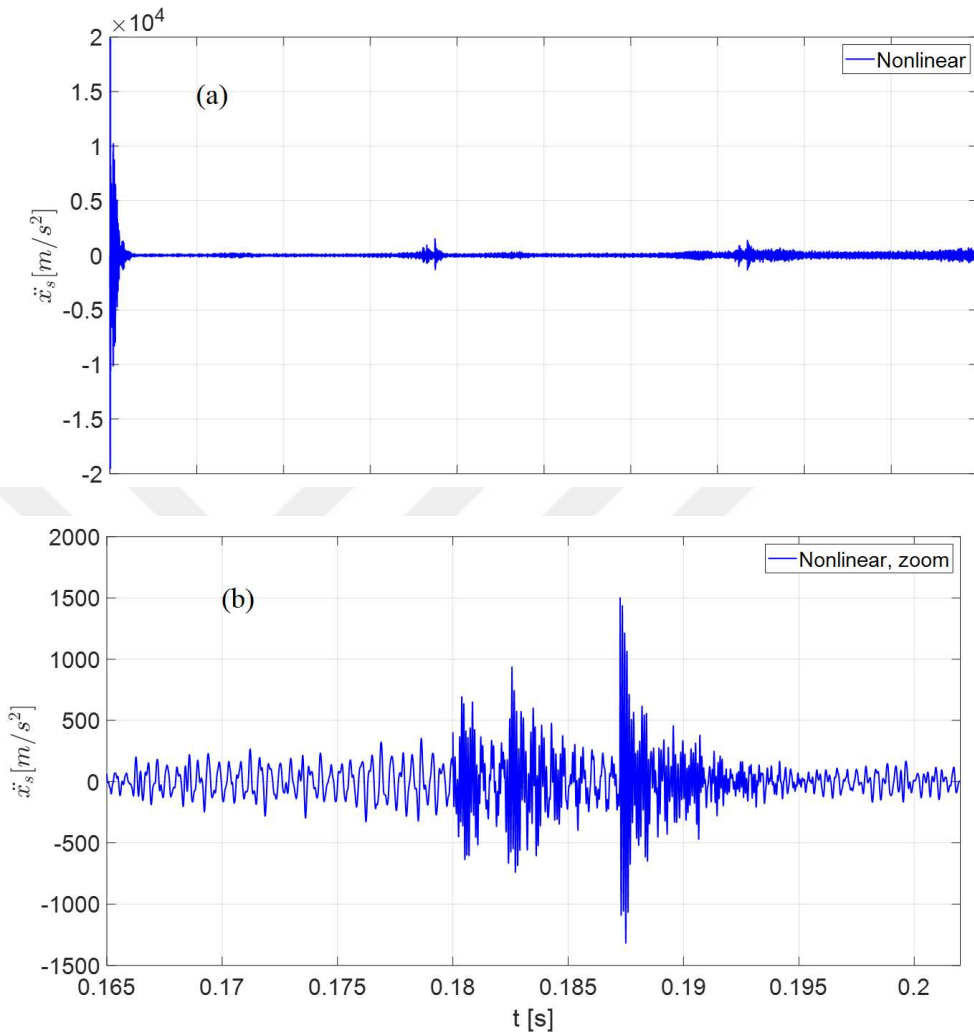


Figure 3.71 Translational acceleration of the sun gear in x direction, healthy nonlinear system

For further analysis, the acceleration in the θ_s direction for the healthy and faulty systems are compared in the frequency domain. It is realized by the FFT analysis. As it can be noticed, from Fig 3.72, the curves overlap each other except the part at the frequency range of $[8 - 11]\text{kHz}$ with sidebands around the natural frequency located at 9.97kHz .

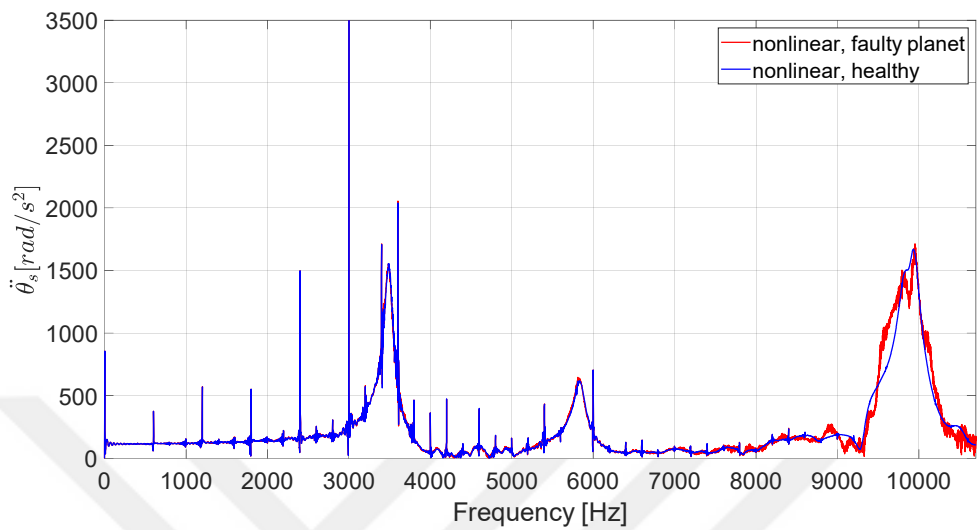


Figure 3.72 Comparison of the FFT of sun gear angular acceleration, healthy vs faulty

CHAPTER 4

Analysis of experimental data

A study is conducted on the collected gearbox acceleration datasets to process and model the signals through Fast Fourier Transform (FFT) and FS-TARMA methods.

4.1 Experimental test rig and acquired data

The experimental signals were recorded at Coventry University of the UK. Gear acceleration signals of healthy and faulty gearboxes has been collected at a sampling frequency of 51.2kHz with an accelerometer mounted on top of the ring gear. The faults considered includes planetary gear tooth surface pitting (mild and severe), broken tooth of a planet and missing tooth. Here, the pitted tooth case will be employed for the analysis and modeling. The parameters of planetary gearbox are given in table 4.1. Different faulty gears used in the experiments are shown in Fig 4.1.

Data collection process is as follows:

4.1.1 Healthy case

In healthy case, the vibration signals were collected with an accelerometer located on top of ring gear. A pitting occurred on a tooth of one of the planets after 150 hours of operation. Diameter of the pitting is 0.04mm.

4.1.2 Mild pitted case

For mild pitting, a pitting with depth of 0.04mm and width of 7mm (along tooth face in axial direction) over the face width of a planetary gear was generated.

4.1.3 Severe pitted case

In severe pitting case, the depth of fault was increased to 0.11 mm and the width was kept constant.

4.1.4 Chipped tooth case

When tooth pitting progresses due to fatigue effects, it can lead to tooth chipping. This is a severe failure and generates impulsive vibrations in the gearbox.

4.1.5 Missing tooth case

Broken tooth on a planet gear can occur under fatigue loading that leads to crack progression. It was generated by grinding the faulty tooth.

From the cases mentioned above, the pitting will be considered for further processing and diagnosis.

Table 4.1 Properties of the planetary gearbox used for data acquisition

Parameters	Sun	Planets	Carrier	Ring
No. of teeth	23	24	-	73
Pitch radius	22.85mm	23	-	149mm
Mass	309g	1816g		1224g
Pressure angle	20	20	20	20

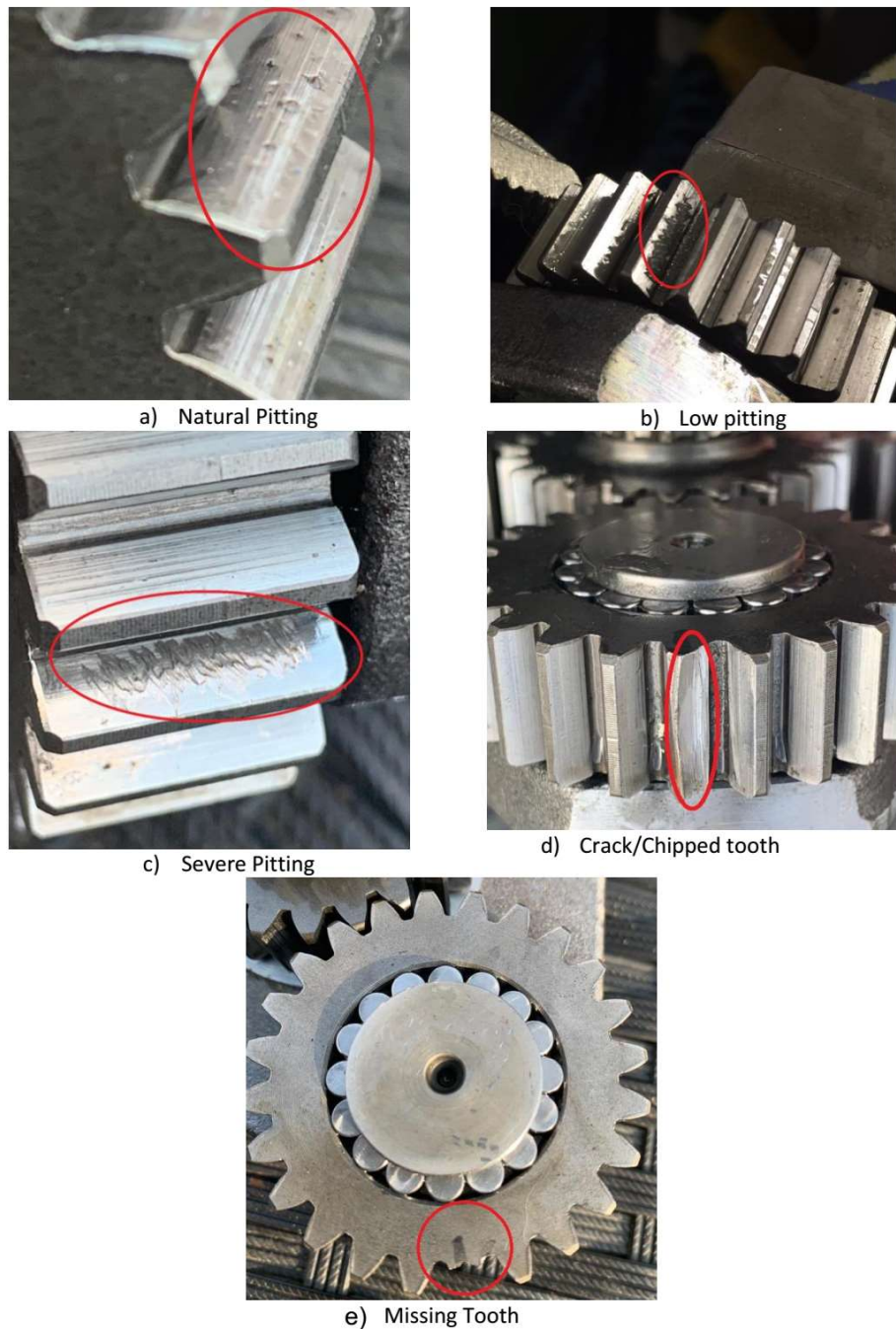


Figure 4.1 Different fault cases considered in the experimental data collection [64]

4.2 Analysis of gear vibration signals

In this section, as a preliminary analysis the recorded gear signals are transformed to frequency domain by FFT with the purpose that the faults are detected before modeling with time series models.

4.2.1 Spectral analysis of planetary gear data by FFT

The recorded vibration signal for mild pitted planet gearbox is shown in Fig 4.2. Before processing the signals, they were digitally band-pass filtered by a Butterworth filter in the range of 10Hz – 10kHz. Subsequently, a Time Synchronous Averaging (TSA) method applied on the filtered signals averages out the effects related with gears other than that of interest. By applying TSA, in fact the periodic signals are extracted from a composite signal contaminated with noise and other effects. This process is carried out synchronously taking into account the speed of the carrier. The spectrum of healthy gears is generally dominated by major peaks at gear mesh frequency and its harmonics with modulation sidebands of low order that are mostly due to gear errors [54]. For a faulty gear, a repeating impulse with low energy level will be included in the signal causing frequency modulation (FM) and Amplitude Modulation (AM). This leads to high order modulation sidebands in the spectrum of the faulty gear. Although the impulsive effect of fault has low energy distributed in a wide frequency range, it can generate structural resonances in the gearbox. Shaft high resonance frequencies may appear in the spectrum of faulty gear together with sharp peaks related to mesh frequency and its harmonics.

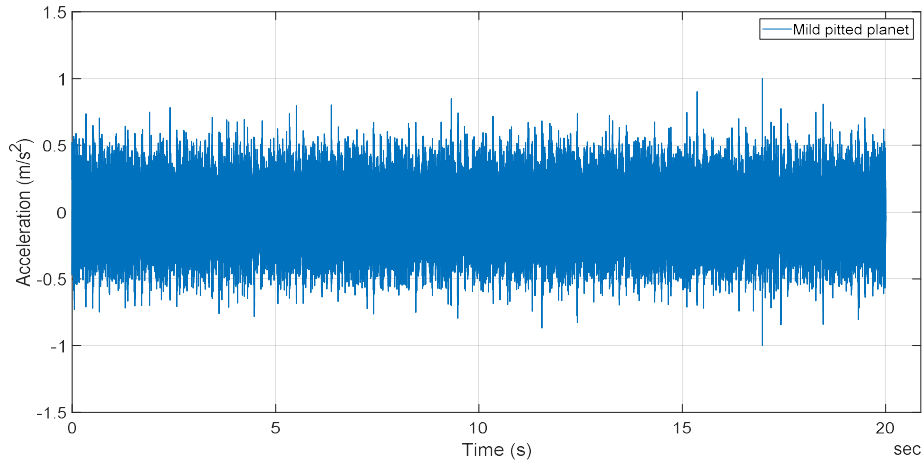


Figure 4.2 Vibrations measured on top of ring gear, low-pitted planet

For the frequency domain analysis, FFT is applied on TSA signals to detect characteristic frequencies of the healthy gearbox. The main one is the mesh frequency, f_m which is equal to 438.09Hz. Table 4.2, lists the frequencies of main components of the gearbox.

Table 4.2 Frequencies of different components of the planetary gearbox

Gear	Frequency (Hz)
Sun	23.33
Planet	17
Carrier	6
Ring	Fixed

Fig 4.2 shows the frequency spectrum of healthy gearbox vibration obtained by applying FFT on TSA signal. Gear mesh frequency and its harmonics can be identified on the chart. Due to uneven loading of the gearbox, other frequencies are resonated as well that resulted in some other large peaks. These peaks do not correspond to characteristic frequencies of the gearbox that are under consideration

here. Fig 4.3 illustrates the frequency spectrum of pitted gearbox with characteristic sidebands emerging around mesh frequency harmonics.

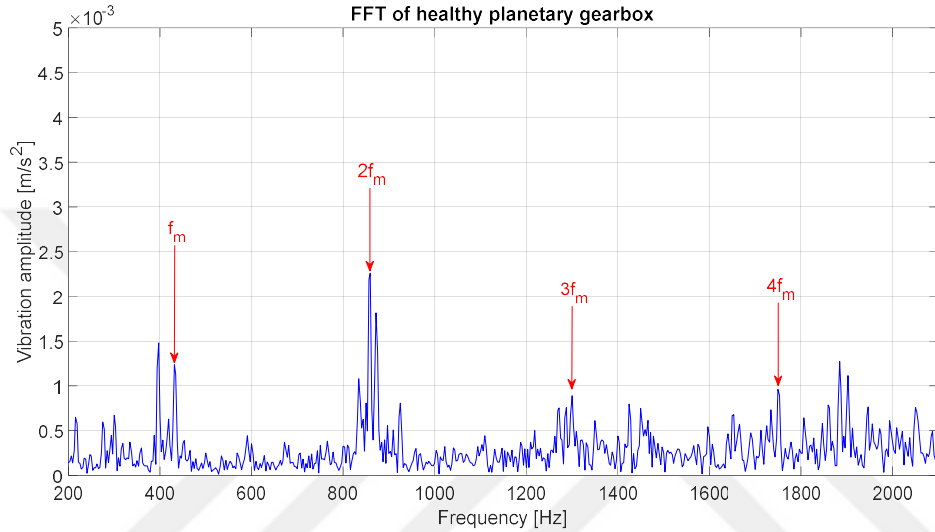


Figure 4.3 FFT of vibration signals measured on top of ring gear, healthy case

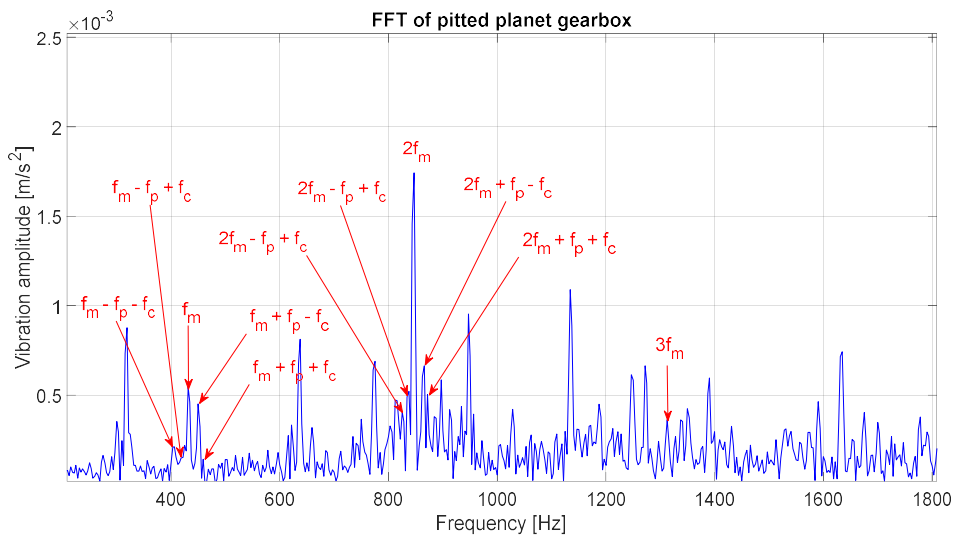


Figure 4.4 FFT of vibration signals measured on top of ring gear, pitted case

CHAPTER 5

Fault detection process based on FS-TAR, FS-TARMA and AR metric

5.1 Modeling non-stationary signals and novelty detection

Before modeling the signals, a synchronous averaging using the speed of carrier has to be carried out. This allows for removing the effects related with components other than planet frequencies and noise. In fact, the gear signals are intrinsically non-stationary and although with an assumption of weak non-stationarity they can be modeled with stationary time series models, there always exist drawbacks with the latter models. Here a class of non-stationary time series models named FS-TARMA is adopted.

5.1.1 Estimation of non-stationary time series via FS-TARMA models

The differential equation governing the motion of a continuous-time, lumped parameter, linear time variant (TV) structure denoted by φ , is as follows [41]:

$$\varphi: \mathbf{M}(t)\ddot{\mathbf{x}}(t) + \mathbf{C}(t)\dot{\mathbf{x}}(t) + \mathbf{K}(t)\mathbf{x}(t) = \mathbf{f}(t), \quad t \in [t_0, t_f], \quad (5.1)$$

where $\mathbf{x}(t) \triangleq [x_1(t) x_1(t) \dots x_p(t)]^T$ represents the vibration vector as a function of analog time t , and $\mathbf{f}(t)$ denotes the excitation vector. $[t_0, t_f]$ is the time interval at which the response is observed, and $\mathbf{M}(t)$, $\mathbf{C}(t)$ and $\mathbf{K}(t)$ denote the time-dependent mass, viscous damping, and stiffness matrices, respectively.

There exists a second order difference equation equivalent to equation (5.1). Assuming a single input, single output (SISO) system, its (partial) dynamics can be

described with a scalar difference equation given below:

$$x[t] + \sum_{i=1}^{n_a} a_i[t]x[t-i] = w[t] + \sum_{i=0}^{n_c} c_i[t]f[t-i], \quad t=1, \dots, N, \quad (5.2)$$

where t , $x[t]$, and $f[t]$ denote normalized discrete time, discretized vibration response, and force, respectively. $a_i[t]$ and $c_i[t]$ represent the discrete time TV parameters, n_a , n_c and N represent the equation Autoregressive (AR) and Moving Average (MA) orders and the length of the time signal, respectively. In case for the system to be modelled, the input is not measurable or observable, FS-TARMA model that solely depends on response can be adopted.

Here, only the major equations are given and for details, the reader is advised to refer to [49]. Equation (5.3), represents an FS-TARMA $(n_a, n_c)_{[p_a, p_c, p_s]}$ [41]:

$$x[t] + \sum_{i=1}^{n_a} a_i[t]x[t-i] = w[t] + \sum_{i=1}^{n_c} c_i[t]w[t-i], \quad w[t] \sim \text{NID}(0, \sigma_w^2[t]), \quad t=1, \dots, N, \quad (5.3)$$

where p_a , p_c represent functional basis dimensionalities respectively, and p_s denotes the dimensionality of the associated innovations variance. NID stands for Normally Independently Distributed random variables with the indicated mean and variance. $x[t]$ and $w[t]$ are the estimated non-stationary response and innovations sequence respectively. The latter has a zero mean and time-dependent variance designated by $\sigma_w^2[t]$. $a_i[t]$ and $c_i[t]$ coefficients represent time-dependent AR and MA parameters, respectively. To estimate these parameters as well as innovations variance $\sigma_w^2[t]$, functional subspaces formed by orthogonal independent functions are utilized given as follows [41]

$$\begin{aligned} \mathcal{F}_{AR} &\triangleq \{G_{b_a(1)}[t], G_{b_a(2)}[t], \dots, G_{b_a(p_a)}[t]\}, \\ \mathcal{F}_{MA} &\triangleq \{G_{b_c(1)}[t], G_{b_c(2)}[t], \dots, G_{b_c(p_c)}[t]\}, \\ \mathcal{F}_{\sigma_w^2} &\triangleq \{G_{b_s(1)}[t], G_{b_s(2)}[t], \dots, G_{b_s(p_s)}[t]\}. \end{aligned} \quad (5.4)$$

where “ \mathcal{F} ” represents functional subspace of the associated quantity and

$\{G_j[t]: j = 0, 1, \dots\}$ indicates a set of orthogonal basis functions that can be selected from a suitable family such as Sine and Cosine functions, Chebyshev functions, etc. The indices $b_a(i)(i=1, \dots, p_a)$, $b_c(i)(i=1, \dots, p_c)$ and $b_s(i)(i=1, \dots, p_s)$, indicate the specific basis functions from a family selected for the associated subspace.

The time-dependent parameters and innovations variance are estimated using the associated functional subspace, as follows:

$$a_i[t] \triangleq \sum_{j=1}^{p_a} a_{i,j} G_{b_a(j)}[t], \quad c_i[t] \triangleq \sum_{j=1}^{p_c} c_{i,j} G_{b_c(j)}[t], \quad \sigma_w^2[t] \triangleq \sum_{j=1}^{p_s} s_j G_{b_s(j)}[t], \quad (5.5)$$

where $a_{i,j}$, $c_{i,j}$ and s_j represent the AR, MA and innovations variance coefficients of projection, respectively. In such manner, the parameterization of FS-TARMA model is realized in terms of constant projection coefficients $a_{i,j}$, $c_{i,j}$ and s_j .

Consequently, a particular model structure \mathcal{M} , identified by model orders n_a , n_c , and functional subspaces \mathcal{F}_{AR} , \mathcal{F}_{MA} , $\mathcal{F}_{\sigma_w^2}$, is defined as follows [41]:

$$\mathcal{M} \triangleq \{n_a, n_c, \mathcal{F}_{AR}, \mathcal{F}_{MA}, \mathcal{F}_{\sigma_w^2}\}. \quad (5.6)$$

Eventually, the model identification problem can be represented as follows [41]: “Given N vibration response measurements, $x^N = \{x[1] \dots x[N]\}$, and the FS-TARMA model set:

$$\begin{aligned} M &\triangleq \\ &\left\{ \mathcal{M}(\theta) : x[t] + \sum_{i=1}^{n_a} a_i[t, \theta] x[t-i] = e[t, \theta] + \sum_{i=1}^{n_c} c_i[t, \theta] e[t-i]; \sigma_w^2 = E\{e^2[t, \theta]\}, t = 1, \dots, N, \theta \in \Re^{\dim(\theta)} \right\}, \end{aligned} \quad (5.7)$$

select an element of M which best fits the observations”. In this equation, $\dim(\theta)$ represents the dimension of the parameter vector, and $e[t, \theta]$ denotes the one-step-ahead prediction error (residual) sequence of the model.

The identification problem is comprised of two subproblems:

- Estimation of parameters assuming a given structure \mathcal{M} ,
- Selection of model structure

The subproblem (a) is discussed in the subsequent subsection.

5.1.1.1 Estimation of FS-TARMA parameters

The vector θ , which includes the projection AR and MA projection coefficients denoted by a and c , and innovations variance s expressed in equation (5.8) for a given model \mathcal{M} , using measured non-stationary response x^N is considered in this subsection [41]

$$\begin{aligned}\theta &\triangleq [\vartheta^T \mid s^T]_{(n_a p_a + n_c p_c + p_s) \times 1}, \vartheta \triangleq [a^T \mid c^T]_{(n_a p_a + n_c p_c) \times 1}, s \triangleq [s_1, \dots, s_{p_s}]_{p_s \times 1}, \\ a &\triangleq [a_{1,1}, \dots, a_{1,p_a} \mid \dots \mid a_{n_a,1}, \dots, a_{n_a,p_a}]^T_{(n_a p_a) \times 1}, \\ c &\triangleq [c_{1,1}, \dots, c_{1,p_c} \mid \dots \mid c_{n_c,1}, \dots, c_{n_c,p_c}]^T_{(n_c p_c) \times 1}\end{aligned}\quad (5.8)$$

To estimate the AR/MA projection coefficients vector ϑ , Ordinary Least Squares (OLS) method is employed which sums up the squares of the one step ahead prediction errors of the model as follows

$$\hat{\vartheta} = \arg \min_{\vartheta} \sum_{t=1}^N e^2[t, \vartheta], \quad (5.9)$$

where $\arg \min$ indicates “argument minimizing” which means that the minimizing arguments are searched for, and $e[t, \vartheta]$ denotes the one-step-ahead prediction error. Since the estimation of FS-TARMA parameters results in a non-linear problem, it can be solved by an iterative method that divides the main non-linear problem into linear subproblems. Here, the Two Stage Least Squares (2SLS) method [41], is utilized for the estimation of model parameters.

5.1.1.2 FS-TARMA modal parameters

Once an FS-TARMA models is estimated, the time-dependent modal parameters of the model, which are natural frequencies $\omega_n[t]$ and damping ratios $\varsigma_i[t]$ can be obtained as follows [41]

$$\omega_n[t] = \frac{|\ln \lambda_i[t]|}{T_s} (\text{rad / s}), \quad \varsigma_i[t] = -\cos(\arg(\ln \lambda_i[t])), \quad t = 1, \dots, N, \quad (5.10)$$

where $\lambda_i[t]$ denotes the i^{th} pole of the model at time t , and T_s represents the sampling period.

5.1.2 Estimation of nonstationary time series via FS-TAR models

There exists a second order difference equation equivalent to equation (5.11). Assuming a single input, single output (SISO) system, its (partial) dynamics can be described with a scalar difference equation given below:

$$x[t] + \sum_{i=1}^{n_a} a_i[t]x[t-i] = w[t], \quad t = 1, \dots, N \quad (5.11)$$

where t and $x[t]$, denote normalized discrete time, discretized vibration response, respectively. $a_i[t]$ represent the discrete time TV parameters, n_a and N represent the equation Autoregressive (AR) order and the length of the time signal, respectively. In case for the system to be modelled, the input is not measurable or observable, FS-TAR model that solely depends on response can be adopted.

Here, only the major equations are given and for details, the reader is advised to refer to [39]. Equation (3), represents an FS-TAR $(n_a)_{[p_a, p_s]}$ [39]:

$$x[t] + \sum_{i=1}^{n_a} a_i[t]x[t-i] = w[t], \quad w[t] \sim \text{NID}(0, \sigma_w^2[t]), \quad t = 1, \dots, N, \quad (5.12)$$

where p_a represent functional basis dimensionality, and p_s denotes the dimensionality of the associated innovations variance. NID stands for Normally Independently Distributed random variables with the indicated mean and variance. $x[t]$ and $w[t]$ are the estimated non-stationary response and innovations sequence respectively. The latter has a zero mean and time-dependent variance designated by $\sigma_w^2[t]$ and $a_i[t]$ coefficients represent time-dependent AR parameters. To estimate these parameters as well as innovations variance $\sigma_w^2[t]$, functional subspaces formed by orthogonal independent functions are utilized given as follows;

$$\mathcal{F}_{AR} \triangleq \{G_{b_a(1)}[t], G_{b_a(2)}[t], \dots, G_{b_a(p_a)}[t]\}, \quad (5.13)$$

$$\mathcal{F}_{\sigma_w^2} \triangleq \{G_{b_s(1)}[t], G_{b_s(2)}[t], \dots, G_{b_s(p_s)}[t]\}.$$

where “ \mathcal{F} ” represents functional subspace of the associated quantity and $\{G_j[t]: j = 0, 1, \dots\}$ indicates a set of orthogonal basis functions that can be selected from a suitable family such as Sine and Cosine functions, Chebyshev functions, etc. The indices $b_a(i)(i=1, \dots, p_a)$, and $b_s(i)(i=1, \dots, p_s)$, indicate the specific basis functions from a family selected for the associated subspace.

The time-dependent parameters and innovations variance are estimated using the associated functional subspace, as follows:

$$a_i[t] \triangleq \sum_{j=1}^{p_a} a_{i,j} G_{b_a(j)}[t], \quad \sigma_w^2[t] \triangleq \sum_{j=1}^{p_s} s_j G_{b_s(j)}[t] \quad (5.14)$$

where $a_{i,j}$ and s_j represent the AR and innovations variance coefficients of projection, respectively. In such manner, the parameterization of FS-TAR model is realized in terms of constant projection coefficients $a_{i,j}$ and s_j . Consequently, a particular model structure M , identified by model order n_a , and functional subspaces $\mathcal{F}_{AR}, \mathcal{F}_{\sigma_w^2}$, is defined as follows:

$$M \triangleq \{n_a, \mathcal{F}_{AR}, \mathcal{F}_{\sigma_w^2}\} \quad (5.15)$$

Eventually, the model identification problem can be represented as follows: “Given N vibration response measurements, $x^N = \{x[1] \dots x[N]\}$, and the FS-TAR model set:

$$M \triangleq \left\{ M(\theta) : x[t] + \sum_{i=1}^{n_a} a_i[t, \theta] x[t-i] = e[t, \theta]; \quad \sigma_w^2 = E\{e^2[t, \theta]\}, \quad t = 1, \dots, N, \quad \theta \in \mathbb{R}^{\dim(\theta)} \right\} \quad (5.16)$$

select an element of M which best fits the observations”. In this equation, $\dim(\theta)$ represents the dimension of the parameter vector, and $e[t, \theta]$ denotes the one-step-ahead prediction error (residual) sequence of the model.

The identification problem is comprised of two subproblems:

- Estimation of parameters assuming a given structure M ,
- Selection of model structure

The subproblem (a) is discussed in the subsequent subsection.

5.1.2.1 Estimation of FS-TAR parameters

The vector θ , which includes the AR projection coefficients denoted by a , and innovations variance s expressed in equation (8) for a given model M, using measured non-stationary response x^N is considered in this subsection

$$\begin{aligned}\theta &\triangleq [\vartheta^T | s^T]_{(n_a p_a + p_s) \times 1}, \vartheta \triangleq [a^T]_{(n_a p_a) \times 1}, s \triangleq [s_1, \dots, s_{p_s}]_{p_s \times 1}, \\ a &\triangleq [a_{1,1}, \dots, a_{1,p_a} | \dots | a_{n_a,1}, \dots, a_{n_a,p_a}]^T_{(n_a p_a) \times 1},\end{aligned}\quad (5.17)$$

To estimate the AR projection coefficients vector ϑ , Ordinary Least Squares (OLS) method is employed which sums up the squares of the one step ahead prediction errors of the model as follows

$$\hat{\vartheta} = \arg \min_{\vartheta} \sum_{t=1}^N e^2[t, \vartheta], \quad (5.18)$$

where $\arg \min$ indicates “argument minimizing” which means that the minimizing arguments are searched for, and $e[t, \vartheta]$ denotes the one-step-ahead prediction error.

5.1.2.2 Selection of AR order and functional subspace dimension

To select the AR order of the FS-TAR model and the associated functional subspace the following process is implemented:

- I. BIC values are calculated for different values of n_a and p_a . Subsequently the model with the largest negative BIC value is selected. When BIC values are negative, the model with the largest negative value is selected as the best-fitted one. The order selection process is based on the minimization of BIC by trial-and-error process through the BIC equation for the FS-TAR model given as [41]

$$BIC = \frac{1}{N} \sum_{t=1}^N \left(\ln(\mathbf{g}_s^T[t] \mathbf{s}) + \frac{e^2[t, \hat{\mathbf{a}}]}{(\mathbf{g}_s^T[t] \mathbf{s})^2} \right) + \dim(\hat{\mathbf{a}}) \frac{\ln N}{N} \quad (5.19)$$

where $\mathbf{g}_s[t] \triangleq [G_{b_s(1)}[t] \ G_{b_s(2)}[t] \ \dots \ G_{b_s(p_s)}[t]]^T$,

$$\mathbf{s} \triangleq [s_1, \dots, s_{p_s}]_{p_s \times 1}, \hat{\mathbf{a}} \triangleq [a_{1,1}, \dots, a_{1,p_a} \ | \ \dots \ | \ a_{n_a,1}, \dots, a_{n_a,p_a}]_{(n_a p_a) \times 1}.$$

II. A subsequent optimization of the functional space obtained in stage I is carried out to remove the redundant basis functions. In this process, the effect of removing each basis function on the functional subspace to adequately estimate the model parameters without a significant reduction in projection accuracy is examined. Such a reduction is realized through Aggregate Parameter Deviation (APD) criterion given as follows [41]

$$APD \triangleq \sum_{k=1}^{n_a} \Delta a_k + \Delta s, \quad (5.20)$$

$$\Delta a_k = \frac{\sum_{t=1}^N |a_k^{in}[t] - a_k^c[t]|}{\sum_{t=1}^N a_k^{in}[t]}, \Delta s \triangleq \frac{\sum_{t=1}^N |\sigma_{ek}^{2,in}[t] - \sigma_{ek}^{2,c}[t]|}{\sum_{t=1}^N \sigma_{ek}^{2,in}[t]} \quad (5.21)$$

Where Δa_k and Δs represent deviations of AR and innovations variance trajectories, respectively. The superscript “*c*” and “*in*” denotes the current and initial (extended) value of the associated parameters, respectively. For more details of the process, the reader is referred to [41], where the problem is solved for an FS-TARMA model.

Once an FS-TAR model is estimated, the time-dependent modal parameters of the model, which are natural frequencies $\omega_{ni}[t]$ and damping ratios $\zeta_i[t]$ can be obtained in the same way as it was done for FS-TARMA.

5.1.3 AR metric for the comparison of time series models and novelty detection

Once the FS-TARMA models associated with faulty and healthy signals are estimated,

they must be compared to achieve a criterion for fault detection. The comparison of models can be carried out utilizing a variety of methods. Here, a metric called AR metric [65] is considered.

To start with, given $X_t \in L$ and $Y_t \in L$ as invertible processes whose forecast functions expressed via the corresponding AR coefficients as [65]

$$\pi_x = (\pi_{1,x}, \pi_{2,x}, \dots, \pi_{j,x}, \dots), \quad \pi_y = (\pi_{1,y}, \pi_{2,y}, \dots, \pi_{j,y}, \dots) \quad (5.22)$$

And assuming absolute convergence of π sequences in L , Piccolo [65], introduced a metric between two AutoRegressive Integrated Moving Average (ARIMA) processes X_t and Y_t , with given orders, as Euclidean distance between their corresponding coefficients of the AR(∞) formulation denoted as follows

$$d(X_t, Y_t) = \left[(\pi_x - \pi_y)' (\pi_x - \pi_y) \right]^{\frac{1}{2}} = \sqrt{\sum_{j=1}^{\infty} (\pi_{j,x} - \pi_{j,y})^2}. \quad (5.23)$$

The expression given in equation (11) has the properties of a metric as for any two identical processes, their corresponding distance is zero. This metric has another important feature and it is: although different orders for the model structures can be obtained for modelling the same set of signals, their corresponding distance is zero since they are supposed to provide the same predictions.

It has to be mentioned that for processes $X_t \in L$ and $Y_t \in L$, their associated distance $d(X_t, Y_t)$ is always well defined regardless of the fact that one or both processes are stationary or non-stationary. This property of AR metric, makes it a reliable candidate for the comparison of time series models regardless from the stationarity or non-stationarity of the models.



CHAPTER 6

Time-frequency analysis of gear vibration signals by FS-TAR and Wavelet Transform

In this chapter, time dependent frequency analysis of the vibration signals will be carried out via WT and the FS-TAR approach. Firstly, the necessary equations will be given and subsequently the results will be presented.

6.1 Time-frequency analysis of gear vibration signals by Wavelet Transform

Since a planetary gearbox's vibrations are nonstationary, conventional FFT analysis, although compelling, may not be well suited for analyzing its time-varying (TV) frequency spectrum. A variety of methods are available for the time-frequency analysis of nonstationary signals. Continuous wavelet transform (CWT) features several advantages over windowed FFT. One important feature is that time resolution is high at a higher frequency, unlike the windowed FFT, where time and frequency resolutions are independent.

Wavelet analysis was first introduced to analyze seismic signals in the 1980s. Based on the purpose of analysis, two main types of Discrete Wavelet Transform (DWT) and Continuous Wavelet Transform (CWT) can be utilized. While the first is generally employed for noise removal, the latter is preferred for time-frequency analysis. For the case of time-frequency analysis, the wavelet analysis can be considered as FFT analysis with windows of variable lengths. Therefore, they can focus on frequency or time domains to provide local information in both domains. Wavelets can be 1D or multi-dimensional. 1D wavelets can be expressed as [66]

$$\psi^{(a,b)}(x) = \frac{1}{\sqrt{|a|}} \psi\left(\frac{x-b}{a}\right) \quad (6.1)$$

where $a(\neq 0)$, b real parameters and $\psi(x)$ represents a spatially localized function named “mother wavelet”. Wavelet analysis, decomposes a given function into a combination of wavelets and reconstructs it. For the reconstruction to be optimal, the mother wavelet should satisfy some conditions. For the case of CWT, the following admissibility condition must be satisfied [66]

$$C_\psi \equiv \int_{-\infty}^{+\infty} \frac{|\hat{\psi}(\omega)|^2}{|\omega|} d\omega < \infty \quad (6.2)$$

where $\hat{\psi}(\omega)$ represents the Fourier transform of $\psi(x)$ given by

$$\hat{\psi}(\omega) = \int_{-\infty}^{+\infty} e^{-i\omega x} \psi(x) dx \quad (6.3)$$

The CWT and inverse CWT of a function $f(x) \in L^2(\mathbb{R})$ is expressed as [66]

$$T_\psi(a, b) = \frac{1}{\sqrt{C_\psi}} \int_{-\infty}^{+\infty} \bar{\psi}^{(a,b)}(x) f(x) dx \quad (6.4)$$

$$f(x) = \frac{1}{\sqrt{C_\psi}} \int_{-\infty}^{+\infty} \int_{-\infty}^{+\infty} T_\psi(a, b) \psi^{(a,b)}(x) \frac{da db}{a^2}$$

The dimension of the time-frequency space to which the wavelet expands a given function is twice the dimension of the original signal. This allows for effortless multiscale analysis and identification of fault effects in the signal.

6.2 Time-frequency analysis of gear vibration signals by FS-TAR model

Although CWT provides valuable information about the TV properties of the signals by a time-frequency analysis, it does not have a parametric structure. Nonstationary time series models provide a parametrized representation of TV system dynamics,

generating nonstationary vibration response. Time-dependent power spectral density (PSD) of nonstationary gear vibration signals can be obtained by estimated FS-TAR models via

$$S(\omega, t) = \frac{1}{\left| 1 + \sum_{r=1}^{n_a} a_r[t] e^{-j\omega r/f_s} \right|} \sigma_e^2[t], \quad t = 1, \dots, N \quad (6.5)$$

where time dependent AR coefficients $a_r[t]$ and innovations variance $\sigma_e^2[t]$ are plugged in from the estimated FS-TAR model and f_s is sampling frequency.

FFT analysis is an efficient tool to detect and identify fault types in a planetary gearbox. However, gear vibration signals are nonstationary, and FFT analysis of TSA signals assumes that they are stationary, leading to a frozen time FFT for an averaged signal. A more efficient spectral analysis can be realized through a time-frequency analysis. Various methods are available for this purpose. One of the powerful methods is Continuous Wavelet Transform (CWT) which will be applied to vibration signals in the next section. Furthermore, the estimated FS-TAR models will analyze the time-dependent Power Spectral Density (PSD) of the signals.

6.3 Continuous Wavelet Transform of vibration signals

Power Spectral Density (PSD) analysis of gear vibration signals via FS-TAR model and CWT analysis can provide a deep insight into the time-dependent effects of gear fault on nonstationary response and simultaneous fault influence mechanism in time and frequency domains.

The CWT analysis of gear vibration signals is performed with MATLAB software. Different wavelet family types are available for CWT. Here, the “Bump” type featuring a wider variance in time and narrower variance in frequency is chosen.

In this section, CWT is first applied on healthy and pitted gearbox signals; subsequently, PSDs are obtained by the FS-TAR model. The spectra estimated by the two approaches are compared, and their role in gear fault detection is studied.

Fig 6.1 depicts the PSD of healthy gearbox vibration calculated in [10 12000] Hz frequency band. Multiple harmonics of mesh frequency are excited with their peaks, dominant in the PSD. These harmonics range from the 7th to 22nd multiples. However, it is cumbersome to discriminate between the harmonics and the adjacent peaks associated with other frequencies resonated with them. The crucial of the graph is the frequency range [3 10] kHz excited during the gearbox's operation. For the case of pitted planetary gear, the CWT of the vibration signal is depicted in Fig 6.2. A clear distinction can be made between the frequency range of fault influence compared with the CWT of the healthy gearbox of Fig 6.1. In this case, the range of excited frequencies with dominant peaks has shifted to [1 3] kHz with intermittent peaks corresponding to faulty planet mesh with ring or sun gear. This frequency range includes harmonics 2 to 8 of gear mesh frequency. However, it does not imply that the other gear mesh frequencies do not exist in the spectrum. In Fig 6.2-b, a 2D view of the CWT, dominant peaks are detectable with bright yellow color. A detailed FFT analysis in the previous section detected a concentrated planet gear fault. A comparison of graphs presented in Figs 6.1 and 6.2 reveals a change in the gearbox dynamics. Since the peaks are narrow in time but wide in the frequency domain, it suggests the existence of a concentrated fault that influences the vibration response similar to an impulse. Fusion of the information provided by FFT and CWT analysis can lead to a more robust fault type identification.

6.4 FS-TAR model-based PSD

Although the investigation of PSDs estimated by CWT can aid gear fault diagnosis, its nonparametric structure does not allow for a detailed analysis of fault occurrence time and frequencies through comparison. The FS-TAR model provides a parametric estimate of the PSD of the vibration signal, which features high-frequency resolution and enables the identification of the dominant mesh frequency harmonics.

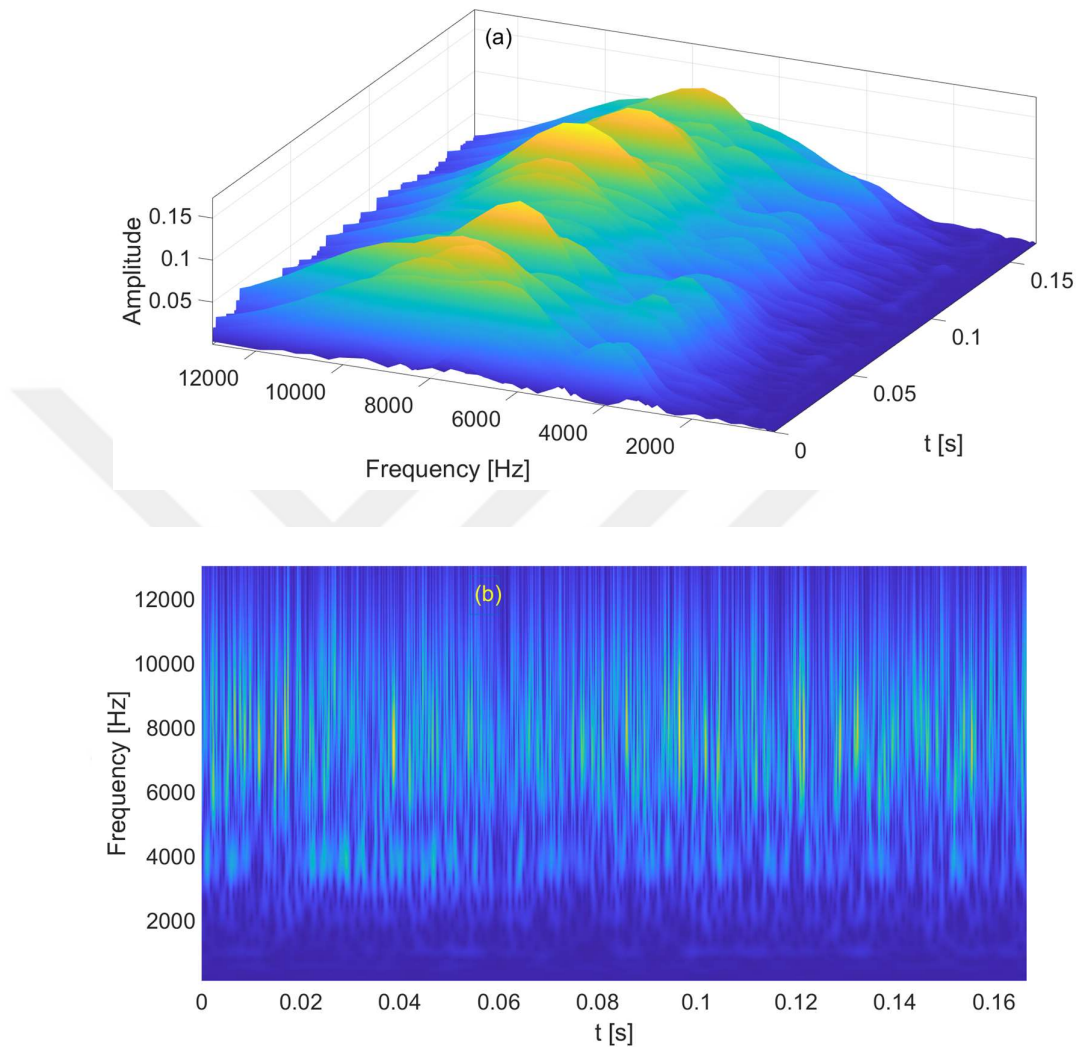


Figure 6.1 CWT graph of the healthy gearbox vibration, a) 3D view, b) 2D view

Fig 6.3 demonstrates the PSD of healthy gear vibration obtained by the FS-TAR (32)_[7, 11] model. Dominant harmonics of mesh frequency, which can be easily identified from the graph, are marked by their harmonic numbers in Fig 6.3-b. The estimated harmonics vary slightly in one revolution period of the carrier. This is because some other frequencies of the gear system in the vicinity of those harmonics are resonated.

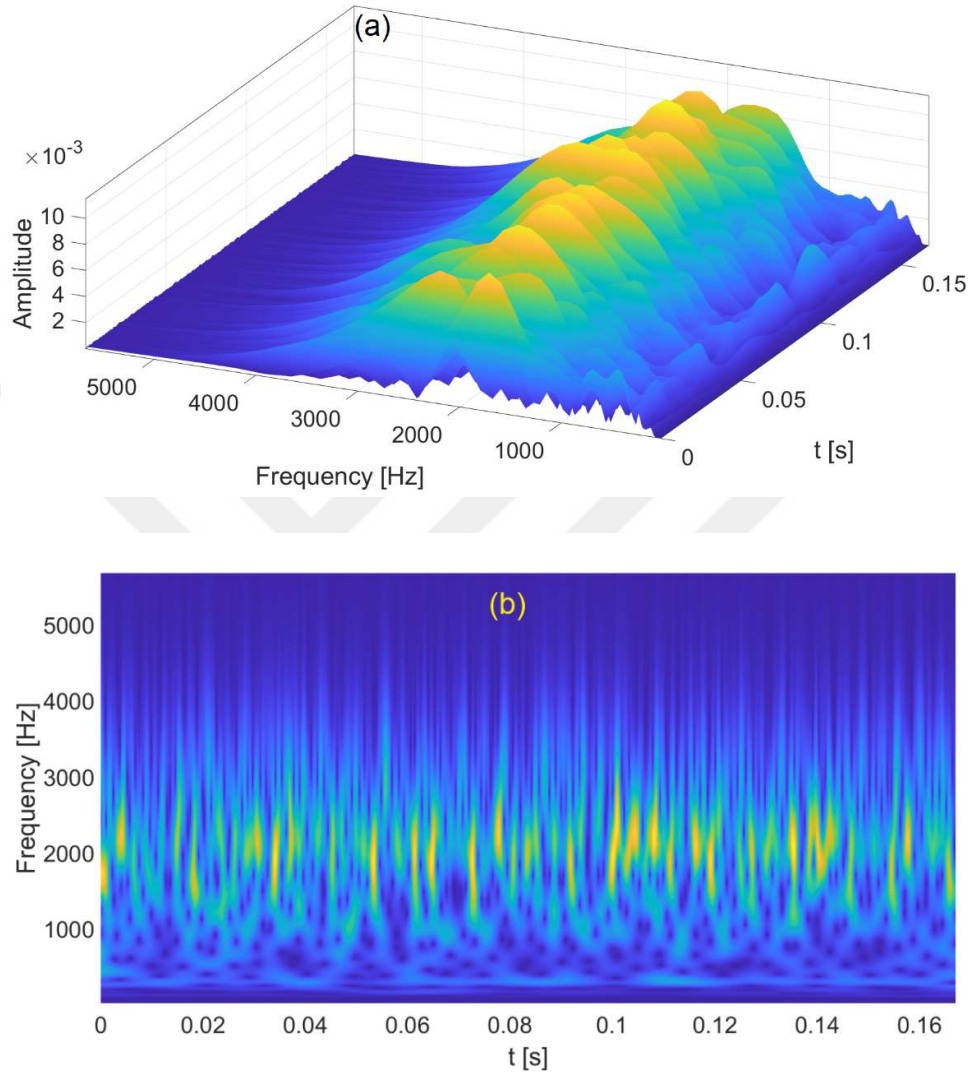


Figure 6.2 CWT graph of the pitted gearbox vibration, a) 3D view, b) 2D view

An important phenomenon evident in the graph is the consistent excitation of the identified harmonics during the gearbox operation, which implies no sudden change in the response due to a concentrated fault. To a significant degree, the signal's energy is evenly distributed between dominant harmonics. An important distinction between the PSDs estimated by CWT and FS-TAR is the number of frequencies/peaks identified. CWT does not truncate the signal by estimating it by

several frequencies as FS-TAR does. It constitutes many filters applied to the signal without changing its frequency content. FS-TAR provides a parametric signal model and operates like a filter with a given order. It is well suited for estimating signal resonances, and its autoregressive order must be chosen reasonably, which cannot be very large.

Regarding the PSD of faulty gear vibration, depicted in Fig 6.4, it can be said that the dominant peaks have been shrunk to a narrower frequency band of [1 2] kHz, although some higher harmonics are instantly excited in [3 4] kHz. Another critical phenomenon identifiable from Fig 6.4-b is the intermittent excitation of mainly the fourth and sometimes the third gear mesh frequency harmonics. It occurs due to planetary gear fault as it generates impulses at specific periods related to the sun-planet and planet-ring mesh phasing. The range of frequencies with dominant amplitudes for the PSD in Fig 6.4 and that of CWT in Fig 6.2 are approximately the same. The main difference between the two PSDs is that the former is a truncated model of the frequencies present in the vibration signal in contrast to the latter, which includes all frequencies. The PSD estimated by FS-TAR simplifies the identification of dominant frequencies. It provides a parametric structure that can be further analyzed to obtain fault-sensitive features that are used in the fault diagnosis process.

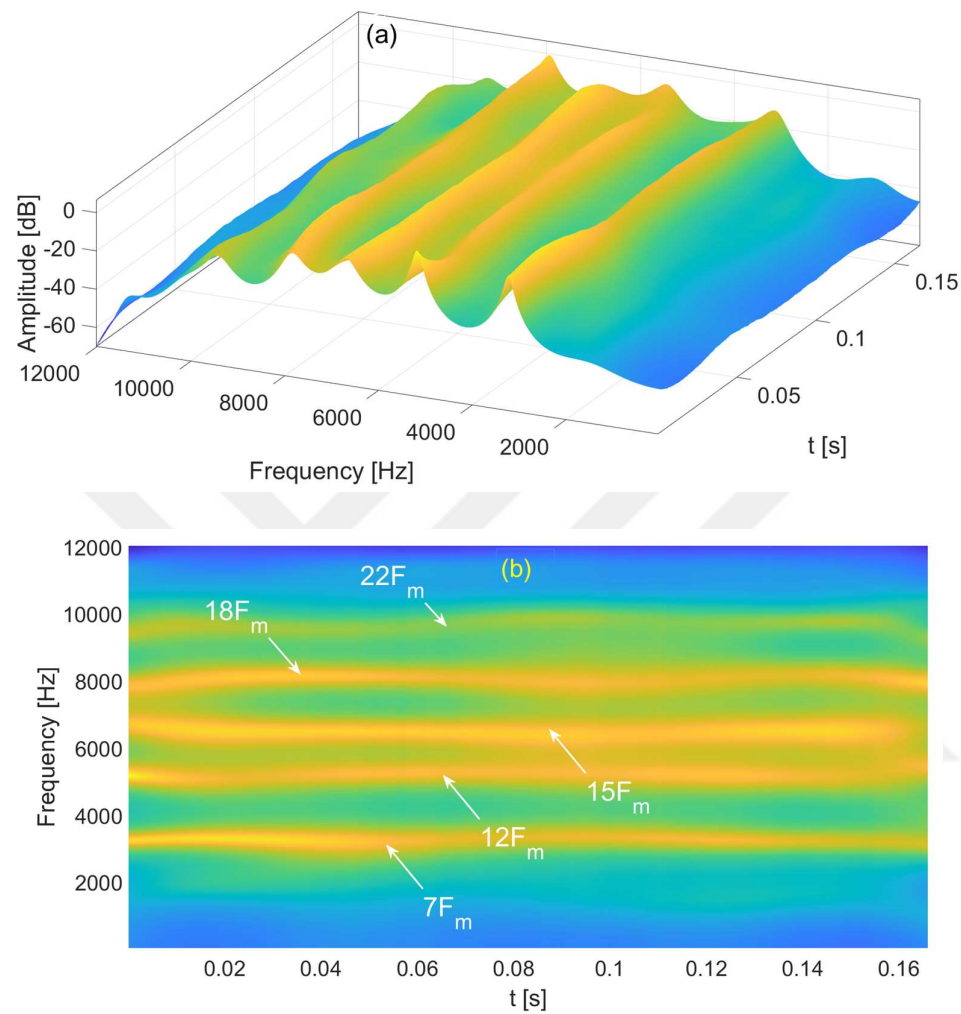


Figure 6.3 PSD estimate of the healthy gear vibration signal based on FS-TAR model

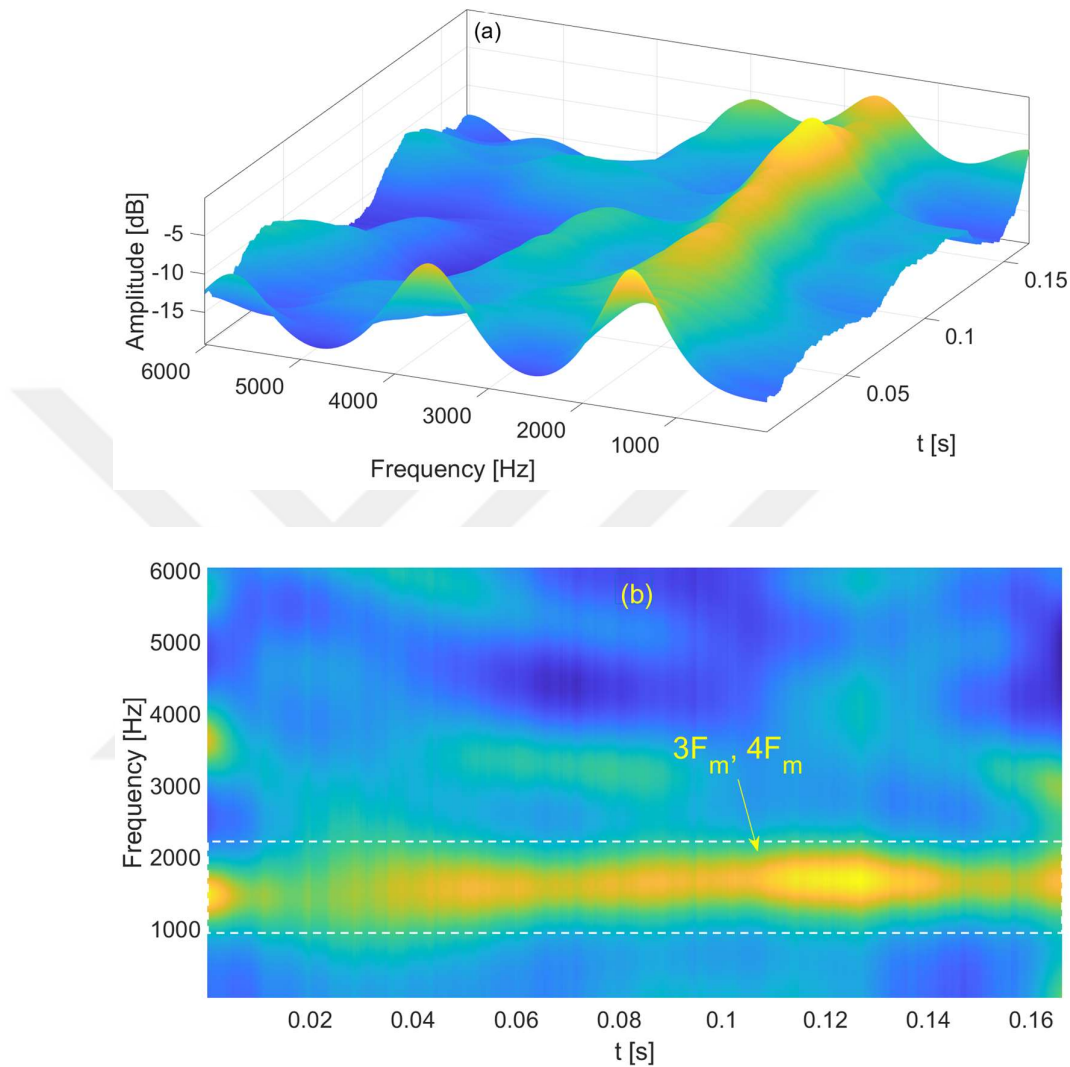


Figure 6.4 PSD estimate of the pitted gear vibration signal based on FS-TAR model (dotted lines are used for clarification only)

CHAPTER 7

Fault detection based on FS-TAR models via vibration signals: results

7.1 Modeling and estimation of gear signals via FS-TAR models

In this section, first, the predictions of the gear signals based on FS-TAR model will be discussed and then the results of fault detection will be presented.

7.1.1 FS-TAR model identification, results

Gear mesh stiffness and damping vary periodically, and so do the vibration signals. Therefore, trigonometric functions are employed as basis functions to estimate the variation of FS-TAR model parameters. Equation (7.1) presents the trigonometric functions employed in the model estimation process.

$$G_{b_0}[t] = 1, G_{b_{2j-1}}[t] = \sin\left(\frac{j\pi(t-1)}{m-1}\right), G_{b_{2j}}[t] = \cos\left(\frac{j\pi(t-1)}{m-1}\right), j = 1, 2, \dots, t = 1, 2, \dots, m. \quad (7.1)$$

The number of basis functions for an adequate model is determined during the order selection level. The order selection process for healthy and faulty data is carried out separately, as each possesses different partial dynamics. During the order selection process, the order of the model at the first trial is determined based on the gearbox dynamics observed from FFT analysis. For instance, twice the number of dominant characteristic frequencies, including mesh frequency and its harmonics, can be considered as a potential order for the model.

Once an adequate FS-TAR model is fitted to the measured data, predictions are obtained using the estimated models. In the order selection process, which will estimate the orders n_a, p_a , the model estimation process is repeated for varying orders, and the set resulting in minimum BIC is selected. The BIC values for different order sets results can be plotted as a 3D surface, as depicted in Fig 7.1. According to

the calculations, the minimum BIC is obtained for $n_a = 32, p_a = 9$. Although these values lead to the best-fit model, the expanded and complete functional subspace order is set to 13. The appropriate basis functions are selected through a subsequent refinement based on the APD criterion. As a result of this process, the final order set remains the same; however, the basis functions are changed according to the APD criterion.

Once an adequate model is estimated, the response can be predicted. FS-TAR(32)_[7,11] model-based predictions for a segment of acceleration signal measured on top of the ring gear is presented in Fig 7.2-(a). Together with the predictions, the residual series and its variance are demonstrated in Fig 7.2-(b) and 7.2-(c), respectively. The prediction accuracy is considered to be satisfactory since the error, which is calculated as the ratio of the Residual Sum of Squares to the Series Sum of Squares (RSS/SSS), is equal to 0. 1%.

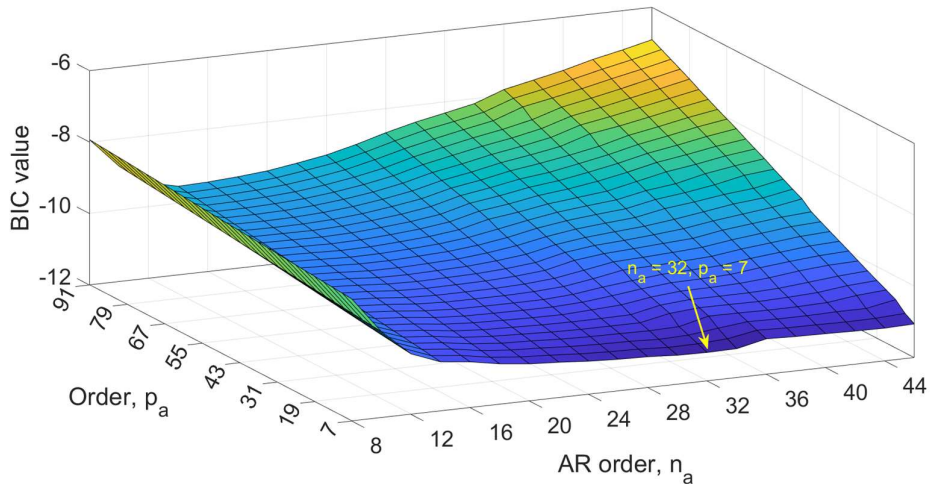


Figure 7.1 BIC values for different AR and functional basis orders plotted as a 3D surface

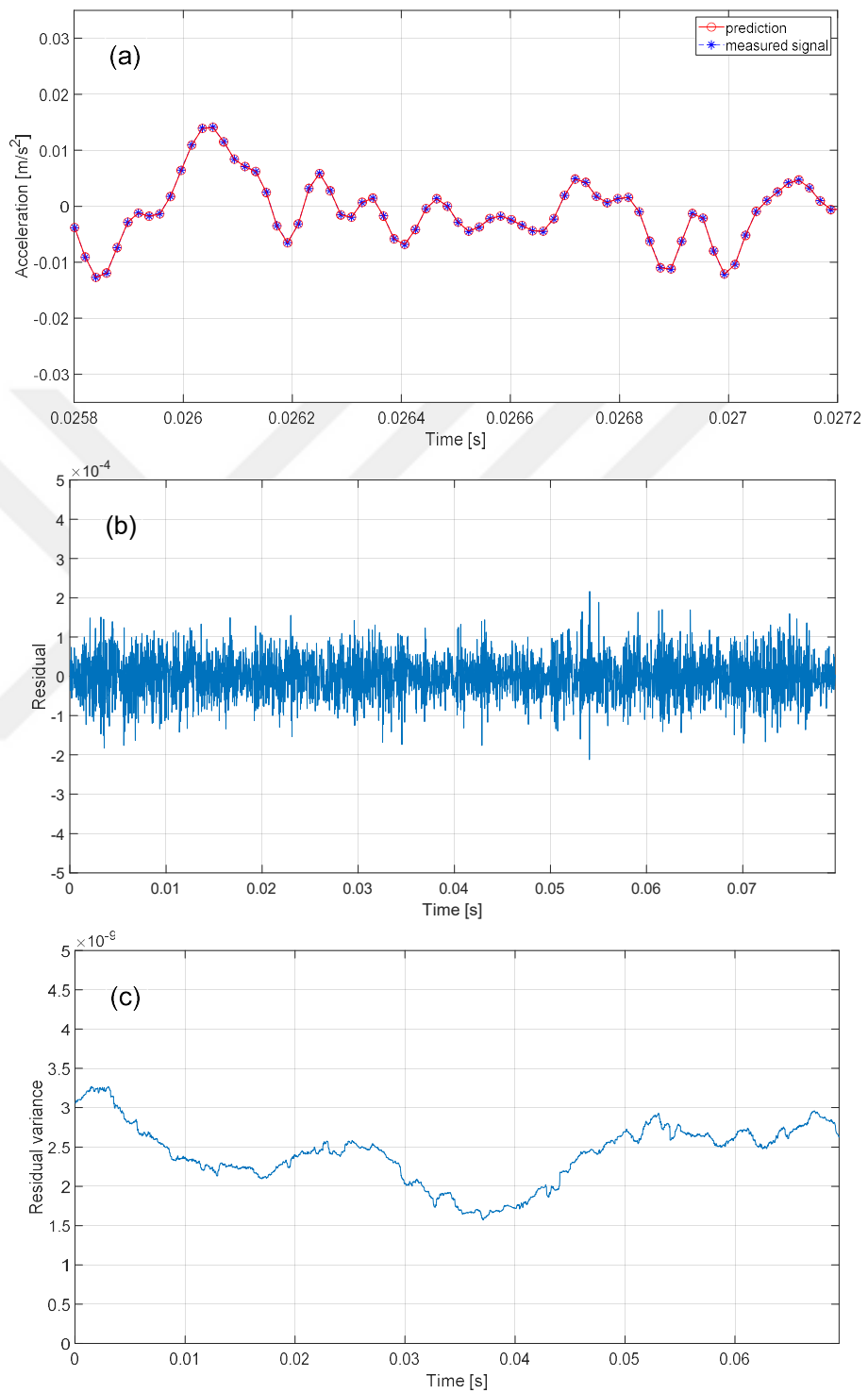


Figure 7.2 (a) Prediction vs time series for a segment of nonstationary gear acceleration, (b) residual series of estimated model, (c) residual variance

7.2 Gear fault detection based on estimated FS-TAR models

This section presents the fault detection process of the planetary gearbox with the aid of the FS-TAR model. An estimated FS-TAR model can predict the response of the gear system in a specific frequency band. However, rather than the prediction of response, the focus is on change detection based on comparing gear signals through the estimated models. The comparison can be realized by employing different tools. For instance, a time series model can be fitted to the baseline data corresponding to the healthy gearbox. A fault is detected through residual generation via faulty gear data, as it has been accomplished in [45]. Various methods can be utilized to compare the time series models. A typical approach uses a metric calculated based on model parameters. It is known that the parameters of time series models are implicitly related to the system dynamics represented by frequencies and damping. In the case of an ARMA model, the frequencies and damping ratios can be calculated through AR and MA coefficients. Time series models can be stationary or nonstationary with different orders, making the comparison somewhat complicated. AR metric $AR(\infty)$, eliminates the mentioned difficulties. It operates on AR inverse model and provides the distance of two models based on the parameters. Here, $AR(\infty)$ metric is applied to the models corresponding to healthy and faulted gears, and the change in distance is investigated.

The plot of the $AR(\infty)$ distance of the faulty FS-TAR models from the healthy one is illustrated in figure 7.3. The distance is calculated for the TSA signal obtained for one carrier revolution. Employing TSA signals already implies that the signals are averaged based on carrier speed, and the fault effects are averaged and emphasized in the associated time period. Therefore, it represents a mean behavior rather than a relationship for one revolution. The purpose is to establish a general method for fault diagnosis that can be later applied to instantaneously acquired data. According to Fig 7.3-a, multiple peaks are noticeable on the graph, three of which are local maxima and one absolute maximum, which occurs between the end and the beginning of the graphs. The first(last) maximum becomes meaningful when one considers the

periodicity of vibration signals for carrier revolution. To interpret the graph, the tools which were utilized to estimate it need to be closely investigated. The main tool is an FS-TAR model, which is a time-dependent nonstationary model that captures the time-varying behavior of the corresponding time series. The other tool is a metric that compares the baseline model and the faulted one through the model parameters, which are implicitly related to the gear system's partial dynamics. Considering the features of the employed tool, it can roughly be mentioned that peaks on the graph imply that the faulty model deviates from the baseline, which is repeated multiple times during one complete revolution of the carrier. The deviation stems from the changes in dynamics, which influences the system response in the event of faulty tooth mesh and specific frequency ranges. In the linear case, the dynamics is related to natural frequencies and associated damping ratios.

Once the duration between the peaks is calculated, it is discovered that they are approximately equal, which suggests the periodicity of the change in the distance. Since the fault is on a planet tooth, a comparison between the period of the peaks and the rotational frequency of a planet reveals that the duration is equal to the planet's frequency relative to the stationary ring gear. The frequency of carrier is $f_c = 5.98\text{Hz}$ and when compared to planet frequency $f_p = 24.18\text{Hz}$, it is expected to have between three to four contacts of planet faulty tooth with the ring gear (notice that $f_p/f_c = 4.04$).

Notably, this relationship is obtained based on kinematics only, and the tooth geometry and mesh phasing [37] between sun-planet and planet-ring mesh are not considered. Another effect is that the change in mesh stiffness or dynamic response during the faulty gear mesh occurs quickly and is not purely impulsive. Considering the mentioned effects, it can be concluded that the peaks interval does not necessarily coincide exactly to f_p , but with a negligible margin.

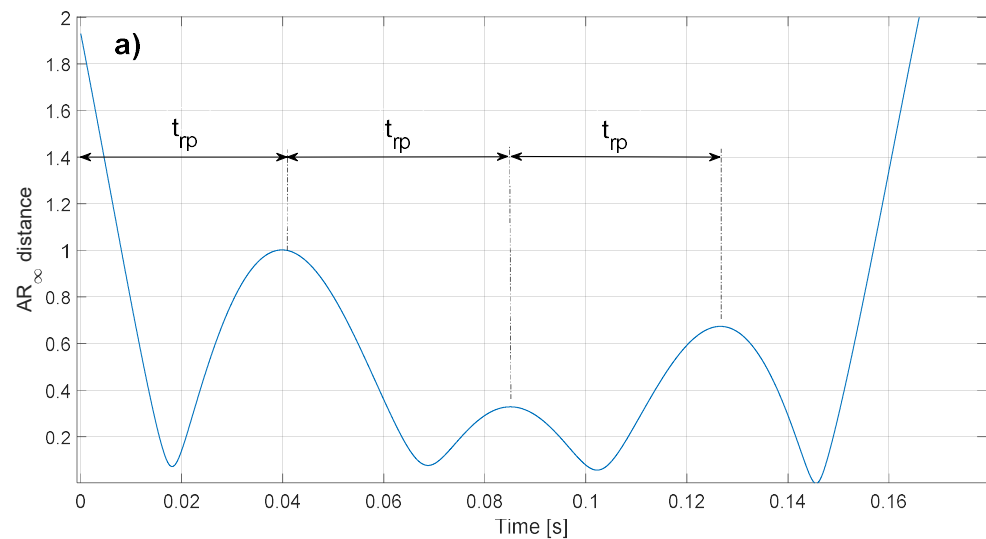
Assuming that the peaks are periodic, repeating the obtained distance curve for another period of the carrier, the graph in Fig 7.3-b is obtained, which demonstrates the periodicity in two periods clearly.

To uncover the phenomenon which results in the curve shown in Fig 8-a, the motion of the faulty planet and its mesh with the sun and ring gear considering the sensor position during the tests, is analyzed here. Consider the planetary gearbox with three planets shown in Fig 7.4-a. The faulty tooth is marked with a red circle to make it easy to follow its motion during meshing. At the start, it is assumed that the faulted tooth is in mesh with ring gear (Fig 7.4-a), and as the planet rotates due to the rotation of input gear (here, sun gear), the faulted tooth meshes with sun gear (Fig 7.4-b) and then it comes into contact with ring gear again. An accelerometer mounted on the ring gear records the gearbox vibrations transmitted through the ring gear. It can be expected that the mesh of the faulty tooth with ring gear will influence the vibrations of the gearbox sensed by the accelerometer more than its mesh with sun gear. This is due to the fact that vibration transmission paths are different in the two cases. In each of the three phases (7.4-a) -(7.4-c), in the event of faulty tooth contact, an impulse is generated, which affects the vibrations, and then it is damped out quickly between any of the two phases.

As the faulty planetary gear rotates, its faulty tooth successively meshes with the sun and ring gear or vice versa. The periodic succession of meshes that takes place in specific time intervals can be analyzed, considering the gearbox's kinematics. In the event of a mesh, the mesh stiffness is reduced, and an impulse is generated, influencing the gearbox dynamics, and hence the vibration response changes. The vibration of a planetary gearbox is intrinsically non-stationary, and it can be efficiently modeled with a non-stationary time series model. Here, FS-TAR is utilized to identify the gearbox dynamics through vibrations measured on top of the ring gear. It efficiently captures the time-varying (TV) partial dynamics of the gearbox via measured vibration signals. The accelerometer is mounted on top of the ring gear; therefore, the planet-ring mesh will influence the response and the estimated model more than the planet-sun mesh. Based on vibration transmission paths to the sensor, it is expected to have more significant deviations from the baseline response during the faulty tooth contact with the ring gear than the sun-planet mesh. The distance between the planet-ring meshes and the sensor also

influences the measured signals. Considering the descriptions given, the peaks and valleys of the graphs of Fig 7.3-a can be justified.

The method based on the AR metric and FS-TAR model applied on TSA signals provides a method for detecting the planetary gearbox and the faulty gear type, which here is a planetary gear. Fault isolation is performed based on the interval of the peaks identified on the graphs presented in Fig 7.3-a. The peaks' periodicity and multiplicity suggest that a planetary gear tooth has a concentrated fault. Furthermore, in the spectral analysis section, a detailed FFT analysis of the healthy and faulty gear signals showed the existence of a concentrated planetary gear fault. Combining the method based on FS-TAR and FFT analysis adds to the robustness of the fault diagnosis process. To detect the type of a planet fault, for instance, to make a distinction between crack and pitting, FS-TAR and AR metric may not be efficient, and mutual information from FFT analysis or other methods can increase the capability of the method.



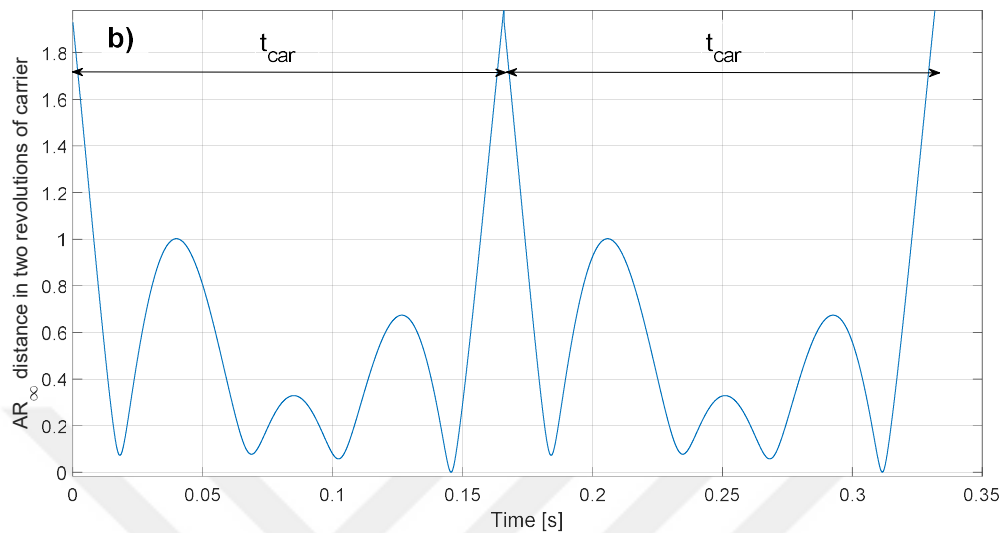


Figure 7.3 AR(∞) of FS-TAR models associated with healthy and pitted cases: a) for one revolution of carrier, b) for two revolutions of carrier; t_{pr} : planet frequency with respect to ring, t_{car} : period of carrier rotation

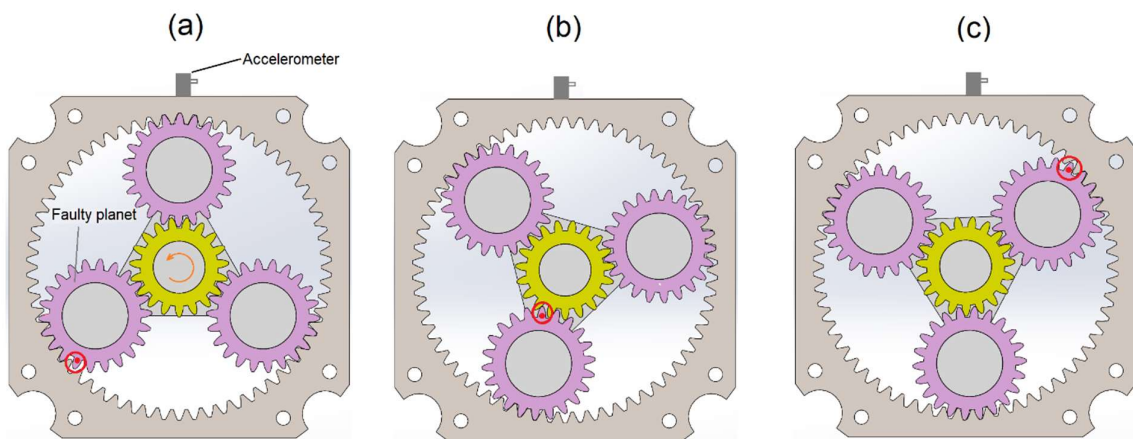


Figure 7.4 Meshing succession of planetary gear faulted tooth (marked with a red dot) with: a) ring gear (first time), b) sun gear and c) ring gear (second time)

7.3 Conclusion

This study proposed a fault detection method for a planetary gearbox based on vibration data measured under constant speed conditions. The problem of modeling nonstationary vibration signals from a planetary gearbox with planet gear fault via the FS-TAR model was considered. It was shown that the FS-TAR model could effectively model the nonstationary vibration signals, and the model coefficients were used to estimate time-dependent power spectral density. A fault diagnosis was performed using FFT analysis of TSA signals, and planet gear fault symptoms were identified. Time-dependent PSDs obtained by FS-TAR were of high resolution and could effectively identify the dominant mesh frequency harmonics as a function of time. The effects of fault on vibration response were investigated based on time-frequency analysis via PSDs, and it was revealed that dominant mesh frequency harmonics changed from harmonics 7, 12, 15, 18, 22 in healthy case to harmonics 3 and 4.

The estimated FS-TAR models possess a parametric structure, making them comparable via $AR(\infty)$ metric through their parameters. As the gears rotate, the position of the faulty tooth changes as well. With its time-dependent structure, the FS-TAR model provided a means of tracking the faulty tooth mesh during its contact with sun and ring gears. The Euclidean distance between the models associated with healthy and faulted gears was calculated by $AR(\infty)$ metric for fault detection. Peaks repeated at the planet rotation period, in the $AR(\infty)$ distance during one carrier revolution, were used to detect and classify a fault related to a planet gear. In this manner, the applicability and effectiveness of FS-TAR models in the identification of TV dynamics of planetary gear vibration and fault detection were demonstrated. Fusing the information provided by comparing FS-TAR models with the results of time-frequency analysis of the gear vibration signals can lead to more robust fault diagnosis algorithms. The method developed in this thesis can be further developed to diagnose gear faults of varying speed cases.



CHAPTER 8

Conclusion and future works

8.1 Conclusion

The current study tried to detect a planetary gearbox's fault using two different approaches. The first method is a forward method based on nonlinear dynamic modeling, including the effects of gear faults. In contrast, a second method is an inverse approach based on experimentally measured vibration signals. Its effects were included in a nonlinear dynamic model of a spur gear pair as a first step in modeling the fault. A novel method for estimating cracked tooth mesh stiffness based on fracture mechanics was developed, which facilitates the inclusion of the crack effect in dynamics models. Subsequently, linear and nonlinear dynamic models of a planetary gearbox, including planetary and sun gear tooth crack effects, were developed. The frequency analysis of the simulation results revealed that the crack influences the response mostly in high frequencies around the natural frequencies of the gearbox. The second part of the study proposed a fault detection method for a planetary gearbox based on vibration data measured under constant speed conditions. The problem of modeling nonstationary vibration signals from a planetary gearbox with planet gear fault via the FS-TAR model was considered. It was shown that the FS-TAR model could effectively model the nonstationary vibration signals, and the model coefficients were used to estimate time-dependent power spectral density. A fault diagnosis was performed using FFT analysis of TSA signals, and planet gear fault symptoms were identified. Time-dependent PSDs obtained by FS-TAR were of high resolution and could effectively identify the dominant mesh frequency harmonics as a function of time. The effects of fault on vibration response were investigated based on time-frequency analysis via PSDs, and it was revealed that

dominant mesh frequency harmonics changed from harmonics 7, 12, 15, 18, 22 in healthy case to harmonics 3 and 4.

The estimated FS-TAR models possess a parametric structure, making them comparable via $AR(\infty)$ metric through their parameters. As the gears rotate, the position of the faulty tooth changes as well. With its time-dependent structure, the FS-TAR model provided a means of tracking the faulty tooth mesh during its contact with sun and ring gears. The Euclidean distance between the models associated with healthy and faulted gears was calculated by $AR(\infty)$ metric for fault detection. Peaks repeated at the planet rotation period, in the $AR(\infty)$ distance during one carrier revolution, were used to detect and classify a fault related to a planet gear. In this manner, the applicability and effectiveness of FS-TAR models in the identification of TV dynamics of planetary gear vibration and fault detection were demonstrated. Fusing the information provided by comparing FS-TAR models with the results of time-frequency analysis of the gear vibration signals can lead to more robust fault diagnosis algorithms. The method developed in this study can be further developed to diagnose gear faults of varying speed cases. Significant contributions of this research to the state of the art in the field of gear condition monitoring can be summarized as follows:

- I. A method of modeling gear tooth root crack and mesh stiffness of cracked gear is developed that can ease the process of including crack effect in dynamic models.
- II. An algorithm based on non-stationary FS-TAR time series model and AR metric is developed that can detect and localized a fault (here planet crack) in a single step

Eventually, an approach based on a combination of non-stationary time series models and non-linear dynamic model is proposed to detect and localize a fault in planetary gear systems.

8.2 Future works

As future works, the focus will be on the following subjects:

- I. Modeling crack and pitting on any gear of a planetary gear by including its effect in mesh stiffness in a single function. This will aid dynamic modeling of faulty gears and fault diagnosis through modeling.
- II. Combining the FE model of a ring gear with the developed nonlinear lumped parameter gearbox to simulate vibration transmission paths to a sensor on top of the ring gear. This will allow for the consideration of sensor spinning effect.
- III. Extension of the developed algorithm based on non-stationary time series models to detect and localize a fault for the case of multiple faults and distributed faults (pitting on all teeth for instance).
- IV. Development of a method based on FS-TARMA model and the change in frequencies and damping ratios for gear fault detection.



REFERENCES

- [1] A. Parey, M. El Badaoui, F. Guillet, N. Tandon, Dynamic modelling of spur gear pair and application of empirical mode decomposition-based statistical analysis for early detection of localized tooth defect, *Journal of Sound and Vibration* 294 (2006) 547–561.
- [2] Yaguo Lei, Zongyao Liu, Delong Wang, Xiao Yang, Huan Liu, Jing Lin, A probability distribution model of tooth pits for evaluating time-varying mesh stiffness of pitting gears, *Mechanical Systems and Signal Processing* 106 (2018) 355–366.
- [3] Taoyuan Chen, Yanxue Wang, Zhigang Chen, A novel distribution model of multiple teeth pits for evaluating time-varying mesh stiffness of external spur gears, *Mechanical Systems and Signal Processing*, 129 (2019) 479–501.
- [4] Yunxia Chen, Yi Jin, Xihui Liang, Rui Kang, Propagation path and failure behavior analysis of cracked gears under different initial angles, *Mechanical Systems and Signal Processing* 110 (2018) 90–109.
- [5] Yang Luo, Natalie Baddour, Ming Liang, A shape-independent approach to modelling gear tooth spalls for time varying mesh stiffness evaluation of a spur gear pair, *Mechanical Systems and Signal Processing* 120 (2019) 836–852.
- [6] Yang Luo, Natalie Baddour, Ming Liang, Dynamical modeling and experimental validation for tooth pitting and spalling in spur gears, *Mechanical Systems and Signal Processing* 119 (2019) 155–181.
- [7] Junguo Wang, Jie Zhang, Zhaoyuan Yao, Xufeng Yang, Rui Sun, Yongxiang Zhao, Nonlinear characteristics of a multi-degree-of-freedom spur gear system with bending-torsional coupling vibration, *Mechanical Systems and Signal Processing* 121 (2019) 810–827.
- [8] Vikas Sharma, Anand Parey, A review of gear fault diagnosis using various condition indicators, *Procedia Engineering* 144 (2016) 253 – 263.

[9] E. Madar, R. Klein, J. Bortman, Contribution of dynamic modeling to prognostics of rotating machinery, *Mechanical Systems and Signal Processing* 123 (2019) 496–512.

[10] Nilson Barbieri, Gabriel de Sant'Anna Vitor Barbieri, Bruno Matos Martins, Lucas de Sant'Anna Vitor Barbieri, Key Fonseca de Lima, Analysis of automotive gearbox faults using vibration signal, *Mechanical Systems and Signal Processing* 129 (2019) 148–163.

[11] Yue Hu, Xiaotong Tu, Fucai Li, High-order synchrosqueezing wavelet transform and application to planetary gearbox fault diagnosis, *Mechanical Systems and Signal Processing* 131 (2019) 126–151.

[12] Sadeghi M. H., Rafiee J., Arvani F., Harifi A., “A Fault Detection and Identification System for Gearboxes using Neural Networks”, 0-7803-9422-4/05/C2005 IEEE.

[13] Rafieea J., Arvania F., Harifi A., Sadeghi M.H., “Intelligent condition monitoring of a gearbox using artificial neural network”, *Mechanical Systems and Signal Processing Journal*, 21 (2007) 1746–1754.

[14] Ettefagh M.M. Sadeghi M.H., Khanmohammadi S., “Structural Damage Detection, Using Fuzzy Classification and ARMA Parametric Modeling”, *Mech. & Aerospace Eng. Journal*, Vol.3, No.2, September 2007.

[15] B. Samanta, Gear fault detection using artificial neural networks and support vector machines with genetic algorithms, *Mechanical Systems and Signal Processing* 18 (2004) 625–644.

[16] Lixin Gao, Zhiqiang Ren, Wenliang Tang, Huaqing Wang, and Peng Chen, Intelligent Gearbox Diagnosis Methods Based on SVM, Wavelet Lifting and RBR, *Sensors* 2010, 10, 4602–4621; doi:10.3390/s100504602.

[17] T Praveenkumar, M Saimurugan, P Krishnakumar, K I Ramachandran, Fault diagnosis of automobile gearbox based on machine learning techniques, *Procedia Engineering* 97 (2014) 2092 – 2098.

[18] W. J. Wang, P. D. MCFADDEN, Application of orthogonal wavelets to early gear damage detection, *Mechanical Systems and Signal Processing* (1995) 9(5), 497-507.

[19] James McNames, Fourier Series Analysis of Epicyclic Gearbox Vibration, *Journal of Vibration and Acoustics*, Vol. 124, January 2002, 150-160.

[20] M. Inalpolat, A. Kahraman, A theoretical and experimental investigation of modulation sidebands of planetary gear sets, *Journal of Sound and Vibration* 323 (2009) 677–696.

[21] Yaguo Lei, Zongyao Liu, Jing Lin, Fanbo Lu, Phenomenological models of vibration signals for condition monitoring and fault diagnosis of epicyclic gearboxes, *Journal of Sound and Vibration* 369 (2016) 266–281.

[22] Ruo-Bin Sun, Zhi-Bo Yang, Konstantinos Gryllias, Xue-Feng Chen, Cyclostationary modeling for local fault diagnosis of planetary gear vibration signals, *Journal of Sound and Vibration* 471 (2020) 115175.

[23] Xinnan Yu, Zhipeng Feng, Ming Liang, Analytical vibration signal model and signature analysis in resonance region for planetary gearbox fault diagnosis, *Journal of Sound and Vibration* 498 (2021) 115962.

[24] P. D. McFadden, A technique for calculating the time domain averages of the vibration of the individual planet gears and the sun gear in an epicyclic gearbox, *J. Sound Vib.* 144 (1) (1991) 163–172.

[25] Dikang Peng, Wade A. Smith, Robert B. Randall, Zhongxiao Peng, Use of mesh phasing to locate faulty planet gears, *Mechanical Systems and Signal Processing* 116 (2019) 12–24.

[26] Enayet B. Halim, M. A. A. Shoukat Choudhury, Sirish L. Shah, Ming J. Zuo, Time domain averaging across all scales: A novel method for detection of gearbox faults, *Mechanical Systems and Signal Processing* 22 (2008) 261–278.

[27] Yu Guo, Lei Zhao, Xing Wu, Jing Na, Vibration separation technique based localized tooth fault detection of planetary gear sets: A tutorial, *Mechanical Systems and Signal Processing* 129 (2019) 130–147.

[28] B. Assaad, M. Eltabach, J. Antoni, Vibration based condition monitoring of a multistage epicyclic gearbox in lifting cranes, *Mech. Syst. Signal Process.* 42 (2014) 351–367, <https://doi.org/10.1016/j.ymssp.2013.06.032>.

[29] P. D. McFadden, Interpolation techniques for time domain averaging of gear vibration, *Mech. Syst. Signal Process.* 3 (1989) 87–97, [https://doi.org/10.1016/0888-3270\(89\)90024-1](https://doi.org/10.1016/0888-3270(89)90024-1).

[30] W. Wang, Autoregressive model-based diagnostics for gears and bearings, DOI: 10.1784/insi.2008.50.8.414

[31] Yuejian Chen a, Stephan Schmidt b, P. Stephan Heyns b, Ming J. Zuo, A time series model-based method for gear tooth crack detection and severity assessment under random speed variation, *Mechanical Systems and Signal Processing* 156 (2021) 107605.

[32] S. D. Fassois, F. P. Kopsaftopoulos, in: *Statistical Time Series Methods for Vibration based Structural Health Monitoring, New Trends in Structural Health Monitoring*, Springer, Vienna, 2013, pp. 209–264.

[33] M. D. Spiridonakos, S. D. Fassois, Non-stationary random vibration modelling and analysis via functional series time-dependent ARMA (FS-TARMA) models – a critical survey, *Mech. Syst. Signal Process.* 47 (1-2) (2014) 175–224, <https://doi.org/10.1016/j.ymssp.2013.06.024>.

[34] Y. Chen, X. Liang, M. J. Zuo, Time series modeling of non-stationary vibration signals for gearbox fault diagnostics, *Handbook on Performability Engineering*, Chapter 15. 2020, In Press.

[35] B. Bamieh, L. Giarre, Identification of linear parameter varying models, *International Journal of Robust and Nonlinear Control* 12 (2002) 841–853.

[36] R. Toth, Modeling and Identification of Linear Parameter-Varying Systems, Springer, 2010.

[37] Yuejian Chen, Ming J. Zuo, A sparse multivariate time series model-based fault detection method for gearboxes under variable speed condition, Mechanical Systems and Signal Processing 167 (2022) 108539.

[38] M. D. Spiridonakos, S. D. Fassois, Adaptable functional series TARMA models for non-stationary signal representation and their application to mechanical random vibration modeling, Signal Process. 96 (2014) 63–79, <https://doi.org/10.1016/j.sigpro.2013.05.012>.

[39] M. D. Spiridonakos, S. D. Fassois, An FS-TAR based method for vibration-response-based fault diagnosis in stochastic time-varying structures: Experimental application to a pick-and-place mechanism, Mech. Syst. Signal Process. 38 (1) (2013) 206–222, <https://doi.org/10.1016/j.ymssp.2012.05.014>.

[40] M. D. Spiridonakos and S. D. Fassois. Non-stationary random vibration modelling and analysis via functional series time-dependent ARMA (FS-TARMA) models - a critical survey. Mechanical Systems and Signal Processing, 2013.

[41] Poulimenos A. G., Fassois S. D. (2009) Output-only stochastic identification of a time-varying structure via functional series TARMA models Mechanical Systems and Signal Processing 23, pp. 1180–1204.

[42] Behrang Hosseini Aghdam, Ender Cigeroglu, Vibration-based tool wear estimation by using non-stationary Functional Series TARMA (FS-TARMA) models, Int J Adv Manuf Technol (2017) 93:1431–1442.

[43] Fotis Kopsaftopoulos, Raphael Nardari, Yu-Hung Li, Fu-Kuo Chang, A stochastic global identification framework for aerospace structures operating under varying flight states, Mechanical Systems and Signal Processing 98 (2018) 425–447.

[44] T.-C.I. Aravanis, J.S. Sakellariou, S.D. Fassois, A stochastic Functional Model based method for random vibration based robust fault detection under variable non-

measurable operating conditions with application to railway vehicle suspensions, Journal of Sound and Vibration 466 (2020) 115006.

[45] Ming Yang, Viliam Makis, ARX model-based gearbox fault detection and localization under varying load conditions, Journal of Sound and Vibration 329 (2010) 5209–5221.

[46] Yimin Zhan, Chris K. Mechefske, Robust detection of gearbox deterioration using compromised autoregressive modeling and Kolmogorov–Smirnov test statistic—Part I: Compromised autoregressive modeling with the aid of hypothesis tests and simulation analysis, Mechanical Systems and Signal Processing 21 (2007) 1953–1982.

[47] W. Wang, Albert K. Wong, Autoregressive Model-Based Gear Fault Diagnosis, Journal Of Vibration And Acoustics, Vol. 124, APRIL 2002, DOI: 10.1115/1.1456905.

[48] A. Wyłoman ska, J. Obuchowski, R. Zimroz, H. Hurd, Periodic autoregressive modeling of vibration time series from planetary gearbox used in bucket wheel excavator, in: Cyclostationarity: Theory and Methods, Springer, Cham, 2014, pp. 171–186.

[49] Woohyung Kim, Ji Yeong Lee, Jintai Chung, Dynamic analysis for a planetary gear with time-varying pressure angles and contact ratios, Journal of Sound and Vibration 331 (2012) 883–90.

[50] J. Lin, R. G. Parker, Analytical characterization of the unique properties of planetary gear free vibrations, Journal of Vibrations and Acoustics ASME Vol 121, july 1999.

[51] D.C.H. Yang, Z.S. Sun, A rotary model for spur gear dynamics, ASME Journal of Mechanical Transmissions and Automation in Design 107 (1985) 529–535.

[52] J. H. Kuang and Y. T. Yang, An estimate of mesh stiffness and load sharing ratio of a spur gear pair, Proceedings of the ASME 12th International Power Transmission and Gearing Conference, AZ, DE-43, 1992, pp. 1-10.

[53] H. N. Ozguven, A non-linear mathematical model for dynamic analysis of spur gears including shaft and bearing dynamics, *Journal of Sound and Vibration* (1991) 145(2), 293-260.

[54] Gitin M. Maitra, 1985, *Handbook Of Gear Design*, TATA McGraw-Hill Publishing Company Limited.

[55] M.F. White, Simulation and analysis of machinery fault signals, *Journal of Sound and Vibration* (1984) 93(1), 95-116.

[56] Chondros, T.G., Dimarogonas, A.D, 1980, Identification of Cracks in Welded Joints of Complex Structures, *Journal of Sound and Vibration*, Vol. 69, pp. 531-539.

[57] Ian Howard, Shengxiang Jia and Jiande Wang, The dynamic modeling of a spur gear in mesh including friction and a crack, *Mechanical Systems and Signal Processing* (2001) 15(5), 831-853.

[58] D. J. Ewins, *Modal Testing: Theory, Practice and Application*, Second Edition, Research Studies Press Ltd, 2000.

[59] R. G. Parker, J. Lin, Mesh Phasing relationships in planetary and epicyclic gears, *Journal of Mechanical Design*, Vol. 126, MARCH 2004, 365-370.

[60] Mian Zhang, Ming J. Zuo, Dongdong Wei, Jie Liu, KeSheng Wang, Yongshan Wang, Motion periods of sun gear dynamic fault meshing positions in planetary gear systems, *Measurement* 162 (2020) 107897.

[61] Mian Zhang, KeSheng Wang, Dongdong Wei, Ming J. Zuo, Amplitudes of characteristic frequencies for fault diagnosis of planetary gearbox, *Journal of Sound and Vibration* 432 (2018) 119–132.

[62] J. Chung, G. M. Hulbert, A Time Integration Algorithm for Structural Dynamics With Improved Numerical Dissipation: The Generalized- α Method, *Journal of Applied Mechanics*, JUNE 1993, Vol. 60/371-375.

[63] Qiang Miao, Qinghua Zhou, *Planetary Gearbox Vibration Signal Characteristics Analysis and Fault Diagnosis*, Hindawi Publishing Corporation Shock and Vibration Volume 2015, Article ID 126489, 8 pages <http://dx.doi.org/10.1155/2015/126489>.

[64] Imthiyas Manarikkal, *Planetary Gearboxes Diagnostics and Prognostics Condition Monitoring and Vibrational Analysis* (PhD thesis), Coventry University, 2022.

[65] Piccolo D. (2010) The Autoregressive metric for comparing time series models, *STATISTICA*, anno LXX, n. 4.

[66] M. Yamada, *Wavelets: Applications*, Editor(s): Jean-Pierre Françoise, Gregory L. Naber, Tsou Sheung Tsun, *Encyclopedia of Mathematical Physics*, Academic Press, 2006, Pages 420-426.

APPENDICES

A. Equations of motion of the non-linear planetary gear system

Derivatives of potential energy terms can be written as follows

$$\begin{aligned}
 \frac{\partial V}{\partial y_s} &= \sum_{i=1}^3 k_i^s \frac{\partial \delta_i^s}{\partial y_s} \delta_i^s + k_s y_s, \quad \frac{\partial \delta_i^s}{\partial y_s} = \cos(\alpha_i^s - \psi_i^s) \\
 \frac{\partial V}{\partial y_s} &= \left(k_s + \sum_{i=1}^3 \cos^2(\alpha_i^s - \psi_i^s) k_i^s \right) y_s + \left(\sum_{i=1}^3 \cos(\alpha_i^s - \psi_i^s) \sin(\alpha_i^s - \psi_i^s) k_i^s \right) x_s \\
 &\quad - \left(\sum_{i=1}^3 \cos(\alpha_i^s - \psi_i^s) \sin(\alpha_i^s - \psi_i^s) k_i^s \right) x_c - \left(\sum_{i=1}^3 \cos^2(\alpha_i^s - \psi_i^s) k_i^s \right) y_c \\
 &\quad - \sum_{i=1}^3 k_i^s \cos(\alpha_i^s - \psi_i^s) [\sin(\alpha_i^s - \psi_i^s) \cos(\theta_c + \varphi_i) \\
 &\quad + \cos(\alpha_i^s - \psi_i^s) \sin(\theta_c + \varphi_i)] \xi_i \\
 &\quad + \sum_{i=1}^3 k_i^s \cos(\alpha_i^s - \psi_i^s) [\sin(\alpha_i^s - \psi_i^s) \sin(\theta_c + \varphi_i) \\
 &\quad - \cos(\alpha_i^s - \psi_i^s) \cos(\theta_c + \varphi_i)] \eta_i + \left(\sum_{i=1}^3 R_s \cos(\alpha_i^s - \psi_i^s) k_i^s \right) \theta_s \\
 &\quad - \left(\sum_{i=1}^3 R_s \cos(\alpha_i^s - \psi_i^s) k_i^s \right) \theta_c + \sum_{i=1}^3 R_p \cos(\alpha_i^s - \psi_i^s) k_i^s \theta_i \\
 \frac{\partial V}{\partial x_s} &= \sum_{i=1}^3 k_i^s \frac{\partial \delta_i^s}{\partial x_s} \delta_i^s + k_s x_s, \quad \frac{\partial \delta_i^s}{\partial x_s} = \sin(\alpha_i^s - \psi_i^s)
 \end{aligned}$$

$$\begin{aligned}
\frac{\partial V}{\partial x_s} = & \left(k_s + \sum_{i=1}^3 \sin^2(\alpha_i^s - \psi_i^s) k_i^s \right) x_s + \left(\sum_{i=1}^3 \cos(\alpha_i^s - \psi_i^s) \sin(\alpha_i^s - \psi_i^s) k_i^s \right) y_s \\
& - \left(\sum_{i=1}^3 \sin^2(\alpha_i^s - \psi_i^s) k_i^s \right) x_c - \left(\sum_{i=1}^3 \cos(\alpha_i^s - \psi_i^s) \sin(\alpha_i^s - \psi_i^s) k_i^s \right) y_c \\
& - \sum_{i=1}^3 k_i^s \sin(\alpha_i^s - \psi_i^s) [\sin(\alpha_i^s - \psi_i^s) \cos(\theta_c + \varphi_i) \\
& + \cos(\alpha_i^s - \psi_i^s) \sin(\theta_c + \varphi_i)] \xi_i \\
& + \sum_{i=1}^3 k_i^s \sin(\alpha_i^s - \psi_i^s) [\sin(\alpha_i^s - \psi_i^s) \sin(\theta_c + \varphi_i) \\
& - \cos(\alpha_i^s - \psi_i^s) \cos(\theta_c + \varphi_i)] \eta_i + \left(\sum_{i=1}^3 R_s \sin(\alpha_i^s - \psi_i^s) k_i^s \right) \theta_s \\
& - \left(\sum_{i=1}^3 R_s \sin(\alpha_i^s - \psi_i^s) k_i^s \right) \theta_c + \sum_{i=1}^3 R_p \sin(\alpha_i^s - \psi_i^s) k_i^s \theta_i
\end{aligned}$$

$$\frac{\partial V}{\partial \theta_s} = \sum_{i=1}^3 k_i^s \frac{\partial \delta_i^s}{\partial \theta_s} \delta_i^s, \quad \frac{\partial \delta_i^s}{\partial \theta_s} = R_s$$

$$\begin{aligned}
\frac{\partial V}{\partial \theta_s} = & \left(\sum_{i=1}^3 R_s \sin(\alpha_i^s - \psi_i^s) k_i^s \right) x_s - \left(\sum_{i=1}^3 R_s \sin(\alpha_i^s - \psi_i^s) k_i^s \right) x_c \\
& - \sum_{i=1}^3 R_s k_i^s [\sin(\alpha_i^s - \psi_i^s) \cos(\theta_c + \varphi_i) + \cos(\alpha_i^s - \psi_i^s) \sin(\theta_c + \varphi_i)] \xi_i \\
& + \sum_{i=1}^3 R_s k_i^s [\sin(\alpha_i^s - \psi_i^s) \sin(\theta_c + \varphi_i) - \cos(\alpha_i^s - \psi_i^s) \cos(\theta_c + \varphi_i)] \eta_i \\
& + \left(\sum_{i=1}^3 R_s \cos(\alpha_i^s - \psi_i^s) k_i^s \right) y_s - \left(\sum_{i=1}^3 R_s \cos(\alpha_i^s - \psi_i^s) k_i^s \right) y_c \\
& + \left(\sum_{i=1}^3 R_s^2 k_i^s \right) \theta_s - \left(\sum_{i=1}^3 R_s^2 k_i^s \right) \theta_c + \sum_{i=1}^3 R_s R_p k_i^s \theta_i
\end{aligned}$$

$$\begin{aligned}
\frac{\partial V}{\partial x_c} &= k_c x_c + \sum_{i=1}^3 \left(k_i^s \frac{\partial \delta_i^s}{\partial x_c} \delta_i^s + k_i^r \frac{\partial \delta_i^r}{\partial x_c} \delta_i^r \right) \\
&= \left(k_c + \sum_{i=1}^3 \sin^2(\alpha_i^s - \psi_i^s) k_i^s + \sum_{i=1}^3 \sin^2(\alpha_i^r + \psi_i^r) k_i^r \right) x_c \\
&\quad + \left(\sum_{i=1}^3 \cos(\alpha_i^s - \psi_i^s) \sin(\alpha_i^s - \psi_i^s) k_i^s \right. \\
&\quad \left. - \sum_{i=1}^3 \cos(\alpha_i^r + \psi_i^r) \sin(\alpha_i^r + \psi_i^r) k_i^r \right) y_c - \left(\sum_{i=1}^3 \sin^2(\alpha_i^s - \psi_i^s) k_i^s \right) x_c \\
&\quad - \left(\sum_{i=1}^3 \cos(\alpha_i^s - \psi_i^s) \sin(\alpha_i^s - \psi_i^s) k_i^s \right) y_c - \left(\sum_{i=1}^3 \sin^2(\alpha_i^s - \psi_i^s) k_i^s \right) x_s \\
&\quad - \left(\sum_{i=1}^3 \cos(\alpha_i^s - \psi_i^s) \sin(\alpha_i^s - \psi_i^s) k_i^s \right) y_s \\
&\quad + \sum_{i=1}^3 (k_i^r \sin(\alpha_i^r + \psi_i^r) [\sin(\alpha_i^r + \psi_i^r) \cos(\theta_c + \varphi_i) \\
&\quad - \cos(\alpha_i^s - \psi_i^s) \sin(\theta_c + \varphi_i)] \\
&\quad + k_i^s \sin(\alpha_i^s - \psi_i^s) [\sin(\alpha_i^s - \psi_i^s) \cos(\theta_c + \varphi_i) \\
&\quad + \cos(\alpha_i^s - \psi_i^s) \sin(\theta_c + \varphi_i)]) \xi_i \\
&\quad + \sum_{i=1}^3 (k_i^s \sin(\alpha_i^s - \psi_i^s) [-\sin(\alpha_i^s - \psi_i^s) \sin(\theta_c + \varphi_i) \\
&\quad + \cos(\alpha_i^s - \psi_i^s) \cos(\theta_c + \varphi_i)] \\
&\quad - k_i^r \sin(\alpha_i^r + \psi_i^r) [\sin(\alpha_i^r + \psi_i^r) \sin(\theta_c + \varphi_i) \\
&\quad + \cos(\alpha_i^r + \psi_i^r) \cos(\theta_c + \varphi_i)]) \eta_i - \left(\sum_{i=1}^3 R_s \sin(\alpha_i^s - \psi_i^s) k_i^s \right) \theta_s \\
&\quad + \left(\sum_{i=1}^3 R_s \sin(\alpha_i^s - \psi_i^s) k_i^s - R_r \sin(\alpha_i^r + \psi_i^r) k_i^r \right) \theta_c \\
&\quad - \sum_{i=1}^3 R_p (\sin(\alpha_i^s - \psi_i^s) k_i^s + \sin(\alpha_i^r + \psi_i^r) k_i^r) \theta_i
\end{aligned}$$

$$\begin{aligned}
\frac{\partial V}{\partial y_c} &= k_c y_c + \sum_{i=1}^3 \left(k_i^s \frac{\partial \delta_i^s}{\partial y_c} \delta_i^s + k_i^r \frac{\partial \delta_i^r}{\partial y_c} \delta_i^r \right) \\
&= \left(\sum_{i=1}^3 \sin(\alpha_i^s - \psi_i^s) \cos(\alpha_i^s - \psi_i^s) k_i^s - \cos(\alpha_i^r + \psi_i^r) \sin(\alpha_i^r + \psi_i^r) k_i^r \right) x_c \\
&\quad + \left(k_c + \sum_{i=1}^3 \cos^2(\alpha_i^s - \psi_i^s) k_i^s + \sum_{i=1}^3 \cos^2(\alpha_i^r + \psi_i^r) k_i^r \right) y_c \\
&\quad - \left(\sum_{i=1}^3 \cos(\alpha_i^s - \psi_i^s) \sin(\alpha_i^s - \psi_i^s) k_i^s \right) x_s - \left(\sum_{i=1}^3 \cos^2(\alpha_i^s - \psi_i^s) k_i^s \right) y_s \\
&\quad + \sum_{i=1}^3 (k_i^r \cos(\alpha_i^r + \psi_i^r) [-\sin(\alpha_i^r + \psi_i^r) \cos(\theta_c + \varphi_i) \\
&\quad - \cos(\alpha_i^s - \psi_i^s) \sin(\theta_c + \varphi_i)] \\
&\quad + k_i^s \cos(\alpha_i^s - \psi_i^s) [\sin(\alpha_i^s - \psi_i^s) \cos(\theta_c + \varphi_i) \\
&\quad + \cos(\alpha_i^s - \psi_i^s) \sin(\theta_c + \varphi_i)]) \xi_i \\
&\quad + \sum_{i=1}^3 (k_i^s \cos(\alpha_i^s - \psi_i^s) [-\sin(\alpha_i^s - \psi_i^s) \sin(\theta_c + \varphi_i) \\
&\quad + \cos(\alpha_i^s - \psi_i^s) \cos(\theta_c + \varphi_i)] \\
&\quad - k_i^r \sin(\alpha_i^r + \psi_i^r) [\sin(\alpha_i^r + \psi_i^r) \sin(\theta_c + \varphi_i) \\
&\quad + \cos(\alpha_i^r + \psi_i^r) \cos(\theta_c + \varphi_i)]) \eta_i - \left(\sum_{i=1}^3 R_s \cos(\alpha_i^s - \psi_i^s) k_i^s \right) \theta_s \\
&\quad + \left(\sum_{i=1}^3 R_s \cos(\alpha_i^s - \psi_i^s) k_i^s - R_r \sin(\alpha_i^r + \psi_i^r) k_i^r \right) \theta_c \\
&\quad - \sum_{i=1}^3 R_p (\cos(\alpha_i^s - \psi_i^s) k_i^s + \sin(\alpha_i^r + \psi_i^r) k_i^r) \theta_i
\end{aligned}$$

$$\frac{\partial V}{\partial \theta_c} = \sum_{i=1}^3 \left(k_i^s \frac{\partial \delta_i^s}{\partial \theta_c} \delta_i^s + k_i^r \frac{\partial \delta_i^r}{\partial \theta_c} \delta_i^r \right)$$

$$\begin{aligned}
\frac{\partial \delta_i^s}{\partial \theta_c} &= [\sin(\theta_c + \varphi_i) \xi_i + \cos(\theta_c + \varphi_i) \eta_i] \sin(\alpha_i^s - \psi_i^s) \\
&\quad + [-\cos(\theta_c + \varphi_i) \xi_i + \sin(\theta_c + \varphi_i) \eta_i] \cos(\alpha_i^s - \psi_i^s) - R_s
\end{aligned}$$

$$\begin{aligned}
\frac{\partial \delta_i^r}{\partial \theta_c} &= [-\sin(\theta_c + \varphi_i) \xi_i - \cos(\theta_c + \varphi_i) \eta_i] \sin(\alpha_i^r + \psi_i^r) \\
&\quad - [-\cos(\theta_c + \varphi_i) \xi_i - \sin(\theta_c + \varphi_i) \eta_i] \cos(\alpha_i^r + \psi_i^r) - R_r
\end{aligned}$$

$$\begin{aligned}
\frac{\partial V}{\partial \theta_c} = & \left(\sum_{i=1}^3 k_i^s R_s^2 \right) \theta_s + \sum_{i=1}^3 k_i^s R_p (-R_s k_i^s + R_r k_i^r) \theta_i + \left(\sum_{i=1}^3 k_i^s R_s^2 + k_i^r R_r^2 \right) \theta_c \\
& + \sum_{i=1}^3 k_i^s \{ [\sin(\theta_c + \varphi_i) \sin(\alpha_i^s - \psi_i^s) - \cos(\theta_c + \varphi_i) \cos(\alpha_i^s - \psi_i^s)] \xi_i \\
& + [\cos(\theta_c + \varphi_i) \sin(\alpha_i^s - \psi_i^s) + \sin(\theta_c + \varphi_i) \cos(\alpha_i^s - \psi_i^s)] \eta_i \} \\
& \times \{ [x_s - x_c - \cos(\theta_c + \varphi_i) \xi_i + \sin(\theta_c + \varphi_i) \eta_i] \sin(\alpha_i^s - \psi_i^s) \\
& + [y_s - y_c - \sin(\theta_c + \varphi_i) \xi_i - \cos(\theta_c + \varphi_i) \eta_i] \cos(\alpha_i^s - \psi_i^s) \\
& + R_s (\theta_s - \theta_c) + R_p \theta_i \} \\
& - \sum_{i=1}^3 R_s k_i^s \{ [x_s - x_c - \cos(\theta_c + \varphi_i) \xi_i + \sin(\theta_c + \varphi_i) \eta_i] \sin(\alpha_i^s - \psi_i^s) \\
& + [y_s - y_c - \sin(\theta_c + \varphi_i) \xi_i - \cos(\theta_c + \varphi_i) \eta_i] \cos(\alpha_i^s - \psi_i^s) \} \\
& + \sum_{i=1}^3 k_i^r \{ [-\sin(\theta_c + \varphi_i) \sin(\alpha_i^r + \psi_i^r) - \cos(\theta_c + \varphi_i) \cos(\alpha_i^r + \psi_i^r)] \xi_i \\
& + [-\cos(\theta_c + \varphi_i) \sin(\alpha_i^r + \psi_i^r) + \sin(\theta_c + \varphi_i) \cos(\alpha_i^r + \psi_i^r)] \eta_i \} \\
& \times \{ [x_c + \cos(\theta_c + \varphi_i) \xi_i - \sin(\theta_c + \varphi_i) \eta_i] \sin(\alpha_i^r + \psi_i^r) \\
& - [y_c + \sin(\theta_c + \varphi_i) \xi_i + \cos(\theta_c + \varphi_i) \eta_i] \cos(\alpha_i^r + \psi_i^r) - R_r \theta_c - R_p \theta_i \} \\
& - \sum_{i=1}^3 k_i^r R_r \{ [x_c + \cos(\theta_c + \varphi_i) \xi_i - \sin(\theta_c + \varphi_i) \eta_i] \sin(\alpha_i^r + \psi_i^r) \\
& - [y_c + \sin(\theta_c + \varphi_i) \xi_i + \cos(\theta_c + \varphi_i) \eta_i] \cos(\alpha_i^r + \psi_i^r) \}
\end{aligned}$$

$$\frac{\partial V}{\partial \xi_j} = \left(k_p \xi_i + k_i^s \frac{\partial \delta_i^s}{\partial \xi_j} \delta_i^s + k_i^r \frac{\partial \delta_i^r}{\partial \xi_j} \delta_i^r \right) \delta_{ij}$$

$$\frac{\partial \delta_i^s}{\partial \xi_j} = -[\cos(\theta_c + \varphi_j) \sin(\alpha_j^s - \psi_j^s) + \sin(\theta_c + \varphi_j) \cos(\alpha_j^s - \psi_j^s)]$$

$$\frac{\partial \delta_i^r}{\partial \xi_j} = [\cos(\theta_c + \varphi_j) \sin(\alpha_j^r + \psi_j^r) - \sin(\theta_c + \varphi_j) \cos(\alpha_j^r + \psi_j^r)]$$

$$\begin{aligned}
\frac{\partial V}{\partial \xi_j} = & (k_p \xi_i + k_i^s [\cos(\theta_c + \varphi_j) \sin(\alpha_j^s - \psi_j^s) + \sin(\theta_c + \varphi_j) \cos(\alpha_j^s - \psi_j^s)]) \\
& \times \{ [x_s - x_c - \cos(\theta_c + \varphi_i) \xi_i + \sin(\theta_c + \varphi_i) \eta_i] \sin(\alpha_i^s - \psi_i^s) \\
& + [y_s - y_c - \sin(\theta_c + \varphi_i) \xi_i - \cos(\theta_c + \varphi_i) \eta_i] \cos(\alpha_i^s - \psi_i^s) \\
& + R_s (\theta_s - \theta_c) + R_p \theta_i \} \\
& + k_i^r [\cos(\theta_c + \varphi_j) \sin(\alpha_j^r + \psi_j^r) \\
& - \sin(\theta_c + \varphi_j) \cos(\alpha_j^r + \psi_j^r)] \{ [x_c + \cos(\theta_c + \varphi_i) \xi_i \\
& - \sin(\theta_c + \varphi_i) \eta_i] \sin(\alpha_i^r + \psi_i^r) \\
& - [y_c + \sin(\theta_c + \varphi_i) \xi_i + \cos(\theta_c + \varphi_i) \eta_i] \cos(\alpha_i^r + \psi_i^r) - R_r \theta_c \\
& - R_p \} \} \delta_{ij}
\end{aligned}$$

$$\begin{aligned}
\frac{\partial V}{\partial \eta_j} &= \left(k_p \eta_i + k_i^s \frac{\partial \delta_i^s}{\partial \eta_i} \delta_i^s + k_i^r \frac{\partial \delta_i^r}{\partial \eta_i} \delta_i^r \right) \delta_{ij} \\
\frac{\partial \delta_i^s}{\partial \eta_j} &= [\sin(\theta_c + \varphi_i) \sin(\alpha_i^s - \psi_i^s) - \cos(\theta_c + \varphi_i) \cos(\alpha_i^s - \psi_i^s)] \delta_{ij} \\
\frac{\partial \delta_i^r}{\partial \eta_j} &= -[\sin(\theta_c + \varphi_i) \sin(\alpha_i^r + \psi_i^r) + \cos(\theta_c + \varphi_i) \cos(\alpha_i^r + \psi_i^r)] \delta_{ij} \\
\frac{\partial V}{\partial \eta_j} &= (k_p \eta_i + k_i^s [\sin(\theta_c + \varphi_j) \sin(\alpha_j^s - \psi_j^s) - \cos(\theta_c + \varphi_j) \cos(\alpha_j^s - \psi_j^s)] \\
&\quad \times \{[x_s - x_c - \cos(\theta_c + \varphi_i) \xi_i + \sin(\theta_c + \varphi_i) \eta_i] \sin(\alpha_i^s - \psi_i^s) \\
&\quad + [y_s - y_c - \sin(\theta_c + \varphi_i) \xi_i - \cos(\theta_c + \varphi_i) \eta_i] \cos(\alpha_i^s - \psi_i^s) \\
&\quad + R_s(\theta_s - \theta_c) + R_p \theta_i\} \\
&\quad - k_i^r [\sin(\theta_c + \varphi_j) \sin(\alpha_j^r + \psi_j^r)] \{[x_c + \cos(\theta_c + \varphi_i) \xi_i \\
&\quad - \sin(\theta_c + \varphi_i) \eta_i] \sin(\alpha_i^r + \psi_i^r) \\
&\quad - [y_c + \sin(\theta_c + \varphi_i) \xi_i + \cos(\theta_c + \varphi_i) \eta_i] \cos(\alpha_i^r + \psi_i^r) - R_r \theta_c \\
&\quad - R_p\}) \delta_{ij} \\
\frac{\partial V}{\partial \theta_j} &= (k_i^s R_p \delta_i^s - k_i^r R_p \delta_i^r) \delta_{ij} \\
\frac{\partial V}{\partial \theta_j} &= (k_j^s R_s R_p) \theta_s - (k_j^s R_s R_p) \theta_c + (k_j^s + k_j^r) R_p^2 \theta_i \\
&\quad + k_j^s R_p \{[x_s - x_c - \cos(\theta_c + \varphi_i) \xi_i + \sin(\theta_c + \varphi_i) \eta_i] \sin(\alpha_i^s - \psi_i^s) \\
&\quad + [y_s - y_c - \sin(\theta_c + \varphi_i) \xi_i - \cos(\theta_c + \varphi_i) \eta_i] \cos(\alpha_i^s - \psi_i^s)\} \delta_{ij} \\
&\quad + (k_i^r R_r R_p) \theta_c \\
&\quad - k_i^r R_p \{[x_c + \cos(\theta_c + \varphi_i) \xi_i - \sin(\theta_c + \varphi_i) \eta_i] \sin(\alpha_i^r + \psi_i^r) \\
&\quad - [y_c + \sin(\theta_c + \varphi_i) \xi_i + \cos(\theta_c + \varphi_i) \eta_i] \cos(\alpha_i^r + \psi_i^r)\} \delta_{ij}
\end{aligned}$$

Derivatives of the kinetic energy terms are as follows

$$\begin{aligned}
\frac{\partial T}{\partial \dot{x}_s} &= m_s \dot{x}_s, \frac{d}{dt} \left(\frac{\partial T}{\partial \dot{x}_s} \right) = m_s \ddot{x}_s \\
\frac{\partial T}{\partial \dot{\theta}_s} &= I_s \dot{\theta}_s, \frac{d}{dt} \left(\frac{\partial T}{\partial \dot{\theta}_s} \right) = I_s \ddot{\theta}_s \\
\frac{\partial T}{\partial \dot{x}_c} &= m_c \dot{x}_c + \sum_{i=1}^3 m_p \dot{x}_i, \frac{d}{dt} \left(\frac{\partial T}{\partial \dot{x}_c} \right) = m_c \ddot{x}_c + \sum_{i=1}^3 m_p \ddot{x}_i
\end{aligned}$$

where

$$\begin{aligned}
\ddot{x}_i &= \ddot{x}_c + \ddot{\xi}_i \cos(\theta_c + \varphi_i) - 2\dot{\xi}_i \dot{\theta}_c \sin(\theta_c + \varphi_i) - (\xi_i + R_c) \ddot{\theta}_c \sin(\theta_c + \varphi_i) \\
&\quad - (\xi_i + R_c) \dot{\theta}_c^2 \cos(\theta_c + \varphi_i) - \ddot{\eta}_i \sin(\theta_c + \varphi_i) - 2\dot{\eta}_i \dot{\theta}_c \cos(\theta_c + \varphi_i) \\
&\quad - \eta_i \ddot{\theta}_c \cos(\theta_c + \varphi_i) + \eta_i \dot{\theta}_c^2 \sin(\theta_c + \varphi_i) \\
\ddot{y}_i &= \ddot{y}_c + \ddot{\xi}_i \sin(\theta_c + \varphi_i) + 2\dot{\xi}_i \dot{\theta}_c \cos(\theta_c + \varphi_i) + (\xi_i + R_c) \ddot{\theta}_c \cos(\theta_c + \varphi_i) \\
&\quad - (\xi_i + R_c) \dot{\theta}_c^2 \sin(\theta_c + \varphi_i) + \ddot{\eta}_i \cos(\theta_c + \varphi_i) - 2\dot{\eta}_i \dot{\theta}_c \sin(\theta_c + \varphi_i) \\
&\quad - \eta_i \ddot{\theta}_c \sin(\theta_c + \varphi_i) - \eta_i \dot{\theta}_c^2 \cos(\theta_c + \varphi_i) \\
\frac{d}{dt} \left(\frac{\partial T}{\partial \dot{x}_c} \right) &= \left(m_c + \sum_{i=1}^3 m_p \right) \ddot{x}_c + \sum_{i=1}^3 m_p \cos(\theta_c + \varphi_i) \ddot{\xi}_i \\
&\quad - \left(\sum_{i=1}^3 m_p [(\xi_i + R_c) \sin(\theta_c + \varphi_i) + \eta_i \cos(\theta_c + \varphi_i)] \right) \ddot{\theta}_c \\
&\quad - \sum_{i=1}^3 m_p \sin(\theta_c + \varphi_i) \ddot{\eta}_i \\
&\quad + \sum_{i=1}^3 m_p \left(-2\dot{\xi}_i \dot{\theta}_c \sin(\theta_c + \varphi_i) - (\xi_i + R_c) \dot{\theta}_c^2 \cos(\theta_c + \varphi_i) \right. \\
&\quad \left. - 2\dot{\eta}_i \dot{\theta}_c \cos(\theta_c + \varphi_i) + \eta_i \dot{\theta}_c^2 \sin(\theta_c + \varphi_i) \right) \\
\frac{\partial T}{\partial \dot{y}_c} &= m_c \ddot{y}_c + \sum_{i=1}^3 m_p \ddot{y}_i, \quad \frac{d}{dt} \left(\frac{\partial T}{\partial \dot{y}_c} \right) = m_c \ddot{y}_c + \sum_{i=1}^3 m_p \ddot{y}_i \\
\frac{d}{dt} \left(\frac{\partial T}{\partial \dot{y}_c} \right) &= \left(m_c + \sum_{i=1}^3 m_p \right) \ddot{y}_c + \sum_{i=1}^3 m_p \sin(\theta_c + \varphi_i) \ddot{\xi}_i \\
&\quad + \left(\sum_{i=1}^3 m_p [(\xi_i + R_c) \cos(\theta_c + \varphi_i) - \eta_i \sin(\theta_c + \varphi_i)] \right) \ddot{\theta}_c \\
&\quad + \sum_{i=1}^3 m_p \cos(\theta_c + \varphi_i) \ddot{\eta}_i \\
&\quad + \sum_{i=1}^3 m_p \left(2\dot{\xi}_i \dot{\theta}_c \cos(\theta_c + \varphi_i) - (\xi_i + R_c) \dot{\theta}_c^2 \sin(\theta_c + \varphi_i) \right. \\
&\quad \left. - 2\dot{\eta}_i \dot{\theta}_c \sin(\theta_c + \varphi_i) - \eta_i \dot{\theta}_c^2 \cos(\theta_c + \varphi_i) \right) \\
\frac{\partial T}{\partial \dot{\theta}_c} &= I_c \dot{\theta}_c + \sum_{i=1}^3 m_p \left[\dot{x}_i \frac{\partial \dot{x}_i}{\partial \dot{\theta}_c} + \dot{y}_i \frac{\partial \dot{y}_i}{\partial \dot{\theta}_c} \right] + \sum_{i=1}^3 I_p (\dot{\theta}_c + \dot{\theta}_i) \\
\frac{\partial \dot{x}_i}{\partial \dot{\theta}_c} &= -[(\xi_i + R_c) \sin(\theta_c + \varphi_i) + \eta_i \cos(\theta_c + \varphi_i)]
\end{aligned}$$

$$\frac{\partial \dot{y}_i}{\partial \dot{\theta}_c} = [(\xi_i + R_c) \cos(\theta_c + \varphi_i) - \eta_i \sin(\theta_c + \varphi_i)]$$

$$\frac{\partial T}{\partial \theta_c} = \sum_{i=1}^3 m_p \left[\dot{x}_i \frac{\partial \dot{x}_i}{\partial \theta_c} + \dot{y}_i \frac{\partial \dot{y}_i}{\partial \theta_c} \right]$$

In the Lagrange's equation the term $\frac{d}{dt} \left(\frac{\partial T}{\partial \dot{\theta}_c} \right) - \frac{\partial T}{\partial \theta_c}$ will appear. After some manipulation, the following equation is obtained.

$$\begin{aligned} \frac{d}{dt} \left(\frac{\partial T}{\partial \dot{\theta}_c} \right) - \frac{\partial T}{\partial \theta_c} &= \left(I_c + \sum_{i=1}^3 I_p \right) \ddot{\theta}_c + \sum_{i=1}^3 I_p \ddot{\theta}_i - \sum_{i=1}^3 m_p \eta_i \ddot{\xi}_i + \sum_{i=1}^3 m_p (\xi_i + R_c) \ddot{\eta}_i \\ &+ \left(\sum_{i=1}^3 m_p [(\xi_i + R_c)^2 + \eta_i^2] \right) \ddot{\theta}_c \\ &+ \left(\sum_{i=1}^3 m_p [-(\xi_i + R_c) \sin(\theta_c + \varphi_i) - \eta_i \cos(\theta_c + \varphi_i)] \right) \ddot{x}_c \\ &+ \left(\sum_{i=1}^3 m_p [(\xi_i + R_c) \cos(\theta_c + \varphi_i) - \eta_i \sin(\theta_c + \varphi_i)] \right) \ddot{y}_c \\ &+ \sum_{i=1}^3 m_p [2\dot{\xi}_i \dot{\theta}_c (\xi_i + R_c) + 2\dot{\eta}_i \dot{\theta}_c] \end{aligned}$$

$$\frac{\partial T}{\partial \dot{\xi}_i} = m_p \left[\dot{x}_i \frac{\partial \dot{x}_i}{\partial \dot{\xi}_i} + \dot{y}_i \frac{\partial \dot{y}_i}{\partial \dot{\xi}_i} \right]$$

$$\begin{aligned} \frac{d}{dt} \left(\frac{\partial T}{\partial \dot{\xi}_i} \right) &= m_p \left\{ \left[\ddot{x}_c + \cos(\theta_c + \varphi_i) \ddot{\xi}_i - 2\dot{\xi}_i \dot{\theta}_c \sin(\theta_c + \varphi_i) - (\xi_i + R_c) \ddot{\theta}_c \sin(\theta_c + \varphi_i) \right. \right. \\ &\quad - (\xi_i + R_c) \dot{\theta}_c^2 \cos(\theta_c + \varphi_i) - \dot{\eta}_i \sin(\theta_c + \varphi_i) - 2\dot{\eta}_i \dot{\theta}_c \cos(\theta_c + \varphi_i) \\ &\quad - \eta_i \dot{\theta}_c \cos(\theta_c + \varphi_i) + \eta_i \dot{\theta}_c^2 \sin(\theta_c + \varphi_i) \left. \right] \cos(\theta_c + \varphi_i) \\ &\quad - \left[\dot{x}_c + \dot{\xi}_i \cos(\theta_c + \varphi_i) - (\xi_i + R_c) \dot{\theta}_c \sin(\theta_c + \varphi_i) - \dot{\eta}_i \sin(\theta_c + \varphi_i) \right. \\ &\quad - \eta_i \dot{\theta}_c \cos(\theta_c + \varphi_i) \left. \right] \dot{\theta}_c \sin(\theta_c + \varphi_i) \\ &\quad + \left[\ddot{y}_c + \sin(\theta_c + \varphi_i) \ddot{\xi}_i + 2\dot{\xi}_i \dot{\theta}_c \cos(\theta_c + \varphi_i) + (\xi_i + R_c) \ddot{\theta}_c \cos(\theta_c + \varphi_i) \right. \\ &\quad - (\xi_i + R_c) \dot{\theta}_c^2 \sin(\theta_c + \varphi_i) + \dot{\eta}_i \cos(\theta_c + \varphi_i) - 2\dot{\eta}_i \dot{\theta}_c \sin(\theta_c + \varphi_i) \\ &\quad - \eta_i \dot{\theta}_c \sin(\theta_c + \varphi_i) - \eta_i \dot{\theta}_c^2 \cos(\theta_c + \varphi_i) \left. \right] \sin(\theta_c + \varphi_i) \\ &\quad + \left[\dot{y}_c + \dot{\xi}_i \sin(\theta_c + \varphi_i) + (\xi_i + R_c) \dot{\theta}_c \cos(\theta_c + \varphi_i) - \dot{\eta}_i \sin(\theta_c + \varphi_i) \right. \\ &\quad - \eta_i \dot{\theta}_c \sin(\theta_c + \varphi_i) \left. \right] \dot{\theta}_c \cos(\theta_c + \varphi_i) \} \end{aligned}$$

$$\frac{d}{dt} \left(\frac{\partial T}{\partial \dot{\xi}_i} \right) = (m_p \cos(\theta_c + \varphi_i)) \ddot{x}_c + m_p \ddot{\xi}_i - (m_p \eta_i) \ddot{\theta}_c + (m_p \sin(\theta_c + \varphi_i)) \ddot{y}_c + m_p [-\dot{\eta}_i \dot{\theta}_c - \dot{x}_c \dot{\theta}_c \sin(\theta_c + \varphi_i) + y_c \dot{\theta}_c \cos(\theta_c + \varphi_i)]$$

$$\begin{aligned} \frac{\partial T}{\partial \xi_i} = m_p & \left[-\dot{x}_c \dot{\theta}_c \sin(\theta_c + \varphi_i) - \dot{\xi}_i \dot{\theta}_c \sin(\theta_c + \varphi_i) \cos(\theta_c + \varphi_i) \right. \\ & + (\xi_i + R_c) \dot{\theta}_c^2 \sin^2(\theta_c + \varphi_i) + \dot{\eta}_i \dot{\theta}_c \sin^2(\theta_c + \varphi_i) \\ & + \eta_i \dot{\theta}_c^2 \sin(\theta_c + \varphi_i) \cos(\theta_c + \varphi_i) + \dot{y}_c \dot{\theta}_c \cos(\theta_c + \varphi_i) \\ & + \dot{\xi}_i \dot{\theta}_c \sin(\theta_c + \varphi_i) \cos(\theta_c + \varphi_i) + (\xi_i + R_c) \dot{\theta}_c^2 \cos(\theta_c + \varphi_i) \\ & \left. + \dot{\eta}_i \dot{\theta}_c \cos^2(\theta_c + \varphi_i) - \eta_i \dot{\theta}_c^2 \sin(\theta_c + \varphi_i) \cos(\theta_c + \varphi_i) \right] \end{aligned}$$

$$\frac{\partial T}{\partial \dot{\xi}_i} = m_p \left[-\dot{x}_c \dot{\theta}_c \sin(\theta_c + \varphi_i) + (\xi_i + R_c) \dot{\theta}_c^2 + \dot{\eta}_i \dot{\theta}_c + \dot{y}_c \dot{\theta}_c \cos(\theta_c + \varphi_i) \right]$$

$$\begin{aligned} \frac{d}{dt} \left(\frac{\partial T}{\partial \dot{\xi}_i} \right) - \frac{\partial T}{\partial \xi_i} = & (m_p \cos(\theta_c + \varphi_i)) \ddot{x}_c + m_p \ddot{\xi}_i - (m_p \eta_i) \ddot{\theta}_c + (m_p \sin(\theta_c + \varphi_i)) \ddot{y}_c \\ & + m_p [-2\dot{\eta}_i \dot{\theta}_c - (\xi_i + R_c) \dot{\theta}_c^2] \end{aligned}$$

Similarly for the coordinate η_i , the following equation is obtained

$$\begin{aligned} \frac{d}{dt} \left(\frac{\partial T}{\partial \dot{\eta}_i} \right) - \frac{\partial T}{\partial \eta_i} = & (-m_p \sin(\theta_c + \varphi_i)) \ddot{x}_c + m_p \ddot{\eta}_i + (m_p (\xi_i + R_c)) \ddot{\theta}_c \\ & + (m_p \cos(\theta_c + \varphi_i)) \ddot{y}_c + m_p [2\dot{\xi}_i \dot{\theta}_c - \eta_i \dot{\theta}_c^2] \end{aligned}$$

For the coordinate θ_i , it is straightforward, and can be expressed as follows

$$\frac{d}{dt} \left(\frac{\partial T}{\partial \dot{\theta}_i} \right) = I_p \ddot{\theta}_c + I_p \ddot{\theta}_i$$

CURRICULUM VITAE

Surname, Name: Hosseiniaghdam, Behrang

EDUCATION

Degree	Institution	Year of Graduation
MS	University of Tabriz Mechanical Engineering	2007
BS	KNT Technical University Mechanical Engineering	2004
High School	Imam Khomeini high school Iran	2000

FOREIGN LANGUAGES

Advanced English, Fluent Turkish

PUBLICATIONS